Astronomy & Astrophysics manuscript no. anticentreEDR3
November 19, 2020

Gaia Early Data Release 3: The Galactic anticentre

Gaia Collaboration, T. Antoja[1], P. McMillan[2], G. Kordopatis[3], P. Ramos[1], A. Helmi[4], E. Balbinot[4], T. Cantat-Gaudin[1], L. Chemin[5], F. Figueras[1], C. Jordi[1], S. Khanna[4], M. Romero-Gomez[1], G. Seabroke[6], and et al.

[1] Institut de Ciències del Cosmos, Universitat de Barcelona (IEEC-UB), Martí i Franquès 1, 08028 Barcelona, Spain, e-mail: tantoja@fqa.ub.edu
[2] Lund Observatory, Department of Astronomy and Theoretical Physics, Lund University, Box 43, 22100 Lund, Sweden
[3] Université Côte d'Azur, Observatoire de la Côte d'Azur, CNRS, Laboratoire Lagrange, Bd de l'Observatoire, CS 34229, 06304 Nice Cedex 4, France
[4] Kapteyn Astronomical Institute, University of Groningen, Landleven 12, 9747 AD Groningen, The Netherlands
[5] Centro de Astronomía - CITEVA, Universidad de Antofagasta, Avenida Angamos 601, Antofagasta 1270300, Chile
[6] Mullard Space Science Laboratory, University College London, Holmbury St Mary, Dorking, Surrey RH5 6NT, United Kingdom

Received September 15, 1996; accepted March 16, 1997

ABSTRACT

Aims. We aim to demonstrate the scientific potential of the *Gaia* Early Data Release 3 (EDR3) for the study of different aspects of the Milky Way structure and evolution, while at the same time we provide a description of several practical aspects of the data and examples of their usage.
Methods. We use the astrometric positions, proper motions and parallaxes, and the photometry from EDR3 to select different populations and components and to calculate the distances and velocities in the direction of the anticentre. In this chosen direction, the *Gaia* astrometric data alone enables the calculation of the vertical and azimuthal velocities, and the extinction is relatively low compared to other directions in the Galactic plane. We then explore the dynamics of the current disc, the spatial and kinematical distributions of early accreted versus in-situ stars, the structures in the outer parts of the disc, and the orbits of the open clusters Berkeley 29 and Saurer 1.
Results. With the improved astrometry and photometry of EDR3 we find that: i) the dynamics of the Galactic disc are very complex with oscillations in the median rotation and vertical velocities as a function of radius, vertical asymmetries and new correlations, including a bimodality with disc stars with large angular momentum moving vertically upwards from below the plane, and disc stars with slightly lower angular momentum moving preferentially downwards; ii) we resolve kinematic substructure (diagonal ridges) in the outer parts of the disc for the first time; iii) the proto-Galactic disc present at the time of the merger with Gaia-Enceladus-Sausage is currently radially concentrated up to around 14 kpc, while the debris of the satellite extends beyond that; iv) there are density structures in the outer disc both above and below the plane most probably related to Monoceros, the Anticentre Stream and TriAnd, for which the *Gaia* data allows an exhaustive selection of candidate member stars and dynamical study; v) the open clusters Berkeley 29 and Saurer 1, despite being located at large distances from the Galactic Centre, are on nearly circular disc-like orbits.
Conclusions. Even with our simple preliminary exploration of the *Gaia* EDR3, we demonstrate how, once again, these data from the European Space Agency are crucial for our understanding of the different pieces of our Galaxy's and their connection to its global structure and history.

Key words. Galaxy: disc – Galaxy: halo – open clusters and associations: individual – Galaxy: formation – Galaxy: kinematics and dynamics – Stars: distances

1. Introduction

As for previous releases, the Early Third Data Release (EDR3, **?**) of the *Gaia* mission (**?**) of the European Space Agency comes accompanied with a series of performance verification articles that show the quality of the data, the improvements with respect to previous releases, and the scientific potential for multiple research areas in astrophysics (see also **???**).

In the present study we focus on a specific area in the sky that allows us to explore different elements of the Milky Way's structure and history: the Galactic anticentre. This region of the Galaxy has the advantage that from astrometric measurements alone (proper motions and parallaxes), one can calculate the vertical and azimuthal (rotation) motion of the stars with a negligible contribution of the line-of-sight velocity. Also, the anticentre has relatively low extinction compared to other directions of the Galactic disc.

More importantly, the anticentre is a meeting point of several distinct components of the Galaxy (the disc, the halo) and possibly hosts ancient and recently disrupted stellar systems of extragalactic origin. The anticentre is also an excellent window to the dynamics and the past of the Milky Way: due to the lower gravitational potential, any perturbation on the disc would cause more significant deformations than in the inner disc, and, due to the longer dynamical timescales, these could still be observable today (e.g. **???**).

In this paper we focus on several aspects of the Galaxy that coexist in the anticentre and that will help us towards answering a single question: "How does the Galaxy appear today and how did it become like this?" Thanks to a combination of models and measurements, in which *Gaia* DR2 (**?**) played one of the most relevant roles, we have already uncovered part of the Milky Way structure and history. The major accretion event of the so-called Gaia-Enceladus-Sausage around 10 Gyr ago (**??**), together with

the ongoing **accetion** of the Sagittarius dwarf galaxy (**??** and a recent detection with *Gaia* data in **?**), and internal structures such as the bar (**?**; **?; ??**) and the spiral arms (**??**) are among the most important phenomena that have shaped our Galaxy throughout its evolution (see also **?**). The footprints of these phenomena can still be observed today and that is what we investigate here.

First, we **look into the disturbances of the disc that EDR3 allows us to inspect** in its outermost parts, which are now reachable with EDR3. The inner disc has been shown to be highly complex: to the initial discoveries of the density structures of the disc such as the bar, the (poorly-constrained) spiral arms, the warp (**???**) and the flare (**???**), we add also vertical asymmetries in the number counts linked to vertical bending and breathing waves (e.g. **??**), moving groups also called dynamical streams (e.g. **???**), large scale velocity patterns in the disc (**????**) and other phase space correlations (e.g. **??**; **??**). More recently, showing even more disagreement with our preconceived image of a simple rotating Milky Way disc in equilibrium, the *Gaia* vertical phase spiral (**??**) possibly suggests a phase mixing event or bending wave after the perturbation of Sagittarius (**??**). The structures seen in the in-plane velocities (**???**) could be due to the same phenomenon possibly combined with the influence of the bar and the spiral arms. All of these aspects have proven to be extremely difficult to understand, and also to disentangle or relate, but they hold the clue to the role that recent and past, internal and external, disturbances have had in the Milky Way. Here we look at the rotation and vertical velocities of the outer disc, looking for more understanding of its complexity.

Second, we go from the current disc of the Galaxy to the ancient one. It has been shown that the **stellar** halo near the Sun is dominated by two components: an accreted one stemming largely from the galaxy Gaia-Enceladus-Sausage, and an in-situ component which is actually a heated (thick) disc that was present at the time of this merger (**?????**). These two distinct populations were clearly apparent in the Hertzsprung-Russell (HR) diagram of stars with large tangential velocities (i.e., representing the halo) by **?** using *Gaia* DR2: a blue and a red sequence corresponding to the accreted halo and the hot thick disc, respectively. Here we investigate out to which distance the debris of Gaia-Enceladus-Sausage may be found, and constrain the extent of the proto-Galactic disc present at the time of the merger by analysing the spatial distribution and kinematics of stars belonging to each of the HR sequences.

Thirdly, we explore the interface between the disc, and the halo and its different structures. **?** used the deep Sloan Digital Sky Survey (SDSS **?**) to scout the stellar content at the edge of the disc and discovered the existence of a $\sim$100° structure in their A/F star count maps. Now known as Monoceros, later studies have confirmed its existence and large extension on the sky (e.g., **???**). Together with the Anticentre stream (ACS, **?**), both at a distance $\sim$10 kpc from the Sun, and the Triangulum-Andromeda overdensities (TriAnd, **???**), they are part of a complex and substructured outer disc. The initial interpretation that these could be the remains of an accreted dwarf galaxy (e.g, **??**) has, with time, become less plausible (although not completely ruled out) since: i) there is no known progenitor to the stream (the candidate Canis Major has been discarded – **???**), ii) the kinematics of the structures are compatible with the disc (e.g., **?**), and iii) their metallicities and their ratio of RR Lyrae to Giants points towards a galactic origin (**??????**). Here we explore how these structures look in *Gaia* EDR3 and coexist with other structures such as the Sagittarius stream.

Finally, we explore the open clusters Berkeley 29 (**????**) and Saurer 1 (**??**) in the anticentre direction that, with ages of several Gyr, are among the oldest Galactic clusters known. Their unusual location at Galactocentric distances of $\sim$20 kpc and more than 1 kpc above the Galactic mid-plane is a puzzle that has led several authors to question whether they are associated with the disc, and to propose a possible extragalactic origin (e.g. **?**). Attempts to characterise the orbits of these two objects have returned widely discrepant results (**??**), mainly due to their poorly-constrained proper motions since at such large distances, small proper motion errors translate into large uncertainties in physical velocities. An additional issue has been the uncertain membership status of individual stars. Here, thanks to *Gaia* EDR3, we perform a robust analysis of the membership of these clusters and derive their orbits with high confidence.

To investigate all these aspects, the main *Gaia* data products that we use here are the astrometric measurements. For EDR3 these show a substantial decrease of uncertainties resulting from the use of 34 months of data (12 more than for DR2). Apart from a higher completeness at the faint end, there is a significantly larger number of stars at a given parallax precision. The combination of all these improvements essentially means that we can now explore distant regions of the Galaxy in the direction of the anticentre, even reaching around 16 kpc from the Galactic centre and beyond (see Sect. 2 for details), and thus, the very outskirts of the disc, for a sample with positions and velocities of excellent quality. Moreover, important improvements in the pipelines of the *Gaia* photometry have resulted in photometric bands with significantly less systematic error, from which, combined with the improved parallaxes, cleaner HR diagrams can be built and used to select different populations and components.

The paper illustrates how, once more, the new *Gaia* data **are** set to revolutionise our knowledge of the Galaxy and its past. Additionally, we describe practical aspects of the data and examples of its **use** that might be of interest for the community, such as queries in the *Gaia* Archive, quality cuts, derivation of distances (Bayesian inference, considerations on the parallax zero point), etc. We also complement our analysis with the use of simulated data from the Gaia Object Generator (GOG, **?**) & the Gaia Universe Model Snapshot (GUMS, **?**), now available directly in the Gaia Archive, to evaluate the effects of selection, errors and extinction.

We start our paper by explaining the different datasets used and demonstrating the different improvements (but also limitations) of the EDR3 data in the anticentre direction (Sect. 2) We continue by explaining how the distances and phase space coordinates are derived (Sect. 3). The results sections follow, organised **into** the explorations of the disc dynamics (Sect. 4), halo, thick disc and outer disc structures (Sect. 5), and distant open clusters (Sect. 6). We present our discussion and conclude in Sect. 7.

2. Data

2.1. Main datasets

In this work we explore the Galactic anticentre region using different data selections obtained from *Gaia* EDR3 (**?**) that can be accessed through the *Gaia* Archive (`https://gea.esac.esa.int/archive/`, **?**). More details on the data and validation are given also in **?**, **?** and **?**. The main datasets are shown in Fig. 1 and listed below. The number of stars for these samples are summarised in Table 1, in which a comparison with DR2 is also shown.

(1) AC20: A square **on** the sky centred at $(\ell, b) = (180, 0)$ deg of **20**deg **on a side** (blue square in Fig. 1). This sample is

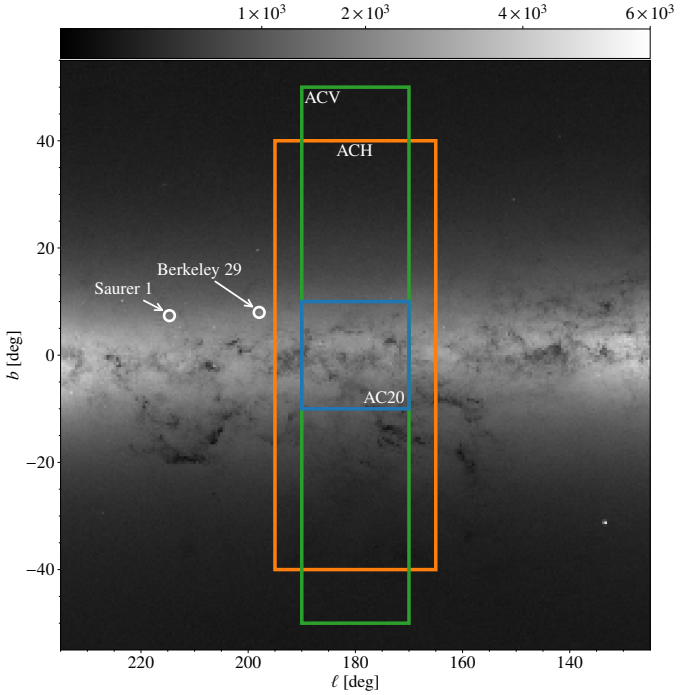

Fig. 1. EDR3 star counts in the anticentre region with the different data selections used. The HEALpix map is obtained by querying the *Gaia* archive the counts of stars within each HEALpix of level 8 (query 2 in Appendix A). The size of the circles to indicate the position of the clusters does not correspond to the size used for the selection which is much smaller. Several other clusters can be seen in the figure, and also the Triangulum Galaxy (M33, bottom right corner).

Table 1. Number of stars in the different samples and comparison with DR2. The numbers are given for the different data **samples** described in Sect. 2.2 and different sub-selections are also detailed. **The numbers in the first two numerical columns are for samples without the `excess_flux` and `RUWE` selections since these are not equally defined in the different releases.** [(a)] See footnote 1.

	DR2	EDR3	**EDR3+filters**
1. AC20	13 307 312	14 120 029	**11 949 642**
5p-6p[a]	10 750 864	12 279 076	**11 949 642**
$\varpi/\sigma_\varpi > 3$	2 645 014	3 518 388	**3 369 456**
photometry	12 618 364	**13 706 954**	**11 436 625**
2. ACV	24 578 296	**2 5835 286**	**21 835 927**
$\varpi < 0.1$ mas	4 974 104	**4 879 087**	**4 509 263**
$\varpi < 0$ mas	3 945 985	**3 781 306**	**3 496 645**
4. ACC	648	**654**	**597**
Berkeley 29	365	**370**	**334**
Saurer 1	283	**284**	**263**

used to explore Galactic disc kinematics in Sect. 4. It contains **14 120 029** stars but most of the time we use only the selection with $\varpi/\sigma_\varpi > 3$ (see Sect. 3.2), which comprises **3 518 388** sources (AC20-$\varpi/\sigma_\varpi > 3$). The data **are** retrieved from the archive using the query 1 in Appendix A. Similar queries have been used for other samples.

(2) ACV: A **rectangle on** the sky centred at $(\ell, b) = (180, 0)$ deg with a width of 20 deg in ℓ and height 100 deg in b (green rectangle in Fig 1). This sample is used to explore the structures in the outer disc such as Monoceros or the Sagittarius stream in Sect. 5.2. For parts of our analysis, we perform a selection of $\varpi < 0.1$ mas to favour distant stars. We note that with this selection there are **2%** fewer stars in EDR3 than in DR2 (Table 1). While the total number of stars in that region has increased with respect to DR2, many of the stars added are nearby faint dwarfs (see Sect. 2.3) and the overall quality of the parallaxes has improved significantly as proven by the decrease in the number of sources with a negative parallax (and spurious sources). As a consequence, our parallax cut is now able to reject the nearby sources more efficiently, thus resulting in a slightly smaller sample.

(3) Two clusters in the anticentre: All sources brighter than $G = 19$ within 4 arcmin of the centres of the extremely distant Galactic old open clusters Berkeley 29 and Saurer 1. These data are analysed in Sect. 6.

In all our analysis, our fundamental observables are the astrometric quantities ϖ, $\mu_{\alpha*}$, μ_δ (parallax and proper motions) and the photometric bands G, BP, RP. In order to use the best quality data, we apply several selections. First we apply the following astrometric quality selection on the Renormalised Unit Weight Error (`RUWE`) as recommended in **?**:

$$\texttt{RUWE} < 1.4 \quad (1)$$

On the other hand, whenever the photometry is used we select **good photometry** sources with:

$$0.001 + \mathbf{0.039}(BP - RP) < \log_{10} \texttt{excess\_flux} < 0.12 + \mathbf{0.039}(BP - RP). \quad (2)$$

Sources out of these limits have inconsistent G, $G_{\rm BP}$ and $G_{\rm RP}$ fluxes due to blends (more than one source in the BP/RP windows), contamination by a nearby source (out of the window) or a sign of the extended nature of the source. Additionally, we correct the fluxes in G for 6p sources sources following ? -their Table 5- using directly an ADQL query as suggested in ?. The last column in Table 1 indicates the number of stars after these selections.

2.2. Complementary datasets

For validation and other purposes, we also use the following complementary data:

(i) 6Dsample: a full sky sample with stars that have DR2 **line-of-sight** velocity in EDR3 (**?**), thus with full 6D phase space information. **After filtering,** this sample contains **6 156 684** stars and is used mainly in Sect. 4.

(ii) DR2: the same selections as above (AC20, ACH, ACV) but for DR2. These are used for comparison with EDR3.

(iii) GOG **& GUMS**: the same selections as above but for GOG (Luri et al. 2014; GEDR3 documentation Chapter 2) **which is a mock *Gaia* catalogue based on the Besançon model (?), and for GUMS (?) which** contains the intrinsic properties of the sources before applying the *Gaia* instrument modelling. Here we use the GOG version 20.0.3. with uncertainties that have been scaled to 34 months of data (but see Fig. E.1). These samples are used for the evaluation of completeness and extinction effects and they do not contain any kinematic substructure or asymmetries. Furthermore, GOG and GUMS are used in Appendix C for testing how robust each of the distance estimation methods is. These simulated data have been retrieved through the Gaia Archive querying from the corresponding tables (`gaiaedr3.gaia_source_simulation` and `gaiaedr3.gaia_universe_model`).

(iv) 2MASS: **We use the official crossmatch of EDR3 with the** *2MASS* **point source catalogue (?), provided in** `gaiaedr3.tmass_psc_xsc_best_neighbour`**. For the AC20 sample,** this **yields** about 55% anticentre objects with *2MASS* photometry. These data are used to select Red Clump (RC) stars and compute their photometric distances (Sect. 2.4 and 3.2, Appendix B and C.2.1).

More information can be found in the respective sections **in which** these samples are used.

2.3. EDR3 data quality and completeness

In this section we examine the quality of the EDR3 data and compare it to DR2. Overall, the most relevant improvements in EDR3 for our study include a larger number of sources at the faintest magnitudes, as well as a significant decrease of the astrometric uncertainties and thus a significantly larger number of stars with a certain parallax precision. Below we show these aspects in more detail focusing on the AC20 region as an example unless stated otherwise.

1. General description. Figure 2 shows the AC20 region in Galactic coordinates coloured according to different quantities in bins of 0.1 deg. In panel a we show the number of stars per bin while the rest of the panels show median quantities. **As expected, the counts anti-correlate with the patterns seen in the extinction map (d, see Sect. 2.4 for more details on how this is estimated) combined with the decrease with Galactic latitude $|b|$. The median magnitude (b) and median colour (c) also correlate with extinction (d):** higher extinction regions have, on average, more reddened sources that have fainter (more extinguished) apparent magnitudes. Panel d shows that there is higher extinction for $b < 0$. Additionally, there is a horizontal elongated window at $b \sim 2.5$ deg of low extinction with far more counts and brighter magnitudes, which is seen also in other panels where brighter magnitudes essentially translate into smaller astrometric errors (e.g. panel g) and also smaller parallaxes (panel f, stars reaching farther distances). **Whether this feature with larger counts reflects more than simply lower extinction (e.g. a flexing of the disk) requires a deeper analysis of the extinction and the selection function. We also note that the thin nearly-horizontal lines in panels a and b are a consequence of the** `RUWE` **selection.**

2. Completeness. The evaluation of the completeness of the *Gaia* data is a difficult task given that there is no deeper survey with a comparable resolution. Distinct methodologies to assess the data completeness can be found in **?**, **?** and **?**. Here we examine it in a simpler way. First we note that the AC20 sample (without any cuts) has about one million more stars in EDR3 compared to DR2 (see Table 1). Figure 3 shows histograms of the G magnitude for stars in the AC20 sample in DR2 and EDR3 (blue and red histograms) showing a great increase of sources at the faint magnitudes with respect to DR2. This was expected given that the detection on board prioritises bright magnitudes and the effect of more months of observations produces new detections mostly at the faintest bins.

Figure 2e shows the map of median `visibility_periods_used`. This panel shows bands at different spatial scales that correspond to regions with higher/lower number of observations and thus higher/lower completeness. The thin, nearly-horizontal, yellowish pattern, separated by roughly 0.7deg, similar to the width (across scan) of *Gaia*'s FOV, corresponds to consecutive scans that did not overlap in across scan. The wider red bands, indicating areas where the coverage is better, are close to some "nodes" in the scanning law, that is, the positions in the sky that get repeated coverage during some consecutive scans. Indeed, Fig. 4 shows the star counts for different ranges in G for DR2 (top) and EDR3 (bottom) using the same colour scale. The bands of the scanning law appear clearly and correlate with Fig. 2e. Comparing to DR2, we can clearly notice the larger number of stars in EDR3 in these two magnitude ranges as well as the reduction of some of the bands (at scales of $\sim$ 3 deg) imprinted in DR2. In the range of $20.75 < G < 21$ some scanning bands are still present.

3. Completeness of the kinematic samples. Some of the *Gaia* sources have only partial astrometric solutions, from which only sky coordinates are derived (2p solutions) while others have full astrometric solution (positions, parallax and proper motions available) and are dubbed 5p and 6p solutions (**?**)**, where the 6th parameter is the colour**[1]. In the first rows of Table 2 we **give** the number of stars with partial (2p) and full (5p, 6p) solutions comparing DR2 and EDR3 for the whole AC20 sample and for different ranges of magnitude. **In** EDR3, there are two million more stars with full astrometric solution **than in** DR2. The table also shows the percentage of full solutions relative to all sources in EDR3, which gives an indication of the internal completeness of the kinematic data. Most notably, in the range of $19 < G < 20$ there is now a 98% internal completeness compared to the 82% in DR2, and in the range $20 < G < 20.7$ the percentage is now 90% versus the old 64%, verifying that, as shown also with the orange and purple histograms of Fig. 3, there is an outstanding gain at the faintest magnitudes. These stars have never been used before in kinematic studies with *Gaia* data.

We note that 6p solutions tend to be associated to fainter sources and their astrometric solutions are worse than for 5p ones (they have on average fewer `visibility_periods_used`, i.e. less observations, and larger `ipd_frac_multi_peak`, i.e. relatively large probability of being a double source, either visual or real binary), having larger astrometric errors. While for the AC20 sample the fraction of 6p solutions is comparable to the 5p (42 and 45%, respectively, the remaining 13% being 2p), for the AC20-$\varpi/\sigma_\varpi > 3$ case they represent only a 14% (86% being 5p) since we require good relative parallax errors.

After selecting stars with $\varpi/\sigma_\varpi > 3$ (AC20-$\varpi/\sigma_\varpi > 3$ sample) we find approximately one milion more stars in EDR3 than in DR2 (bottom rows of Table 2), which represents an increase of 33%. Figure 3 (green and brown histograms) shows an improvement of the completeness of the parallax quality selection at magnitudes fainter than $G = 16$, which means better sampling **at** all distances and probing larger ones. Table 2 also shows that at the relatively bright magnitudes $15 < G < 17$, there were 74% of stars in DR2 satisfying this condition but we have now 88%. It is nevertheless important to remark that the completeness of the

[1] 2p partial solutions (only positions) are indicated as `astrometric_params_solved`=3 in the Gaia Archive. 5p solutions are those for which the *Gaia* colour is used in the astrometric solution, while in the 6p cases, this quantity, more precisely, the pseucolour, is derived simultaneously in the solution (**?**). The 5p and 6p solutions correspond to `astrometric_params_solved`=31 and 95, respectively. In DR2 all full astrometric solutions were included under the `astrometric_params_solved`=31 case, **even if** in some cases a chromaticity different from the **photometric** colour was used

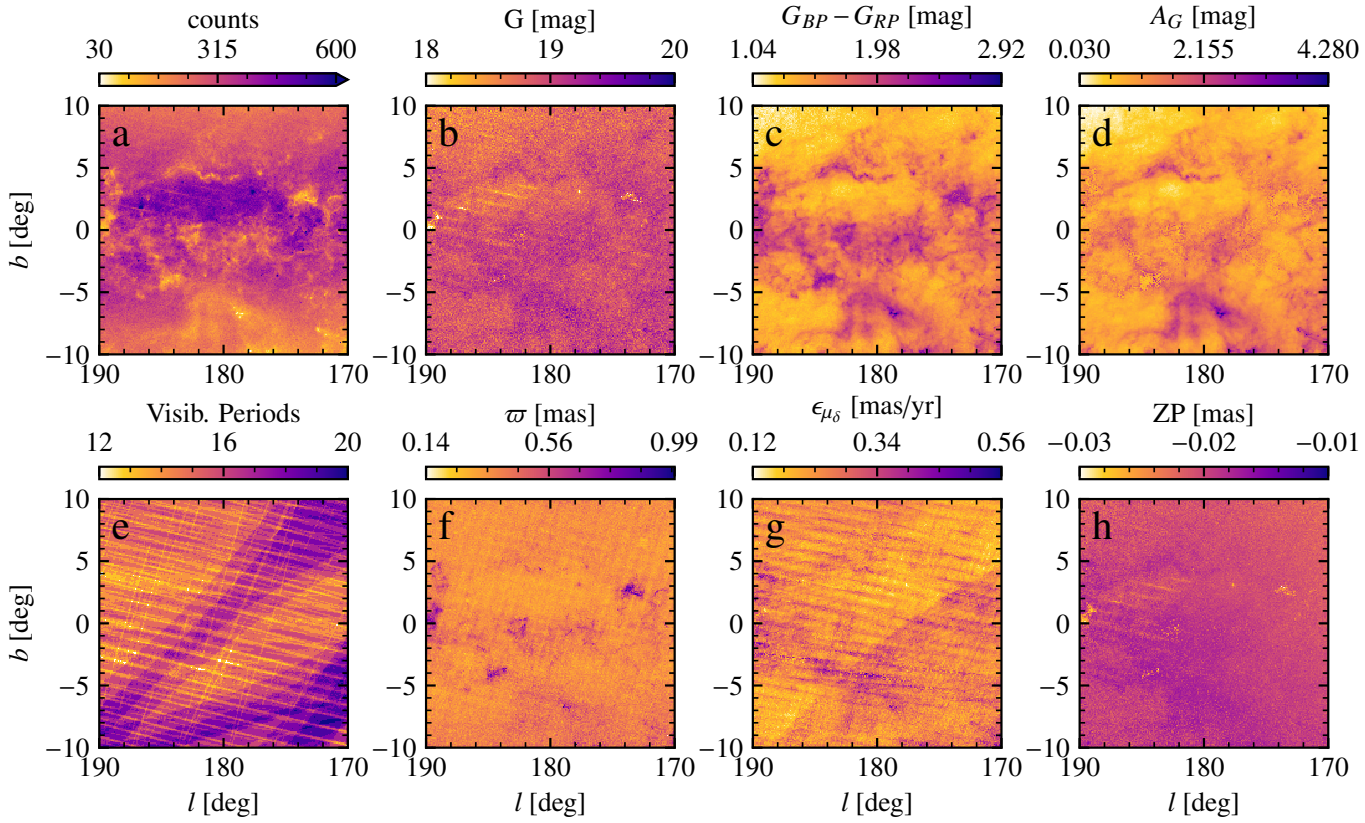

Fig. 2. Characteristics of the anticentre AC20 sky. Panel (a) shows the number of sources and the rest of panels show median quantities for bins of 0.1*deg* of the magnitude (b), colour (c), extinction in the G band (d, **with the $\varpi/\sigma_\varpi > 3$ selection**, see Sect. 2.4), `visibility_periods_used` (e), parallax (f), uncertainty in the proper motion in the δ direction (g), and zero point correction to the parallax ZP_{56} (h, see Sect. 3.1)

Table 2. Indicative completeness of the kinematic samples. Absolute number of stars and fractions for all magnitudes and for distinct magnitude ranges are given for the cases with 2p and 5/6p solutions and for the selection of $\varpi/\sigma_\varpi > 3$. To compute the percentages for DR2, the total number of sources in EDR3 for each case have been used. **These numbers are for samples without the `excess_flux` and `RUWE` selections since these are not equally defined in the different releases and the selection in `RUWE` eliminates the 2p solutions.**

	DR2			EDR3		
	2p	5p	(5p) /ALL-EDR3	2p	(5p∪6p)	(5p∪6p) /ALL-EDR3
$\forall G$	2556448	10750864	76%	1840953	12279076	87%
$G < 19$	111638	5860281	96%	**67217**	**6010199**	99%
$19 < G < 20$	492849	2825129	82%	**60360**	**3369371**	98%
$20 < G < 20.7$	940298	1944641	64%	**312553**	**2705704**	90%
	$\varpi/\sigma_\varpi < 3$	$\varpi/\sigma_\varpi > 3$	$\varpi/\sigma_\varpi > 3$ /ALL-EDR3	$\varpi/\sigma_\varpi < 3$	$\varpi/\sigma_\varpi > 3$	$\varpi/\sigma_\varpi > 3$ /ALL-EDR3
$\forall G$	10662298	2645014	19%	10601641	3518388	25%
$G < 15$	30930	478565	93%	**13098**	**500913**	**97%**
$15 < G < 17$	360149	1096109	74%	**170528**	**1301329**	**88%**
$17 < G < 19$	6284445	1039701	14%	**5860892**	**1660388**	22%
$19 < G < 21$	3826133	30637	0.7%	**4232117**	**55142**	1%

sample with good parallaxes is low even at intermediate magnitude ranges both for the DR2 and EDR3 (as low as 14% and 22% in the range $17 < G < 19$, respectively), although we see an overall improvement for the new release.

4. Astrometric quality, systematics and parallax zero point. The improvement in astrometric quality of EDR3 with respect to DR2 is discussed in **?** and **is reflected in smaller uncertainties and** a reduction of the number of negative parallaxes (e.g. for the ACV sample where there are 164679 less sources with negative parallaxes, Table 1). Figure E.1 in Appendix E illustrates the improvement in the uncertainties for the anticentre (similar to figure A.1 by **?** for all EDR3). Both plots show a reduction by a factor of 0.79 and 0.5 in parallax and proper motion uncertainties, respectively, as expected for the increase in the number of months of observations, with even a larger reduction for sources brighter than $G \sim 14$. It is this improvement in the astrometric quality that allows us to have now a much larger sample of stars with very good relative parallax errors, and reach farther distances from the Sun. We also note that the uncertainty in μ_δ is smaller than for $\mu_\alpha*$. This is due to a geometrical scaling factor on the uncertainties that appears as a result of the scanning law which in the direction of the anticentre favours μ_δ.

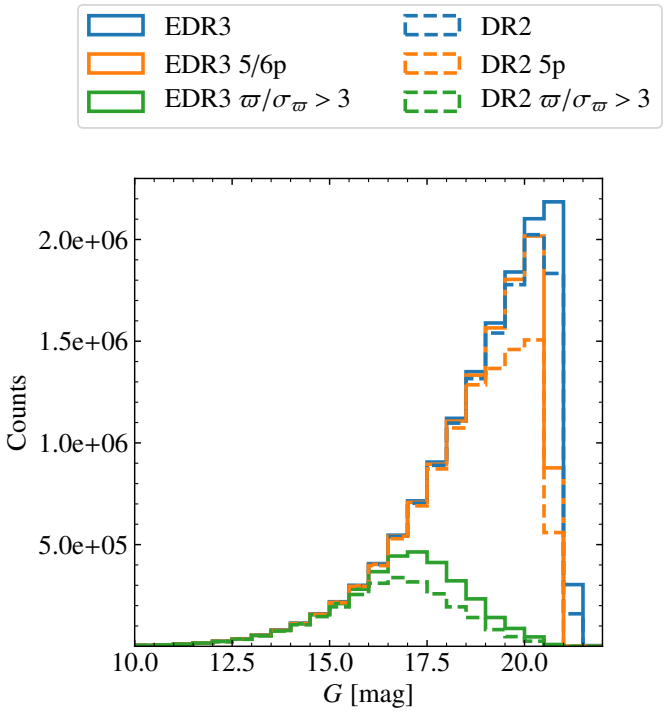

Fig. 3. Distribution of G magnitude for different selections in the anticentre. We show the number of stars in bins 0.5 mag for the AC20 case. The gain from DR2 to EDR3 is mostly at the faintest magnitudes where some sources did not have enough observations **to appear in** the past release.

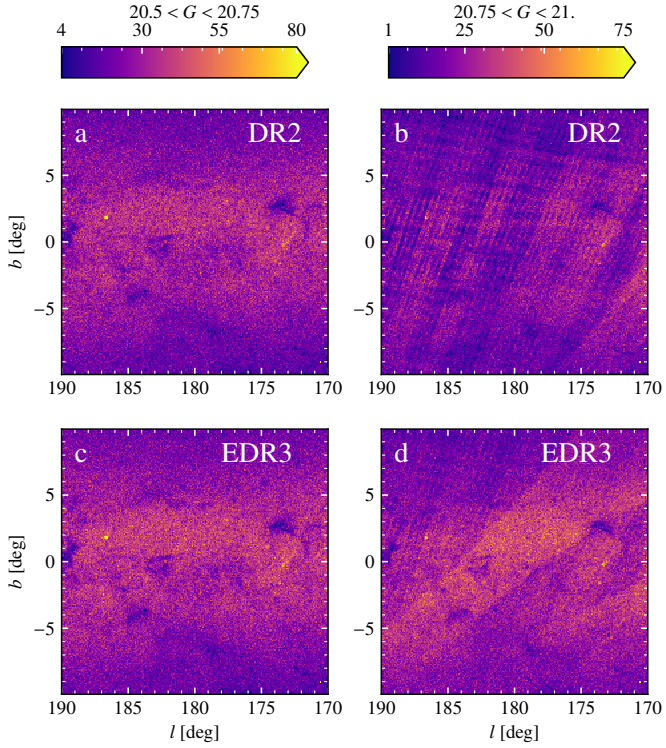

Fig. 4. DR2 and EDR3 counts for different magnitude ranges. The panels show the number of sources in bins of 0.1 deg in two different ranges of magnitude: $20.5 < G < 20.75$ (left) and $20.75 < G < 21$. (right). To facilitate the comparison, the same colour bars has been used for each vertical pair of panels and the upper limit of the colour scale does not correspond to the maximum number of counts to avoid dominance of bins with clusters. An increase of the number of counts in EDR3 is observed, together with the decrease of some of the small scale patterns, although some bands remain in the faintest magnitude range.

As in previous releases, the astrometric *Gaia* data suffers from some systematics. The median astrometric quantities and their uncertainties show checkered patterns that somehow correlate with the scanning law, as illustrated for the median parallax (Fig. 2f) and median uncertainty in μ_δ (Fig. 2g). The later shows additionally some of the large scale bands mentioned above. The amplitude of these systematics has, however, been reduced in EDR3 (see **?**). Another known systematic is a zero point in parallax **?** that has also been reduced and which we examine in detail in Sect. 3.1.

Figure 5 shows the differences in all astrometric quantities between DR2 and EDR3 normalised to the errors[2]. The median absolute differences between EDR3 and DR2 are 17 μas in ϖ, -48 mas yr^{-1}in $\mu_{\alpha*}$ and 6 mas yr^{-1}in μ_δ. For comparison, we show a Gaussian distribution with 0 mean and 1 as variance with a blue curve, although the quantities from DR2 and EDR3 are not independent and thus these distributions are not expected necessarily to follow this curve. We see some systematic differences in the proper motion in right ascension $\mu_\alpha*$ (green histogram). This is explained by a correction of the reference frame (spin) for EDR3 that has largely reduced the medium-scale (1-20 deg) inhomogeneities in the median parallax and proper motion of the quasars, which actually were quite large precisely in the direction of the anticentre and for $\mu_\alpha*$ (about 0.1μas, figures 10 and 11 of **?**). The histogram of parallax differences is narrower than the Gaussian case and is slightly positively biased. In Fig. 5 the zero point has been corrected using the median estimated values for quasars respectively in DR2 and EDR3 (more details are given in

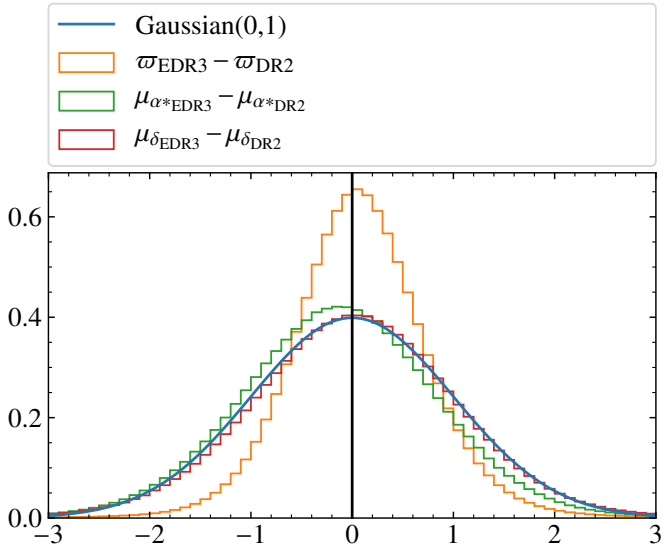

Fig. 5. Consistency between astrometric values in DR2 and EDR3. The histograms show the differences in parallax and proper motion normalised to the errors $(x_{\rm EDR3} - x_{\rm DR2})/\sqrt{\sigma^2_{x,\rm EDR3} + \sigma^2_{x,\rm DR2}}$, **where** x **is** ϖ**,** $\mu_\alpha*$ **or** μ_δ, and compared to a Gaussian distribution with 0 mean and variance of 1. The differences in $\mu_\alpha*$ are due to a systematic in DR2 that has been now corrected. We have corrected the parallaxes (Eq. 3) using the median offset for DR2 (-27 μas) and for EDR3 (**-17** μas).

[2] We have used sources having the same `source_id` in DR2 and DR3. Even though we know from **?**, **?** and **?** that some sources have changed `source_id`, this occurs for a minority of cases and does not affect the results from Fig. 5

Table 3. Populations in the AC20 sample. The selections are obtained following the Method I, except for the RC of the last row (Method II).

	Population	Sources
	All	3486633
EY	Extremely Young Massive ($\tau \lessapprox 0.2\,Gyr$)	9708
YP	Young MS with $0.2 \lessapprox \tau \lessapprox 2\,Gyr$	240329
IP	Intermediate MS with $2 \lessapprox \tau \lessapprox 8\,Gyr$	601404
OP	Old MS	1636273
RG	Red Giants	193359
RC	Red Clump	**121857**

Sect. 3.1). We note that the bias was even larger if we neglected the corrections (giving a median of 25 μas). The persistent bias even after the correction could be attributed to underestimation of the zero point in DR2 (for which there is some evidence, see **?**) or effects of considering a fixed value of the offset (Sect. 3.1).

4. Photometric quality. The improvement of the photometry of EDR3 with respect to DR2 is described in **?**. In summary, the increase of the number of observations and the improvement of several steps of the pipelines (image parameter determination, LSF/PSF calibrations, cross-match and photometry) have led to a significant decrease of the systematics at the bright end ($G < 15$). The effects of blends and contamination by nearby stars are mainly filtered out using Eq. 2.

2.4. Extinction and selection of tracer populations

We use two different approaches to select the tracer populations. The first strategy uses only *Gaia* data and the populations are selected in the de-reddened HR diagram. In the second and more refined approach, external photometric data is used to define a sample of RC sources.

Method I: Using the *Gaia* HR diagram. We obtain the de-reddened HR diagram for the AC20-$\varpi/\sigma_\varpi > 3$ sample using the 3D extinction map of **?**, which was derived from Gaia DR2 photometry. This map was the one used in the generation of the mock catalogue of GOG and here, in practice, we obtain the extinction of our sources by using this same implementation. We use the d_{PM} distances (Sect. 3.2 and Appendix C.1) and the galactic (ℓ, b) coordinates to infer the line-of-sight visual extinction A_V for each source. Then we transform A_V to A_G and $E(BP-RP)$ using the polynomial expressions from Appendix A in **?**. This 3D extinction map only considers dust structures in a $6 \times 6 \times 0.8$ kpc box centred on the Sun and, as in GOG, we assume there is no significant additional extinction toward the anticentre outside this box. This may cause an underestimation of the extinction (apparent in Fig. 6) for sources located behind distant and dense molecular clouds in specific sky areas. Indeed, we have seen that the extinction values **yielded by** this strategy are, in some sky areas, slightly smaller than the ones from the 3D dust-reddening maps from Bayestar (**?**) that we use to derive the RC sample (see below).

Figure 6 shows the Gaia de-reddened HR diagram for the AC20-$\varpi/\sigma_\varpi > 3$ sample. We use the direction of the extinction line in this diagram ($M_G = 1.95(BP-RP)_o - 0.8$, black diagonal line) combined with the vertical cut $(BP-RP)_o > 0.8$ to select (conservatively) giants (purple dots). Then we use the PARSEC

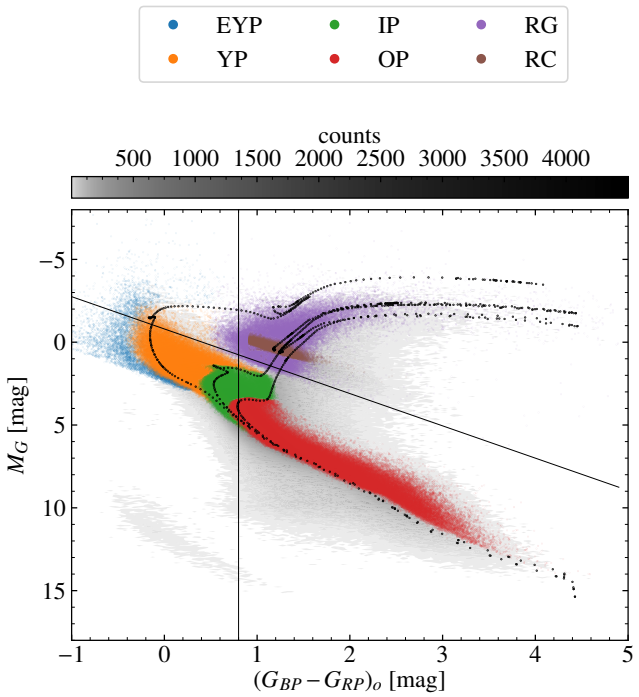

Fig. 6. De-reddened HR diagram of the anticentre region and different selected populations. The diagram is shown for the 3486633 sources of the AC20-$\varpi/\sigma_\varpi > 3$ sample with available photometry (G, BP, RP) and extinction data derived considering the d_{PM} distances. We over-plot three PARSEC stellar isochrones with $[M/H] = 0$ for the ages of 0.2, 2 and 8 Gyr, a line at $BP - RP = 0.8$ and a diagonal line following the extinction slope used for the selection of populations (Method I) that appear in different colours, while the RC have been selected using a different method (Method II) .

isochrones (**??**) and respective updates[3] to perform a statistical partition by ages of the main sequence sources into extremely young (EY, 0.2 Gyr), young (YP, 0.2 - 2 Gyr), intermediate (IP, 2 - 8 Gyr) and old populations (OP), as specified in Table 3 and illustrated in Fig. 6. The massive sources of the EY population are constrained to have $(BP-RP)_o < 0.8$, while the YP, IP and OP are selected between the lower (ZAMS) and the upper (TAMS) luminosity boundary of the main sequence band defined by the PARSEC stellar evolutionary tracks at $[M/H] = 0$. We note that while the OP has contribution from young stars, we can claim it is on average older that the IP: we expect an average age of 4-5 Gyr (e.g. figure 13 in **?**) but with an important contribution of the oldest stars in the disc. In general, we expect these selections to be contaminated by stars of different ages due to several aspects (stars with different metallicities to the ones used in the isochrones, inaccuracies of the extinction model used, confluence of isochrones around the ZAMS, binarity, etc). Nevertheless, we expect our samples to be dominated by the age ranges desired, which is enough for our basic purposes here.

Method II: Using Gaia & 2MASS. We combine EDR3 parallaxes and G-band photometry with that from *2MASS* K-band for the AC20-$\varpi/\sigma_\varpi > 3$ sample. The passbands in *2MASS* are narrow and in the infrared, and are thus weakly affected by errors in the extinction estimation. For *2MASS*, the flag (qfl) = 'AAA' indicates the highest photometric quality. However, this would significantly reduce our sample (to only 15% of the entire AC20

[3] http://stev.oapd.inaf.it/cgi-bin/cmd

sample). Instead, we choose to enforce a quality cut only at the distance estimation stage using the photometric errors, *e_jmag* & *e_kmag*. We first compute the extinction of each source using the 3D dust-reddening maps from *Bayestar* (**?**) with the inverse of the parallax as a prior for distance. The RC sources are selected in a Bayesian manner around the literature values for the absolute magnitude of the RC simultaneously for the *G Gaia* band and the *2MASS K* band. More details of the procedure and a validation with an external sample are given in Appendix B and C.2.1.

3. Distances and phase space coordinates

In this Section we describe how the distances and phase coordinates are computed in our study. We start by discussing the zero point in the *Gaia* parallaxes (Sect. 3.1), which needs to be corrected in order to estimate first distances (Sect. 3.2), and subsequently Galactic cylindrical positions and velocities (Sect. 3.3).

3.1. Parallax zero-point correction

As for previous releases, the *Gaia* parallaxes have a zero point[4] (ZP) that needs to be **considered. In EDR3** the median parallax of the quasars is $-17\,\mu as$ **(?)**. This negative correction needs to be subtracted from the EDR3 parallaxes (effectively increasing the values of the parallaxes):

$$\varpi^{\text{corrected}} = \varpi - ZP \tag{3}$$

or equivalently, reducing the inferred distance. Here we correct all parallaxes by subtracting $ZP = -17\,\mu as$. Additionally, when relevant, we also compare our results with the more sophisticated approach presented in **?**. In that work, they estimate the parallax zero-point ZP_{56} as a function of magnitude, colour (more precisely, `nu_eff_used_in_astrometry` for the 5p solutions and `pseudocolour` for the 6p solutions, hence the names ZP_5 and ZP_6), and ecliptic latitude, by looking at the parallaxes of quasars, binary stars and sources in the Large Magellanic Cloud for EDR3. Here we compute ZP_{56} using the Python implementation that will be available online. Panel h in Fig. 2 shows the median zero-point ZP_{56} in the AC20 region. We observe a mild dependency of its value on the sky position.The median value for all stars in AC20 region is $ZP_{56} = -\mathbf{20}\,\mu$as, thus the same as for the quasars, with the 10 and 90 percentiles being $-\mathbf{32}$ and $-14\,\mu$as, respectively, and $ZP_{56} > 0$ only for 0.02% of the stars. For the AC20-$\varpi/\sigma_\varpi > 3$ sample, which has a significantly different magnitude distribution compared to the case without the parallax quality cut (Fig. 3), we find a median ZP_{56} of -30 μas and percentiles of -38 and -20 μas, respectively. The ZP_{56} case**, thus, yields** the largest differences **between uncorrected and corrected distances** (Fig D.1 in Appendix D). The velocities, which depend linearly on the distances, are consequently scaled as well. All these will be important in order to determine, for example, the exact distances to some kinematic features that we detect but we do not observe any qualitative difference in our results. More details are given in Appendix D and throughout the paper.

3.2. Distances

To convert the astrometric measurements by *Gaia* into phase space coordinates, we require an estimate of the distance to a given star. The complications of estimating distances to stars given their measured parallaxes have been discussed by a number of authors over a long period of time (e.g. **????**). The transformation between parallax and distance is non-linear, which leads to a number of issues, including the extreme case of negative measured parallaxes. Simply taking the inverse of the measured parallax gives a biassed estimate of the distance of a star, and this bias grows more serious as the relative uncertainty grows larger. It has therefore become extremely common to apply a Bayesian approach to the problem of providing distance estimates from parallaxes, and/or to use photometric information to produce a better estimate of the distance.

We work primarily with distance estimates from a Bayesian approach (d_{PM}), similar to that applied by **?**, with a prior that is derived iteratively to be consistent with the data. These distances use a **prior** $P(d) \propto d^2 P_\rho(\mathbf{r}(d)) S(d)$**, where** $\mathbf{r}(d)$ is the position at distance d along a given line-of-sight, **so** $P_\rho(\mathbf{r}(d))$ **is proportional** to the density of a model Galaxy. The term $S(d)$ is the selection function – i.e. the probability that a randomly chosen star at a distance d enters the catalogue. The distance estimate, $\tilde{d}$ is then found as the expectation value of d given this prior and the measured parallax (**and its** uncertainty). As explained in the previous section, default distances are computed considering a fixed **parallax zero point of** -17μ**as.** More details can be found in Appendix C.

To check that our results are robust, we compare to results when we estimate the distance as simply the inverse of the parallax, and also with a different Bayesian approach based on that from **?**. We have tested each of these approaches on GOG data, and further details are given in Appendix C. From these tests, we conclude that using a parallax quality cut of $\varpi/\sigma_\varpi > 3$ is a good compromise between the performance of the estimate and the number of stars of our samples. However, we emphasise that all the estimators tested here return somehow imperfect distances, which in the Bayesian case depend also on how close the assumed prior on the Galaxy distribution is to the Galaxy model **used in GOG (i.e. the Besançon Galaxy Model)**. We find that the median relative difference between the simulated true distances and the estimated ones can be as large as 20% at 4 kpc and larger than 50% for 25% of the stars even with the $\varpi/\sigma_\varpi > 3$ selection.

On the other hand, for the stars classified as RC (see Sect. 2.4), we infer their distance (d_{RC}) in a Bayesian manner using complementary photometric data from *2MASS* (details are given in Appendix C.2.1).

3.3. Positions and velocities

From the distances obtained in Sect. 3.2 and the sky positions, we compute the Galactic Cartesian (X, Y, Z) and cylindrical (R, ϕ, Z) positions, assuming that the Sun is located at $d_{\odot-GC} = 8.178$ kpc from the Galactic centre (**?**) and a height above the Galactic plane of $Z_\odot = 0.0208$ kpc (**?**). Figure E.2 in Appendix E shows the spatial distribution of the the AC20 sample. By construction, the vertical (Z) and azimuthal Y distributions are wider for larger distances from the Sun, with some stars at $R \sim X = 14$ kpc reaching heights of 1 kpc above and below the plane. Figure 7 shows the number of stars as a function of Galactocentric radius. The gain in EDR3 for sources with $\varpi/\sigma_\varpi > 3$ (black line) compared to DR2 (grey line) at large radii is very significant with an increase of one order of magnitude already at 16 kpc and notably more stars at almost all radii.

For the different populations detailed in Sect. 6 (colour lines in Fig. 7), the samples with younger ages have distributions that,

[4] We use a different notation compared to **?** to distinguish with the vertical cylindrical coordinate Z.

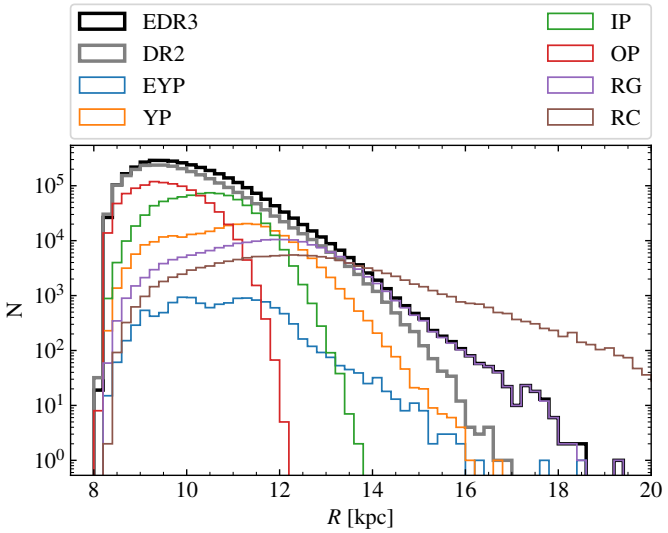

Fig. 7. Distribution of stars in Galactocentric radius. Number of stars per radial bin of 200 pc width for the whole AC20 sample with $\varpi/\sigma_\varpi > 3$ for EDR3 (black line) and DR2 (grey line), as well as for each stellar population (colour lines as indicated in the legend). The RC do not have the constraint $\varpi/\sigma_\varpi > 3$ and that is why there appear more sources than in the black distribution at larger radii.

as expected, extend to larger radii compared to older populations. The distribution for the whole sample with $\varpi/\sigma_\varpi > 3$ is dominated by dwarfs for $R < 12$ kpc while giant stars take over beyond that. We see some hints of an over-density at around 12 kpc for the EYP, YP and IP that could be due to the Perseus spiral arm but a good assessment of this requires more investigations of the selection function and the extinction. For the RC whose distances are computed photometrically without the $\varpi/\sigma_\varpi > 3$ constraint (brown dashed-dotted line), there is a larger number of stars at large distances compared to the whole sample with $\varpi/\sigma_\varpi > 3$ (black line).

For the velocities, we compute V_ℓ and V_b and correct them for the reflex of the solar motion using the following equations:

$$V_\ell = kd\mu_\ell - U_\odot \sin(\ell) + (v_{c,\odot} + V_\odot)\cos(\ell) \quad (4)$$

$$V_b = kd\mu_b + [-U_\odot \sin(\ell) - (v_{c,\odot} + V_\odot)\cos(\ell)]\sin(b) + W_\odot \cos(b) \quad (5)$$

where $k = 4.7404705$ is the usual factor for units conversion, and we assume $U_\odot = 11.1$, $v_{c,\odot} + V_\odot = 248.5$, $W_\odot = 7.25$ km s^{-1} for the solar motion (**??**), where $v_{c,\odot} \equiv v_c(R = R_\odot)$ is the value of the rotation curve at the Sun's position. In the anticentre direction, V_ℓ and V_b are approximately aligned with the usual cylindrical velocities V_ϕ and V_Z and, thus, we use:

$$V_{\phi}* \equiv V_\ell \quad (6)$$

$$V_Z* \equiv V_b \quad (7)$$

We note that V_ϕ^* is not exactly equivalent to V_ϕ, nor is V_Z^* to V_Z, due to a geometric difference in the vector orientation and the contribution of the line-of-sight velocity, but the differences are small in the anticentre. In the Appendix E we have used GOG to quantify this and we find that 80% of the sources with $\varpi/\sigma_\varpi > 3$ have absolute differences smaller than 2.9 and 3.3 km s^{-1} for $V_{\phi}*$ and V_Z*, respectively (Figs. E.4, E.5 and E.3). We see that V_ϕ^* is mainly larger than V_ϕ (but note that V_ϕ is defined negative for disc stars) with a median of 0.4 km s^{-1}. When examining how these differences are distributed in the ℓ-b projection, we see, as expected, larger differences in V_ϕ^* the farther from the exact anticentre line ($\ell = 180$ deg). The differences in V_Z^* show a quadrupole symmetry, indicating that any kinematic signature following this same shape in the sky would be clearly suspicious but that for most of the cases, since we average over the whole area, the global effect of these differences is null. For stars in the Gaia 6D phase space sample (thus a more realistic case), the differences are similar though slightly larger (80% of the stars with $\varpi/\sigma_\varpi > 3$ have absolute differences smaller than **3.2** and 4.0 km s^{-1} for $V_{\phi}*$ and V_Z*, respectively).

Another reference system for the velocities that we use in Sect. 5.1 is the tangential velocity V_t defined as:

$$V_t \equiv kd\sqrt{{\mu_\alpha*}^2 + {\mu_\delta}^2} \quad (8)$$

where in particular for that section we use as distances the inverse of the parallax with a more strict selection of $\varpi/\sigma_\varpi > 5$.

We have used the Jacobian matrix to compute the errors in the positions and velocities from the errors (and correlations) of the astrometric quantities. We neglect the errors in the angular positions since they are extremely small. In the case of the Bayesian and photometric distances, no correlation between distance d and proper motions μ has been considered (but see discussion Appendix C). Figure 8 shows the median uncertainty in the radius R (top) and velocities (bottom) as a function of R for EDR3 (solid lines) for the AC20-$\varpi/\sigma_\varpi > 3$ sample, and the area delimited by the 25 and 75 percentiles (shaded regions). The median errors in R (solid blue line) remain lower than 1 kpc for $R < 16$ kpc and the velocity uncertainties (solid orange and green lines) are smaller than 5 and 2 km s^{-1} for V_ϕ^* and V_Z^*, respectively, for most of the radii probed. The slight change of trend in the solid curves at around 12 kpc is due to the contributions of different stellar types, in particular giants stars that are intrinsically brighter at a given R and have, thus, smaller astrometric uncertainties. Table 4 gives a summary of these position and velocity errors: 80% of stars have errors < 0.6 kpc in Galactocentric radius, and < 7 km s^{-1} and < 4 km s^{-1}, respectively for V_ϕ^* and V_Z^*. We note that the errors for V_Z^* are smaller than for V_ϕ^* due to the better alignment of μ_b with $\mu_\alpha*$ which in turn has smaller errors than μ_δ as seen in Sect. 2.3 (Fig. E.1).

Table 4. Uncertainties in phase space coordinates for the different *Gaia* releases. In the first rows we show the median uncertainties (first three numerical columns) and upper limit uncertainty for 80% of stars (three columns from the right) for stars in the AC20-$\varpi/\sigma_\varpi > 3$ sample for DR2 (first row), for the stars from EDR3 in common with DR2, and for EDR3. The last rows compare the heliocentric velocity uncertainties in DR2 and EDR3 for the sample with 6D velocities (6dsample) when the error in $v_{\rm los}$ is not (left) and is considered (right).

	AC20-$\varpi/\sigma_\varpi > 3$					
	median			80% of sources		
	ϵ_R	$\epsilon_{V_\phi^*}$	$\epsilon_{V_Z^*}$	ϵ_R	$\epsilon_{V_\phi^*}$	$\epsilon_{V_Z^*}$
DR2	0.30	3.8	2.2	<0.57	<8.4	<4.6
EDR3 ($\cap$ DR2)	0.18	2.4	1.3	<0.44	<5.9	< 3.1
EDR3	0.29	3.1	1.7	<0.58	<7.3	< 3.9
	6dsample					
	median $\epsilon_{v_{\rm los}} = 0.$			median		
	ϵ_U	ϵ_V	ϵ_W	ϵ_U	ϵ_V	ϵ_W
DR2	0.09	0.09	0.07	0.43	0.44	0.38
EDR3	0.04	0.04	0.04	0.38	0.39	0.34

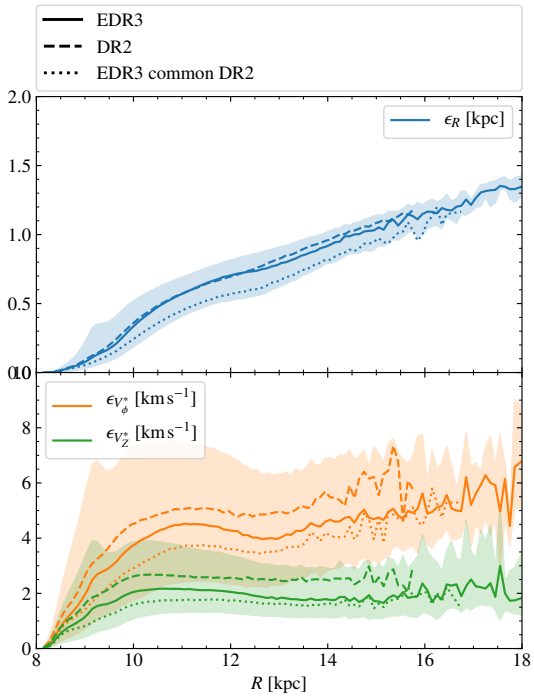

Fig. 8. Errors in phase space coordinates in the anticentre. The curves are for the AC20-$\varpi/\sigma_\varpi > 3$ sample and show the median errors for R (blue) in the top panel, and V_ϕ^* (orange) and V_Z^* (green) in the bottom panel, while the shaded regions show areas enclosing 50% of the stars (that is, limited by the 25 and 75 percentiles). We show the values for EDR3 (solid), DR2 (dashed) and sources in common (dotted).

In Fig. 8 we also show the equivalent errors in DR2 (dashed lines). However, a fair comparison to demonstrate how the uncertainties have improved in EDR3 requires that we compare the common sources (otherwise the new sources of fainter magnitudes at each bin in R contribute in a negative way to the overall values). The dotted lines obtained for the sources of EDR3 in common with DR2 show a quite significant improvement. For the velocities, the uncertainties are now smaller by about $\lesssim 2\,\mathrm{km\,s^{-1}}$ at a Galactocentric distance of $R = 12\,\mathrm{kpc}$, which represents an improvement of 30%.

Figure 9 shows the full error ellipses for a few stars chosen to sample different values of R in the R-V_ϕ^* projection that we explore later in our analysis. While the black error bars show the errors on the individual quantities, the error ellipses show large correlations between these two variables. This correlation is mostly induced by the coordinate transformations, which in both cases have an approximately linear dependency with the distance error. As expected, the ellipses are all oriented pointing towards the position of the Sun and the Local Standard of Rest assumed (LSR, indicated with a black star).

Finally, another good illustration of the improvement in the astrometry is the comparison of the uncertainties in the heliocentric velocities U, V and W for the 6dsample in DR2 (**?**) and EDR3 (**?**), which is shown in the last three rows of Table 4. Assuming that there are no **line-of-sight** velocity uncertainties, the median uncertainties (left columns) are reduced by around 50% in EDR3. Including the **line-of-sight** velocity uncertainties (rightmost columns) does not show such a reduction, highlighting that the **line-of-sight** velocity uncertainties dominate. This will change in DR3 where these uncertainties are expected to decrease substantially and millions of additional sources will have **line-of-sight** velocity measurements for the first time.

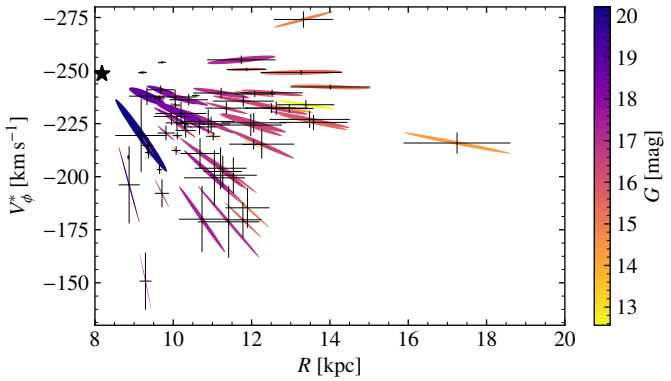

Fig. 9. Error ellipses in the R-V_ϕ^* plane for stars in the anticentre. The ellipses have been drawn for 60 stars from the AC20-$\varpi/\sigma_\varpi > 3$ sample chosen randomly but with weight of R^7 in order to sample different R. The ellipses are coloured by magnitude G and the error bars are included as black lines. The error ellipses are oriented pointing towards the $R_\odot$-LSR point (black star).

4. Disc kinematics

In this section we explore the dynamics of the Milky Way disc, analysing the velocities as a function of positions. As seen in Sects. 2.3 and 3.3, the improvement in the EDR3 astrometry allows us to probe the disc's outer regions. We start by examining the median velocities and velocity dispersions (Sect. 4.1) as a function of Galactocentric radius. We then look at large scale velocity asymmetries and phase space correlations in Sect. 4.2, to end with the analysis of small scale velocity substructures (Sect. 4.3) that are now resolved for the first time.

4.1. Azimuthal and vertical velocities and dispersions

We measure the median velocity profiles and dispersions (standard deviation with median velocity errors subtracted quadratically) of V_ϕ^* and V_Z^* for each stellar population. The outer edge of a given radial bin is automatically adapted, and found as soon as minimum thresholds for both the number of stars per bin and the size of the bin are exceeded. These thresholds are 200 stars inside of a 200 pc-wide bin for $R \leq 15$ kpc, and 50 stars within 500 pc for $R > 15$ kpc. In a given bin, we then discard outlying velocities by performing a $\pm 3\sigma$ clipping with respect to the median velocity of the bin. This procedure removes between 2.5 and 4% of stars from the initial subsamples, and is necessary to avoid strong bin-to-bin variation of the velocity dispersion profiles. The uncertainties are then obtained by performing 1000 bootstrap resampling of these distributions at each radius, choosing the 16th and 84th percentiles.

The rotation velocity curves for the different populations are shown in the top left panel of Fig. 10. A difference in the median V_ϕ^* is observed for the different stellar populations with the older stars rotating slower as a result of the asymmetric drift. On average, the EY stars rotate $\sim 11\,\mathrm{km\,s^{-1}}$ faster than the OP or the RC, with a maximum velocity difference of $\sim 18\,\mathrm{km\,s^{-1}}$ at the last radial bin of the OP curve. This is consistent with the expectation that younger stars rotate as fast as the cold interstellar gas, thus at velocities closer to the true circular velocity of the Milky Way. The curve of the EY stars presents the best agreement with the rotation curve (black dashed lines) derived in **?** from a compilation of kinematic data from molecular gas and stars in the infrared. Globally, all the rotation curves decline for $R \lesssim 9.5$ kpc and show a bump at 10.2 kpc (though not resolved

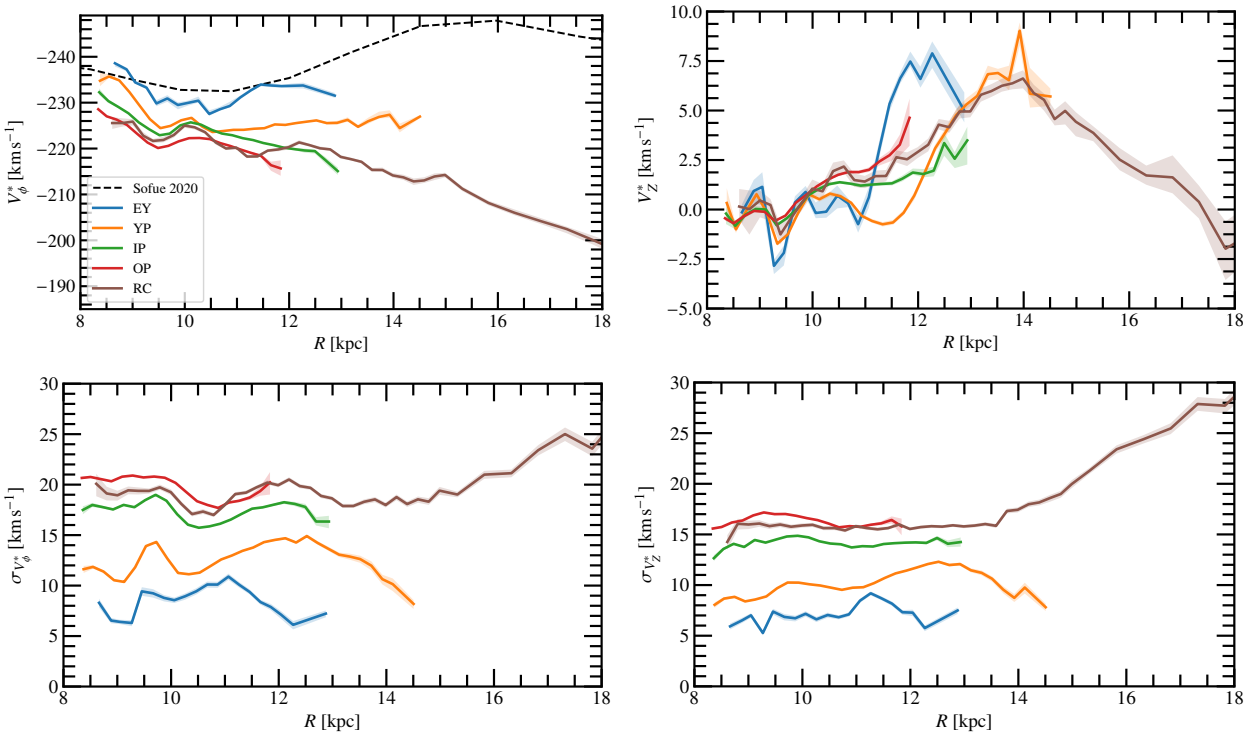

Fig. 10. Rotation and vertical velocity profiles in the anticentre. Top: Median azimuthal and vertical velocities of the populations EY, YP, IP, OP and RC as indicated in the legends (same as in Fig. 7). Shaded areas represent the uncertainties (see text) **but they are very small and barely visible in most of the cases**. The rotation curve by **?** is over-plotted in the top left panel. Bottom: Same as top but for the velocity dispersions. Apart from the expected differences due to the different ages of the populations and the asymmetric drift, we see significant oscillations in all curves.

for the EY stars due to low number statistics). Beyond $R \sim 10$ kpc, the curves of YP stars is flat, while those of older stars decrease again.

The effects of the parallax zero point are examined in Appendix D where we show, as an example, the effects of the different adopted values of this offset on the rotation curve of our AC20-$\varpi/\sigma_\varpi > 3$ sample as an example (Fig. D.2). As expected and discussed in Sect. 3.1, we see slight differences in the curves mostly due to a decrease of the distance and scaling of the velocities when the correction is used compared to when it is not used. However, the general features of the curves remain the same.

Interestingly, we observe stars from the YP rotating as far as 14.5 kpc from the Galactic centre (see also Figs. 7, 11 and 15). In total, we find as many as 269 stars with $16 < R < 18$ and $|V^*_\phi| > 190$ kpc for the $ZP = 19\,\mu$as (with median uncertainties of $\epsilon_R = 1.1$ kpc), and 162 for the case of ZP_{56}. This establishes a lower limit to the disc size although a more detailed analysis is required, in particular in the context of the selection function and the biases of the distance estimators, which can be very large at these distances (see Fig. C.4).

The top right panel of Fig. 10 shows the median vertical velocities. These velocities appear to have small oscillations of the order of 2 km s^{-1} inside $R \sim 12$ kpc. There are clear dips at $R \sim 9.3$ kpc, coinciding with the dip in V^*_ϕ, and at $R \sim 11$ only for the young stars (EY, YP). The first dip has clearly larger amplitude the younger the stars are. Beyond the location of the dips, V^*_Z increases and stars move in median upwards ($V^*_Z > 0$). The profiles of EY and RC stars draw a clear wiggle (with a subsequent decrease), with maxima of ~ 7.5 km s^{-1} at $R \sim 12$ kpc and ~ 6 km s^{-1} at $R \sim 14$ kpc, respectively. There is a hint of wiggle for YP stars, despite a spike at $R \sim 14$ kpc. In Fig. 14 of **?** only the first part of this positive vertical velocity wiggle was observed and seemed to have certain dependencies on the Galactic azimuth ϕ and vertical position Z of the stars as we will confirm in Sect. 4.2. **The oscillations and the outer increase of the vertical velocities were also observed in ?, ? and ? but as a function of angular momentum (equivalent to R, see also Sect. 4.2).**

The bottom panels of Fig. 10 show the diversity in the velocity dispersions $\sigma_{V^*_\phi}$ and $\sigma_{V^*_Z}$ in the Galactic anticentre direction. Although we expect decreasing dispersions with R (**?**, and references therein) supported by observations in external galaxies (**?**) and also the Large Magellanic Clouds in the *Gaia* data (**?**), the general behaviour here shows bumpy dispersions in all the populations studied that correlate with the oscillations in the median velocities, especially in $\sigma_{V^*_\phi}$.

Apart from the oscillations, overall we observe dispersions that are quite flat as a function of R, and even increasing at larger radii for RC stars. We note that the geometry of our AC20-$\varpi/\sigma_\varpi > 3$ samples have larger ranges of Z for increasing R (Fig. E.2). This together with a complex selection function in the more distant regions and the approximation in the velocities of Eqs. 6 and 7 could increase artificially the velocity dispersion. We suspect that this is the case of the RC sample that shows a lack of stars at $Z \sim 0$ for large R. The flattening could also be due to the flare of the Galaxy. A similar flattening of the vertical velocity dispersion outside the solar radius was observed in **?** where the authors also discuss different biases that could explain this behaviour but also the possibility of being related to the flare (see also **??**).

As for the amplitude of the dispersions, younger stars unsurprisingly present lower velocity dispersions than more evolved stars, because these populations have not had the time to be heated by various internal and external processes, unlike older populations. On average, the **azimuthal** and vertical velocity dispersions of the EY stars are 11 and 9 $\mathrm{km\,s^{-1}}$ lower than those of OP and RC stars, respectively.

The flattening of the velocity ellipsoid $\sigma_{V_Z^*}/\sigma_{V_\phi^*}$ inside $R \sim 14.5$ kpc is homogeneous among the various populations and within the whole sample, all of them showing a **azimuthal** dispersion larger than the vertical component ($\sigma_{V_Z^*}/\sigma_{V_\phi^*} = 0.7-0.8$, on average). The vertical random motion only exceeds the **azimuthal** component for RC stars beyond 15 kpc, and for EYP stars at $R = 9$ kpc. Interestingly, the random motions of the EY stars (with values of 8.5 and 7 $\mathrm{km\,s^{-1}}$ for $\sigma_{V_\phi^*}$ and $\sigma_{V_Z^*}$ on average, respectively) are comparable to the the typical velocity dispersions seen in the gas ($\sim$ 9 and 4.5 $\mathrm{km\,s^{-1}}$ respectively for neutral atomic and molecular gas for $R < 8$ kpc, **?**), for a gas velocity ellipsoid assumed isotropic. If this assumption is correct, the maximum age of 200 Myr for the Extremely Young stars in the AC20 sample is thus an upper limit for the timescale during which the velocity ellipsoid of the most recent stars would turn from isotropic to anisotropic.

4.2. Velocity correlations and asymmetries

We study here kinematic differences as a function of the location with respect to the Galactic mid-plane, and other phase space correlations. First, we compare the kinematics of $Z < 0$ stars with those at $Z \geq 0$ for the whole AC20-$\varpi/\sigma_\varpi > 3$ sample (Fig. 11). We note that the velocity dispersion for all AC20-$\varpi/\sigma_\varpi > 3$ stars has a decreasing profile for V_ϕ^* (bottom left panel) as a function of R, which is not what we see in the bottom panels of Fig. 10, when we divide the sample into populations. This is probably because our selection is biased to different relative weights of the populations as a function of radius, and these have different heating histories.

There is a notable asymmetry in the median velocities and the velocity dispersions (Fig. 11), starting approximately at 10-11 kpc, thus coinciding with the starting position of the large vertical velocities of Fig. 10. The rotation of $Z < 0$ stars (blue curves) clearly leads that of stars at $Z \geq 0$ (orange) beyond $R \sim 11$ kpc typically by up to 10 $\mathrm{km\,s^{-1}}$. A significant asymmetry is also seen for $R > 10$ kpc in the vertical motion where stars at $Z < 0$ move at larger velocities than $Z \geq 0$ stars, with a difference of up to ~ 6 $\mathrm{km\,s^{-1}}$ (already noticed in **?** and **?** for example). The asymmetries in V_Z^* start close to the Sun, though with opposite trend compared to $R > 10$ kpc. The **azimuthal** random motions are comparable at lower **radii** but asymmetric beyond $R \sim 10.5$ kpc (larger values for $Z < 0$ stars, by up to 2-4 $\mathrm{km\,s^{-1}}$). There is also a vertical velocity dispersion asymmetry but it is weaker ($\lesssim 1$ $\mathrm{km\,s^{-1}}$). In any case, the dispersions observed correspond to the typical thin disc velocity dispersions (e.g. **??**).

We now follow up these asymmetries by looking with more detail at the density of stars in the V_ϕ^*-V_Z^* plane. We show the counts in this projection in 1 kpc-wide radial bins for Galactocentric distances ranging from 10 kpc to 15 kpc, and for the north ($Z > 0$, top) and south ($Z < 0$,bottom) Galactic plane (Fig. 12). One of the clearest features in Fig. 12 is the lack of symmetry for stars above and below the plane. Secondly, for the bins **at** $R > 12$ kpc we observe a bimodality where stars are sitting mainly in two clumps, one with negative V_Z^* at lower $|V_\phi^*|$, which is more prominent in the north, and one with positive V_Z^* at higher $|V_\phi^*|$, more conspicuous in the south. The different proportions of the clumps of the bimodality at different Z seems to be the cause of the vertical asymmetries seen at the top panels of Fig. 11, moving the median velocities to higher/lower V_ϕ^* and higher/lower V_Z^*. However, we emphasise that the bimodality appears on both sides of the disc, just in different ratios.We also note that some hints of this bimodality were seen in the maps of e.g. **?** and **?** but those reach only 12 kpc from the Galactic centre and the bimodality appears marginally at the borders of their distributions.

Figure 13 shows other phase space projections, allowing us to study this **phenomenom** in a more continuous way: the top panels show V_ϕ^* as a function of R, color-coded by either the Z position (a), the median V_Z^* (b) or the median $\sigma_{V_Z^*}$ (c). **At R>11 kpc,** the population having large $|V_\phi^*|$ (~ 30 $\mathrm{km\,s^{-1}}$ larger than the other group) and positive V_Z^* (~ 10 $\mathrm{km\,s^{-1}}$, blue colours in panel b) is predominantly at negative Z (red colours in panel a), and vice-versa for the population having smaller $|V_\phi^*|$ and negative V_Z^* (of about -2 to -5 $\mathrm{km\,s^{-1}}$), as seen before. Additionally, we note now a clear spatial evolution, with the region at large $|V_\phi^*|$ and positive V_Z^* smoothly diminishing its $|V_\phi^*|$ when R increases. A line of constant angular momentum $L_Z = -2750$ $\mathrm{km\,s^{-1}}$ kpc has been plotted that roughly marks the transition in the sign of V_Z^* in panel b. There is not an exact match between the transition zone in panels a and b, indicating that the dominance of one clump over the other does not occur exactly at $Z = 0$. We note that the velocity dispersion of both groups of stars is typical of the thin disc ($\sigma_{V_Z^*} \sim 15$ $\mathrm{km\,s^{-1}}$), as already inferred from the bottom-right plot of Fig. 11.

The phase spiral identified in **?** with DR2 data for stars in the immediate Solar vicinity (within $\boldsymbol{R_0} \pm 200$ pc), is illustrated in panel d of Fig. 13 now with astrometry from EDR3. The morphological change of this phase spiral (or more precisely a slice of it, centred around $Z \sim 0$ kpc, highlighted with brighter colours in panel d) is traced at larger radii in panel e, by plotting V_Z^* as a function of R color-coded by V_ϕ^*. Up to $R \sim 11$ kpc, one can still see the different arms of the phase spiral at positive and negative V_Z^*, with a diminishing envelope as one moves outwards, due to smaller restoring forces. While this has been observed already in **?** for discrete ranges of R, we see it here in a continuous way. However, farther out than $R \sim 12$ kpc, we see a clump (red colours) of large $|V_\phi^*|$ and positive V_Z^* dominating, which corresponds to one of the modes of the bimodality discussed above. Whether this is a manifestation of the same or another phase spiral at larger radius or a different phenomenon (although perhaps with the same origin) is not clear at this point, especially given the complex cone geometry of the AC20-$\varpi/\sigma_\varpi > 3$ sample and the distance and velocity errors, which might blur any thinner substructures.

In Appendix E we repeat some of the plots presented thus far for the GOG and UM samples. From those we conclude that selection effects due to extinction can induce some features in projections such as R-V_ϕ^* coloured as a function of Z. This is because a different extinction below and above the plane favours distinctly the different types of stars (different ages) that have different asymmetric drift (thus different V_ϕ^*) creating correlations between these variables. However, we do not observe any special vertical kinematics for these features in the mock data. We have also checked that the effects of the zero point in parallax does not induce or remove the features observed but merely change the distance scale with the pattern arriving farther or closer, independently whether a constant ZP or ZP_{56} is used (Fig. E.6

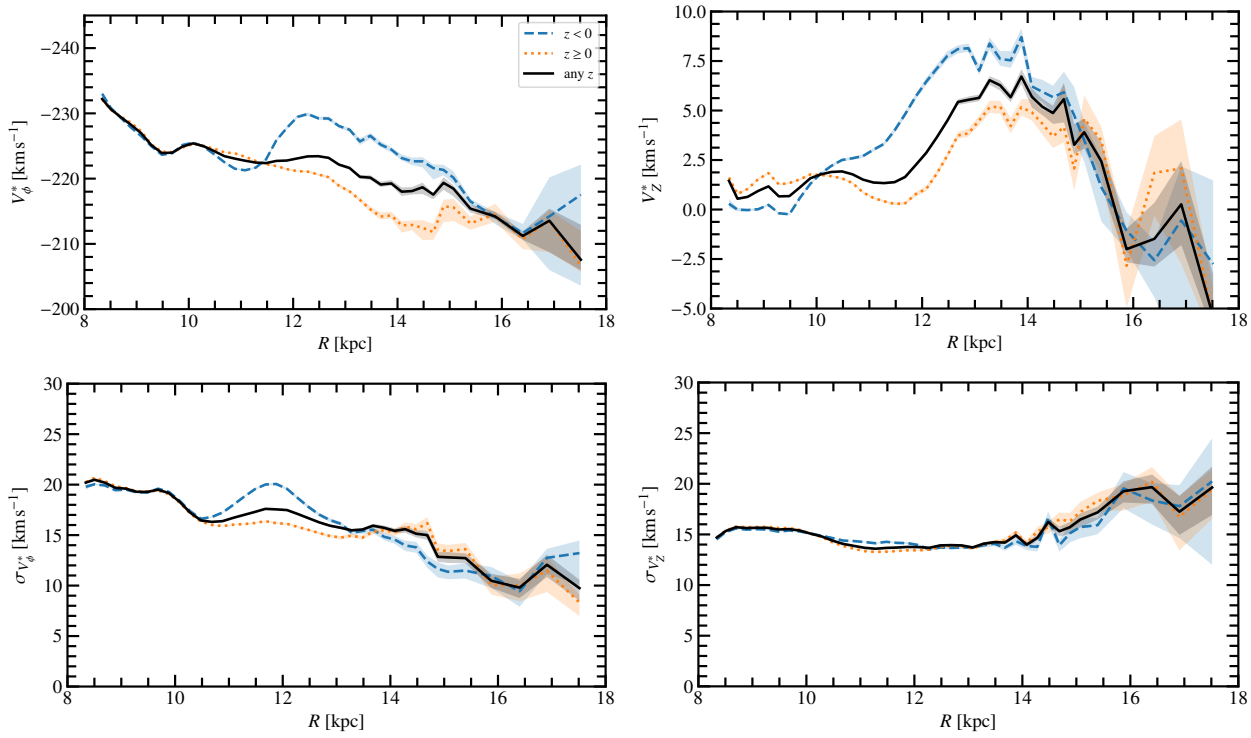

Fig. 11. Comparisons of the velocities above and below the Galactic plane. We plot the median azimuthal and vertical velocities (top) and velocity dispersions (bottom) for the whole sample AC20-$\varpi/\sigma_\varpi > 3$ (solid black lines), and for stars with $Z \geq 0$ (orange dotted lines) and for $Z < 0$ stars (blue dashed lines). Shaded areas represent the uncertainties. We observe notable asymmetries beyond 10-11 kpc.

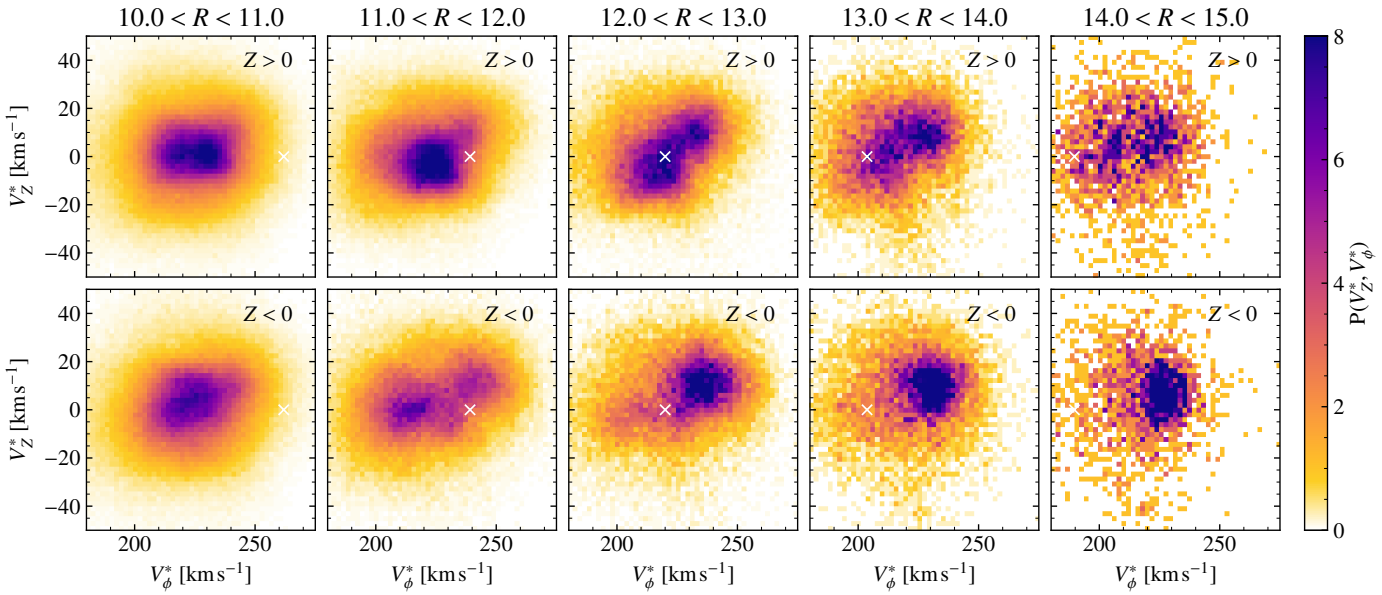

Fig. 12. Density in velocity space at different distances above and below the plane. Stellar density in the $V^*_\phi - V^*_Z$ plane, for bins in R from 10 to 15 kpc for the AC20-$\varpi/\sigma_\varpi > 3$ sample for $Z > 0$ (top) and $Z < 0$ (bottom). We see division into two components in the outer radial bins. To guide the eye a cross has been placed at V^*_ϕ corresponding to $L_z = -2750$ km s^{-1} kpc for a point in the centre of the radial bin (see also Fig. 14).

in Appendix E). Moreover, these features preferentially occupy positive or negative Galactic latitudes but do not correlate with the smaller scale checkered patterns seen in the astrometry. We note also that the stars participating in this phenomenon are relatively bright stars (Fig. E.7 in the Appendix E), thus with good astrometry in general. Also the difference of 10 km s^{-1} seen in the velocities of the two distinct features mentioned above which are at a typical distance of 4 kpc, correspond to a proper motion difference of around 0.5 mas yr^{-1}, which is much bigger than any known systematics.

Finally, Fig. 14 shows the angular momentum-vertical velocity (L_z, V^*_Z) space, **coloured by column density (top) and average Z coordinate (bottom).**In this plot, we see oscillations in V^*_Z for the smaller $|L_z|$ **(seen also in ? and ?)** that most likely

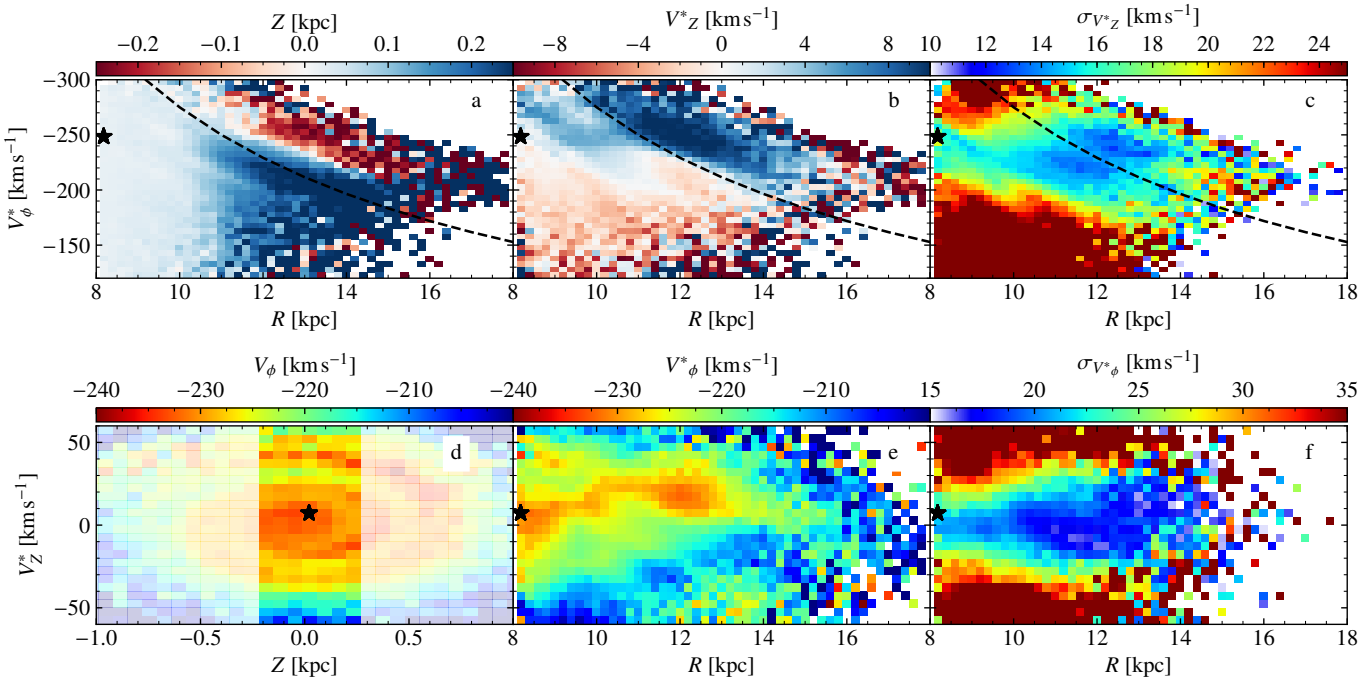

Fig. 13. Phase space projections of the Galaxy disc. The plots show for the AC20-$\varpi/\sigma_\varpi > 3$ sample: a) median Z coordinate in the R-V^*_ϕ plane; b) median vertical velocity V^*_Z in the same projection; c) dispersion in the V^*_Z velocity in the same projection; d) phase spiral in the 6dsample in EDR3 for stars in the Galactic radial range $|R - \boldsymbol{R_0}| < 0.2$ kpc; e) median azimuthal velocity V^*_ϕ in the R-V^*_Z plane; f) dispersion in V^*_ϕ in the same plane. The bimodality appears in the outer parts of the disc in panels a, b and c, with the separation marked with a line of constant angular momentum $L_z = -2750\,\mathrm{km\,s^{-1}}$ kpc. In pane e, the evolution of a slice of the phase spiral (marked in brighter colours in panel d) is seen for **smaller radii**, while a signature related to the above bimodality is seen beyond ~ 12 kpc in panels e and f.

correspond to the vertical oscillations also seen in the bottom panel of Fig. 10 at nearby Galactocentric radii. Most notably, these plots show that the clumpy features seen for $R > 11.5$ kpc in Fig. 12 correspond to a clear break in the (L_z, V^*_Z) **density** at $\sim -2750\,\mathrm{km\,s^{-1}}$ kpc rather than a smooth transition. We note that when we separate our sample into young population (YP+EY), Main Sequence (IP+OP) or Giants (Fig. E.8 in Appendix E), this trend is seen for all the populations (albeit most clearly in the young one, as it has the lowest velocity dispersion) implying that this break is most likely of dynamical origin. In particular, the change in proportions between the two populations that we see in Fig. 12 as we move outwards is related to the fact that the population with $|L_z| \lesssim 2750\,\mathrm{km\,s^{-1}}$ kpc (and $V^*_Z < 0$) does not reach as large radii as the population with $|L_z| \gtrsim 2750\,\mathrm{km\,s^{-1}}$ kpc (and $V^*_Z > 0\,\mathrm{km\,s^{-1}}$). According to the bottom panel of Fig. 14, and as seen above, the part of the disc at lower angular momentum $|L_z|$ corresponds to stars predominantly at positive Z while the one with higher $|L_z|$ mostly has negative Z, though without perfect one-to-one correlation.

4.3. Small scale velocity structures

Apart from the two clumps discussed in Sect. 4.2, finer substructures in the phase space of the disc can already be seen in the top panels of Fig. 13 for nearby radii. These structures are better visualised in Fig. 15 showing the 2-dimensional histogram of the V^*_ϕ-R projection (panel a). Diagonal ridges, i.e. substructures with decreasing $|V^*_\phi|$ as a function of R, can be seen, as already discovered in the *Gaia* DR2 (**??**). To enhance the contrast of these substructures, in panel b we show the density relative to a smoothed density obtained from a Gaussian filter ($\frac{N-N_s}{N_s}$, where N are the counts and N_s are the smoothed counts with a $\sigma = 5$ times the bin size, similar to what is done in **?**). Panels c to e show this relative density for different stellar types. We do not note any difference between using $Z = -19\,\mu$as and Z_{56} except for the already mentioned distance scaling.

The location of the main ridges obtained in **?** with the DR2 *Gaia* RVS sample are over-plotted with colour lines in Fig. 15b-e. We can identify the ridges associated to Hercules, Hyades, L18 (with a different slope compared to the rest) and one that could be linked to L16 or the so called hat (e.g. **?**, $V \sim 40\,\mathrm{km\,s^{-1}}$ on their figure 22) - also related to L14 and L17. Interestingly, for the YP the Sirius ridge appears to have slightly higher $|V^*_\phi|$ velocities than the marked ridge (red line), as if following the asymmetric drift relations, and the ridges look thinner **than in** the RG or RC **plots**. **We estimate the fraction of stars forming the ridges by calculating $\frac{\sum(N-N_s)>0}{\sum N_s}$. This fractions are 44%, 16%, 10%, 9% for the EY, YP, IP and OP, respectively. The fractions are 14%, 12% and 8% for the RG, RC and all AC20-$\varpi/\sigma_\varpi > 3$ stars, respectively. This fraction depends on the σ used to smooth the distribution but the relative trends are the same, from which we see that the younger the population, the higher the fraction of stars in substructures.** On the other hand, we do not have enough stars in the lower $|V^*_\phi|$ region in any of the populations to notice the low angular momentum ridges suggested in **?**.

In Fig. 13a, we see some correspondence between the median Z and the density ridges seen in Fig. 15 (e.g. the white ridge in panel a with lower median Z overlaps with the Sirius ridge). Similarly, in Fig. 13b the ridges exhibit a complex pattern of positive and negative vertical velocities, **thus indicating** coupling between in-plane and off-plane kinematics. These effects were also noticed in *Gaia* DR2 with the RVS sample (**??**), where the

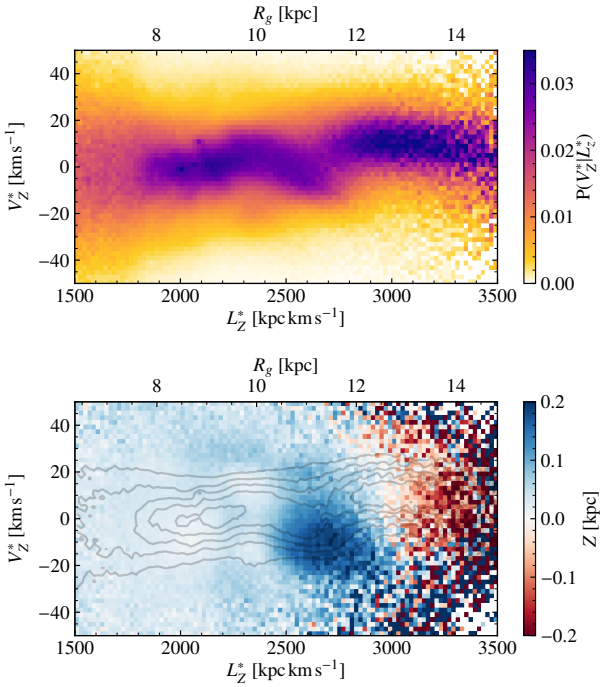

Fig. 14. Structures in vertical velocity and angular momentum. Top: Column normalised histogram of star numbers in the L_z-V_Z^* plane for the AC20-$\varpi/\sigma_\varpi > 3$ sample (the colour represents the fraction of stars in a given L_z bin that have a certain V_Z^*). Bottom: Average Z of stars in each bin in L_z-V_Z^* in our AC20-$\varpi/\sigma_\varpi > 3$ sample. Contours are the same as the colour plot in the top panel.

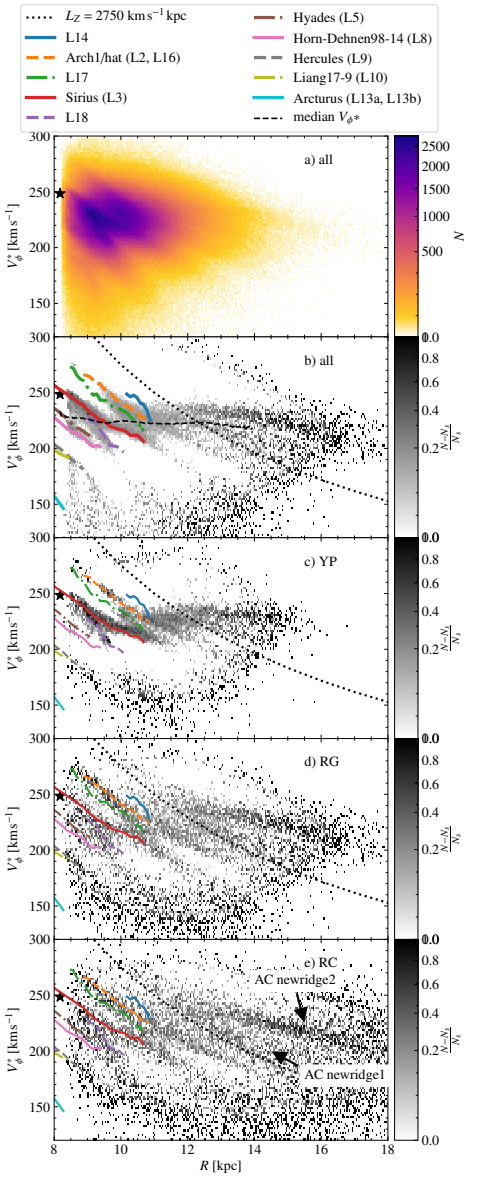

Fig. 15. Substructures in the R-V_ϕ^* projection in the anticentre direction. a) Number counts in the R-V_ϕ^* plane in bins of size $\Delta R = 0.02$ kpc and $\Delta V_\phi^* = 1$ km s^{-1} for all stars in the AC20-$\varpi/\sigma_\varpi > 3$ sample. b) Same but applying a substructure mask to highlight the ridges (see text). c-e) Same as b but for different stellar types. We also plot: some ridges from **?** with coloured lines, the separation of the bimodality (black dotted line), and the median velocity (black dashed line in panel b). We see the ridges extending beyond their limits in DR2 and new ridges resolved here for the first time.

ridges were stronger at lower $|Z|$ and had some amplitude in V_Z^* though typically lower than 5 km s^{-1}.

More importantly, in Fig. 15 the ridges are now seen at much larger distances than before. The Sirius ridge is detected up to $R \sim 12.5$ kpc, while in *Gaia* DR2 a sophisticated method to detect very low contrasts was needed to reach even $R \sim 11$ kpc (**?**). We can also spot three ridges that reach outer regions of the disc, up to 16 kpc and beyond in the case of the RC. The one at lowest $|V_\phi^*|$ could be the extension of L16. The other two were previously unknown and have been marked with arrows in the bottom panel (new anticentre ridges 1 and 2). s The new structures do not point towards $V_\phi^* \sim V_{\rm LSR}$ and $R = \boldsymbol{R_0}$ (black star in the panels) as expected for structures stretched by errors in distance (see Fig. 9). In addition, we do not see any similar ridge induced by selection effects, uncertainties, or extinction, in the GOG equivalent sample.

In the panels b to e of Fig. 15 we **also** plot the line of angular momentum $L_Z = -2750$ km s^{-1} kpc (dotted black line) which marks the approximate separation of the bimodality described in Sect. 4.2. While this line seems to coincide with the new anticentre ridge 1 (especially in panel e), **no** dynamical connection is clear at this stage. The median rotation velocities from Fig. 10 are over-plotted as a black dotted line in panel b and we see that the bump at around 10 kpc seems linked to the appearance of the L16 ridge that, with higher $|V_\phi^*|$, moves the median curve slightly upwards. The connection between ridges and bumps in the rotation curve was already suggested by **??**. The bump at 13 kpc could also be connected to the new anticentre ridge 2.

5. Halo, thick disc and distant structures

In this section, we investigate several constituents of the Galaxy through the powerful combination of *Gaia* astrometry and photometry. In Sect. 5.1 we look at the **stars** of high tangential velocity conforming the halo and the hot thick disc and secondly, in Sect. 5.2 we explore the structures in the outer parts of the Galaxy disc.

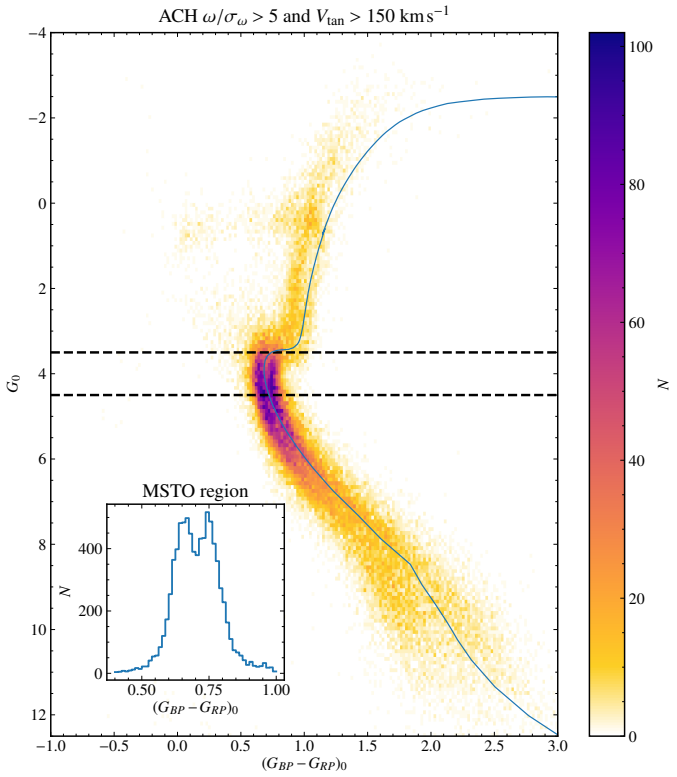

Fig. 16. Red and blue sequences for high tangential velocity stars. $G_{\rm RP} - G_{\rm BP}$ vs G Hess diagram for the ACH sample with a $\varpi/\sigma_\varpi > 5$ and $V_t > 150$ km s^{-1}. A PARSEC isochrone with [M/H] = −0.5 and age of 11 Gyr is shown in blue (but shifted by 0.04 in colour and 0.2 in magnitude in order to match the gap between blue and red sequences). The inset histogram shows the colour distribution in the magnitude range of the MSTO (shown as dashed lines in the main figure). A clear separation in two sequences is clearly seen as originally noted in **?** with DR2 data. An animated version of this figure for varying V_t limits will be available online.

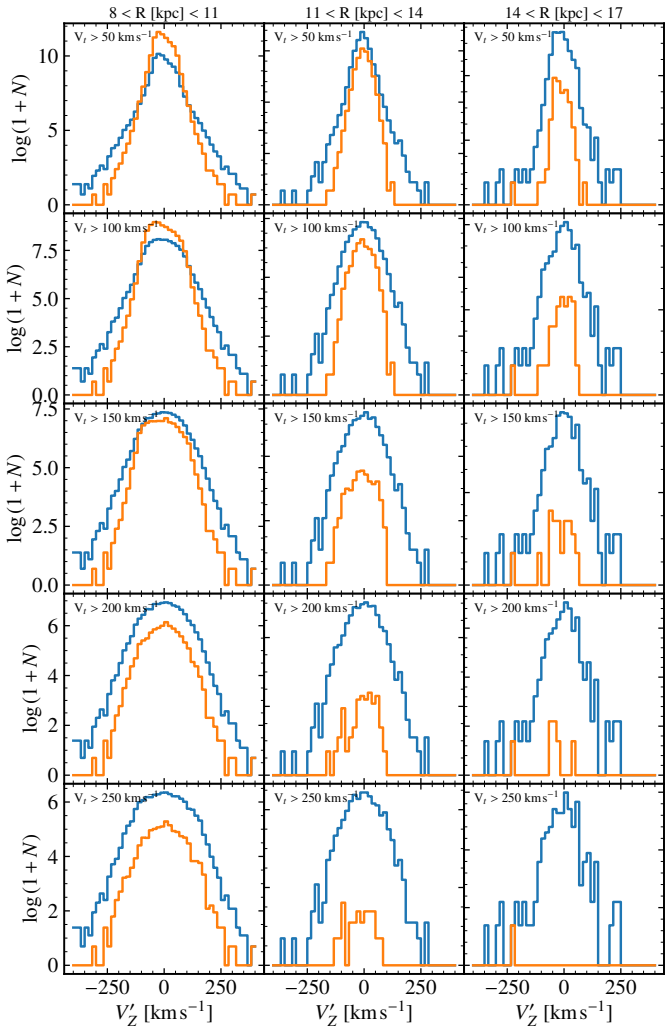

Fig. 17. Vertical velocities for the blue and red sequences. The plots are for different distance slices, indicated in the top of each column. Each row shows a different V_t selection, indicated in each panel. The blue (orange) curve shows the distribution for the blue (red) sequence. The different relative contribution of the sequences in the different panels is indicative of the spatial distribution of the accreted component and the ancient heated disc, and in particular of a shorter extent of the later one.

5.1. Halo and thick disc

Our goal in this section is to establish the extent and properties of the accreted halo and the hot thick disc populations beyond the solar vicinity and towards the galactic anticentre.

To enhance the contribution of halo stars and partially mitigate the effects of high-extinction near the disc plane, we use the ACH sample, defined in Sect. 2.2. We select on $\varpi/\sigma_\varpi > 5$ and compute distances as the inverse parallax. Since we are interested in precise intrinsic colours and magnitudes, we choose only stars that have G-band extiction $A_G < 1.0$. Here the extinction is computed using the **?** maps (with the correction of **?**) and a **?** extiction curve with $R_V = 3.1$. Although this extinction correction does not yield intrinsic magnitudes as accurate as in Appendix B, the main goal here is simply to remove high-extinction regions from our analysis, while producing accurate enough colours at large distances.

Following the approach of **?**, we focus on the HR diagram for stars in the ACH sample that pass the cuts described above. We find that when selecting only stars with high **heliocentric** tangential velocity V_t (Eq. 8), two sequences arise as shown in Fig. 16, and that at the value of $\sim$ 150 km s^{-1} both sequences seem to be found in equal numbers around the main-sequence turn-off point. For completeness, see also our animation of how the HR diagram varies as V_t is **increased** in 5 km s^{-1} slices that will be available online. When V_t is very low, there is a significant contribution from the thin and the canonical thick discs, whereas at $V_t \gtrsim 250$ km/s mainly the blue sequence (corredponding to the accreted halo) is apparent.

In Fig. 16 the double sequence extends beyond the turn-off point, but with fewer **luminous** stars in the red-sequence **than in** the blue one, suggesting that the distance distribution of the two populations is different. In order to select stars in either sequence we use a PARSEC isochrone (**??**) with [M/H] = −0.5 and age of 11 Gyr (blue line). The isochrone was shifted by 0.04 in colour and 0.2 in magnitude in order to match the gap between blue and red sequences. Notice that both the isochrone and extinction coefficients use *Gaia* DR2 transmission curves.

We now explore the dynamical distributions of the stars belonging to these two sequences in more detail. To this end we explore the velocity distribution in cylindrical coordinates, V'_ϕ and V'_Z, where the prime indicates that the line-of-sight velocity component is assumed to be zero. The ACH sample is dominated by low latitude stars for which this approximation is good enough. These velocities are vey similar to the ones defined in Eqs. 4 and

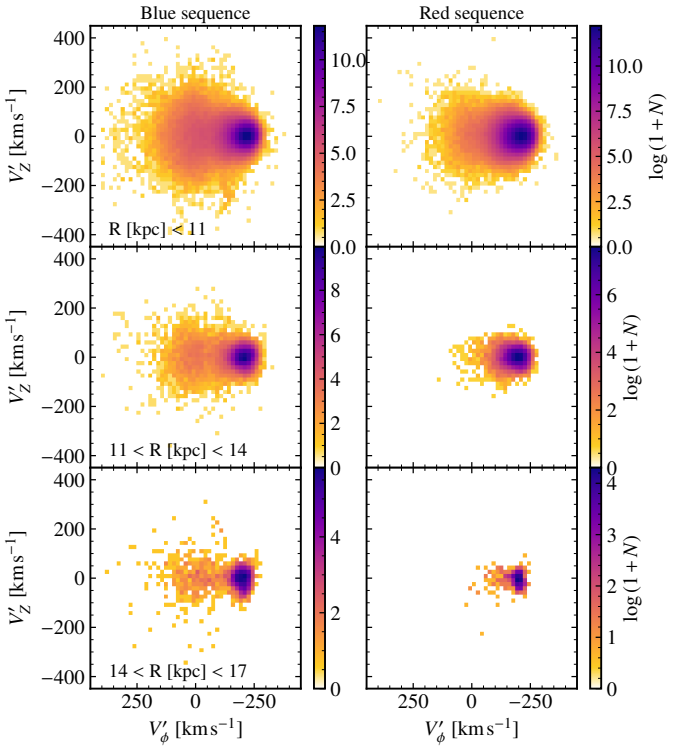

Fig. 18. Velocity distribution of the blue and red sequences. V'_ϕ vs V'_Z distribution showing in the left (right) column the stars in the blue (red) sequence. Each row shows the distributions for a given distance slice, indicated in the left panels. The stars with low rotation (even the retrogrades ones) are far more prominent in the blue sequence and extend to larger Galactocentric radii.

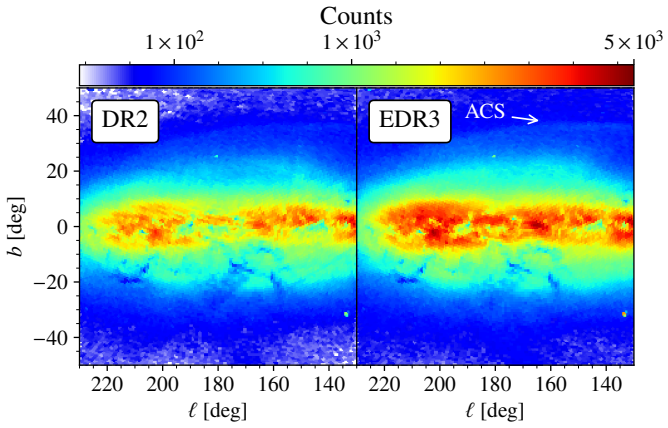

Fig. 19. Counts in the sky for a selection of stars that favours the outer disc structures. The selection is for stars with $\varpi < 0.1$ mas, $-1 < \mu_{\alpha*} < 1$ mas yr^{-1} and $-2 < \mu_\delta < 0$ mas yr^{-1}. Left: DR2 (we observe marks of the scanning law). Right: EDR3 **without filters nor parallax zero-point correction** (more stars and better homogeneity). The ACS can be seen more clearly in the right panel.

5. Fig. 17 shows the distribution of velocities perpendicular to the Galactic plane (i.e. V'_Z) for the blue and red sequence at three cylindrical galactocentric distance bins (columns) and five V_t selections (rows). We note that the red-sequence distribution, for $V_t \gtrsim 50$ km s^{-1}, is peaked for all distance bins and has a lower velocity dispersion in V'_Z, compared to e.g. $V_t \gtrsim 100$ km s^{-1}. The lower velocity dispersion results from the contribution of the canonical thick disc (with some contribution from the thin disc) while as V_t increases, the contribution of the hot thick disc becomes more important, giving rise to large wings and higher overall velocity dispersions. Note, however, that for more distant bins, the contribution of the hot thick disc becomes smaller (bottom right panels), and it is basically absent beyond 14-17 kpc (whereas the canonical thick disc still is apparent in the top panels at these radii). On the other hand, the blue sequence is apparent at all radii, has a relatively large vertical velocity dispersion, nearly always higher than that of the red sequence.

In Fig. 18 we show the V'_ϕ vs. V'_Z distribution for blue and red sequences stars for the same distance bins as in the previous figure. The densest structure at $V'_\phi \sim -220$ km s^{-1} is comprised mainly of disc stars, while the more extended and sparser structures belong to the halo and thick disc. Firstly, we note the presence of the **?** streams in the top-left panel at $(V'_\phi, V'_Z) \sim (-180, -230)$ km s^{-1} (indicating that these streams are a relatively local feature, i.e. dominant for $R < 11$ kpc, in agreement with the results and predictions of **?**). We see, however, some hints of structures at similar velocities (and mirrored ones) in the panels of more distant stars (two bottom left panels) that could potentially be related to these known streams. For the local sample (top panels) we observe higher dispersion for the radial/retrograde component in the blue sequence stars compared to the red sequence. At the intermediate distance bin (middle panels) the same holds, but the distribution of radial/retrograde red sequence stars does not extend to the low rotation region (V'_ϕ>0) as in the blue sequence, indicative of a more thick disc-like component, and consistent with our findings from the previous figure. For the most distant stars (bottom panels) the blue sequence dominates the radial/retrograde population, with the red sequence mostly appearing as a low-dispersion disc-like component.

Therefore, the analyses presented in this section show that the hot thick-disc component, associated with the heated disc at the time of the merger with Gaia-Enceladus-Sausage, has a smaller extent presently than the canonical thick disc. This indicates that the disc present at that time was smaller in size, as indeed expected from cosmological models. A more quantitative estimate of its size would require a careful assessment of the density distribution of the older stars in the red sequence, which is beyond the scope of this work. On the other hand, we see that the component associated with Gaia-Enceladus-Sausage has deposited debris out to large distances from the Sun, as we detect the presence of a retrograde component out to ~ 17 kpc from the Galactic centre.

5.2. Distant structures

Studying the outskirts of the disc is a difficult task since the anticentre is mostly **outshone** by the nearby stars which are more numerous due to both the density gradient of the Galaxy and the magnitude limitations inherent to any survey. The majority of the studies of the outer disc detected unexpected overdensities in counts **such as Monoceros and ACS** and focused on a specific stellar type, generally main sequence turn-off stars or M giants. An alternative way is now possible with *Gaia*, which allows us to detect them by applying the right astrometric selection. First, we can significantly reduce the amount of foreground contamination with a cut in parallax selecting only stars with $\varpi < 0.1$ mas. By doing so, we guarantee that most of the stars closer than 10 kpc are not selected, although the probability of failure is related to the parallax error of the source (the fainter sources being more likely to pass the filter regardless of their true distance). Then, we

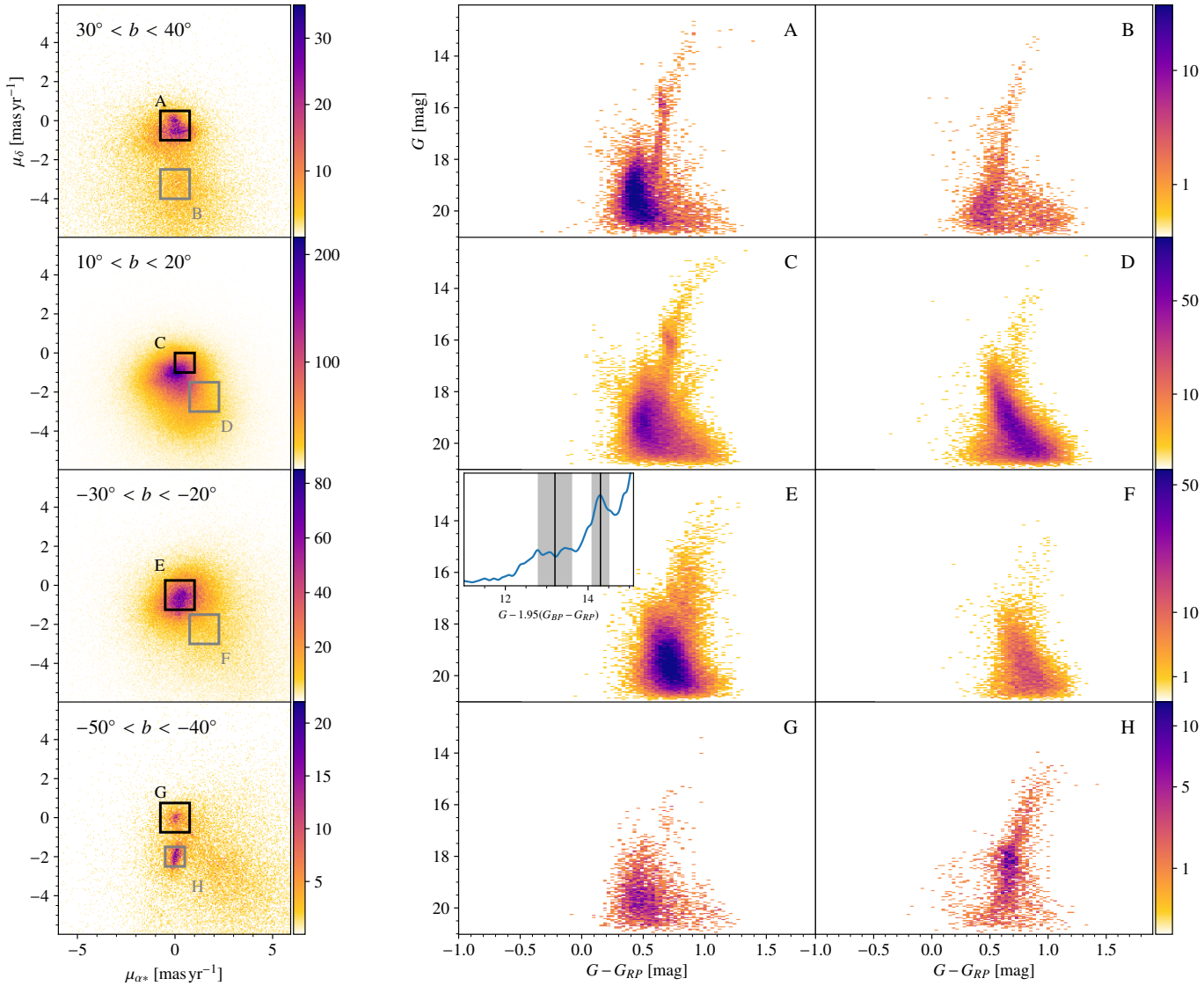

Fig. 20. Colour-magnitude diagrams of different features in the anticentre. The diagrams are for the kinematic groups selected in proper motion in the range $170° < \ell < 190°$. Each row corresponds to a different latitude. The first column shows their distribution in proper motion and the definition of two regions of interested. The stellar population in the first selection A (B) is shown in the second (third) column. We see structures such as ACS (A), Monoceros (C), the Sagittarius stream (H, C) and other outer disc structures (E).

apply a kinematic selection since the proper motion signatures of these structures, given that they are relatively far from the Sun, are significantly different from the nearby disc and halo stars. The latter tend to have large proper motions due to the large relative velocity with respect to the Local Standard of Rest, while the former also tend to have large proper motions, but in this case due to the small heliocentric distance. Figure 19 is an example of such parallax and kinematic selection ($-1 < \mu_{\alpha}* < 1$ mas yr^{-1} and $-2 < \mu_{\delta} < 0$ mas yr^{-1}) where, in contrast to Fig. 1, we can observe a perfectly defined and thin ACS**, as indicated by the arrow.** The difference between DR2 (left) and EDR3 (right) is clear: we now have more stars 7 624 697 compared to 5 951 302), mostly due to the higher completeness of stars with proper motions in EDR3, and the sample is less affected by the scanning law and other artefacts.

While Fig. 19 shows the power of *Gaia* to resolve distant structures like Monoceros and ACS, a deeper inspection of the stellar content of each structure requires a more precise selection in kinematic space. In the first column of Fig. 20 we show the proper motion histograms for different slices in latitude around the anticentre ($170° < \ell < 190°$) using the sample ACV**, now with the astrometric and photometric filters, as well as the parallax zero-point correction**. As we move from the north to the south Galactic hemisphere (top to bottom), different structures can be observed. We examine them by selecting stars in the rectangles A to H and plotting their Colour-Magnitude diagrams (CMDs) in the second and third columns using $G - G_{RP}$ instead of $G_{BP} - G_{RP}$ since, as exposed in **?** –see their Fig. 26–, the flux in the *BP* band can be overestimated for faint sources.

First, we note that the large concentration of sources close to the proper motion origin in the boxes A and G are mostly quasars for several reasons: i) they are faint and too blue, with $G - G_{RP} < 0.5$ mag, which is equivalent, incidentally, to the cut used in **?** ($g - r < 0.3$ mag) to remove the SDSS quasars[5], ii) the fraction of primary sources (`astrometric_primary_flag`), a significant fraction of which are quasars (**?**), is abnormally high

[5] We used the values in Table 5 from **?** to convert the SDSS colours to *Gaia* colours.

in both A and G, and iii) ∼30% of the sources in A and ∼25% in G are found in the CU3QS0 compilation of confirmed quasars obtained from different surveys (**?**).

More interestingly, box A contains other kinematic structures apart from the aforementioned quasars. There is a more extended giant branch formed by the ACS (c.f. Fig. 2 from **?**) and, tentatively, two fainter tips of a giant branch that could be related to the Sagittarius stream (similarly to box C, as explained below). The other box (B) at the same latitude corresponds to the distribution of halo stars, their proper motions larger due to the Sun's **reflex motion** and their CMD compatible with an old isochrone at ∼10 kpc or farther, where stars accumulate due to our parallax cut. In the second row, panel C contains parts of both Monoceros, which provides the giant branch, a well defined RC and a very blue turn-off consistent with previous observations (e.g. **??**), and the leading tidal tail of Sagittarius, which is only **evident** by its AGBs at magnitudes between 17 and 18. Boxes D and F are dominated by the disc which, after the selection in parallax, is expected to have a thick main sequence created by faint dwarfs with large parallax uncertainties, and a few Red Giants[6] above magnitude G ∼17 mag.

On the south, at latitudes $-30\,\mathrm{deg} < b < -20\,\mathrm{deg}$, we observe that the CMD of the small proper motion population is dominated by two RCs (panel E), the densest at magnitude ∼17 mag and the other at ∼15.5 mag. To confirm their existence, we have obtained the Gaussian kernel of $G^* = G - 1.95(G_{BP} - G_{RP})$, therefore marginalising the apparent magnitudes along the extinction line (see Sect. 2.4). This kernel (**shown within panel E**) presents two clear peaks corresponding to each of the mentioned RCs. By approximately selecting stars in these clumps and computing their distances assuming an absolute magnitude of the RC of $M_G = 0.495$ (**?**) and the extinction by **?** -and thus, upper limits-, we find that they are located at an average heliocentric distance of 9 and 14 kpc with variance of 3 and 2 kpc, for the bright and faint clumps, respectively. These corresponds to Galactocentric cylindrical radii of around 16 and 21 kpc, and heights below the plane of -4 and -6 kpc, respectively. With this it is very likely that the bright RC corresponds to a nearby south extension of Monoceros (**??**), alternatively called "south middle structure" (**?**), at around ∼ 12 to 16 kpc from the Galactic centre. On the other hand, the faint RC could be related to TriAnd (**????**)), at a Galactocentric radius between 18 and 25. We note however that previous TriAnd detections were located around the range 100-160 deg in ℓ, thus not exactly in the anticentre direction, and our detection would then be a confirmation of the broadness of this structure and their extension up to $\ell = 180$, albeit predicted by models such as that from **?**.

6. Clusters in the outer disc

In this section, we investigate the peculiar clusters Berkeley 29 and Saurer 1. The *Gaia* EDR3 astrometric data allows us for the first time to perform a reliable member selection of these clusters and to constrain their proper motions in order to determine their orbits. We retained all sources brighter than G=19 within 4 arcmin of the cluster centres. The members were identified from their *Gaia* proper motions and parallaxes with the unsupervised clustering procedure UPMASK (**?**). **?**, **also** using UPMASK, analysed the stars brighter than $G = 18$ mag of *Gaia* DR2 and detected Berkeley 29 but not Saurer 1. The improvement of *Gaia* EDR3 with respect to *Gaia* DR2 allows us to gain one magnitude and reliably detect both clusters. Figure 21 impressively shows how the stars in these clusters appear much more concentrated in proper motion space compared to DR2. The CMDs of the clusters are shown in Fig. 22, highlighting the sources that we consider the most secure members (with membership scores over 50%). We manually fit PARSEC isochrones (**?**) to the observed CMDs. For Berkeley 29 we employ an isochrone with a metallicity [Fe/H] = −0.5 (**??**), an age log t=9.55, and a distance modulus of 15.5 mag with an extinction A_V of 0.2 mag. For Saurer 1 we use an isochrone of metallicity [Fe/H] = −0.4 (**??**), an age log t=9.6, and a distance modulus of 15.4 mag with an extinction A_V of 0.4 mag.

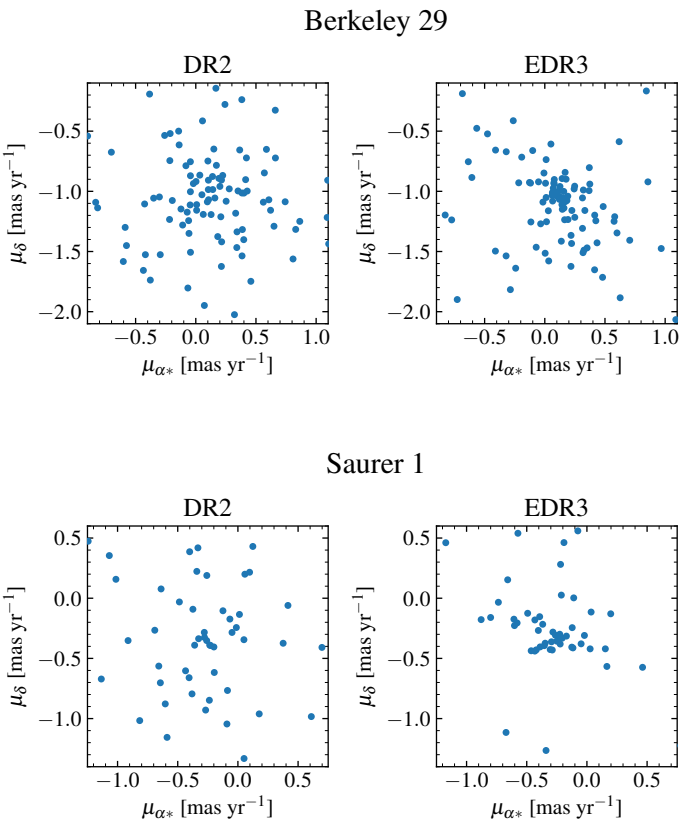

Fig. 21. Proper motions of the stars in Berkeley 29 and Saurer 1. The proper motions are for Berkeley 29 (top) and Saurer 1 (bottom) for *Gaia* DR2 (left) and *Gaia* EDR3 (right), for sources brighter than G=19 in the investigated field of view. The reduced uncertainties in EDR3 make the stars appear much more clumped than in DR2, allowing for a better selection of members and a better determination of the proper motion of the clusters.

The mean proper motions of the cluster members are $(\mu_\alpha*, \mu_\delta)$=(0.11, −1.05) mas yr^{-1} for Berkeley 29, and (−0.26, −0.32) mas yr^{-1} for Saurer 1. They are represented in Galactic coordinates $(\mu_\ell*, \mu_b)$ in the first panel of Fig. 23, along with the mean proper motion of the Sagittarius stream particles from the **?** model. In this panel, all proper motions were corrected from the effect of the Solar motion. The velocity vector of both clusters is mostly parallel to the Galactic plane, and differs significantly from that of the stream.

We used `galpy` MWPotential2014 model (**?**) to integrate the orbits of these objects, shown in the left panels of Fig. 23. For this, we supplemented the quantities derived from *Gaia*

[6] A RC star fainter than G ∼15 mag at latitudes b>10° is bound to be higher than 2 kpc from the disc, which is unlikely, but stars brighter than that tend to have a reliable parallax and are therefore more likely to be removed with our parallax cut.

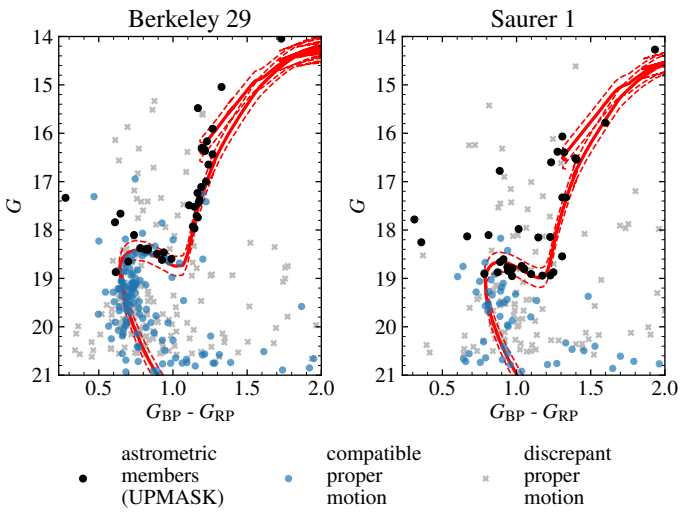

Fig. 22. CMDs for Berkeley 29 and Saurer 1. The secure members identified with UPMASK are indicated and used to compute the mean proper motions. The blue points are sources with similar proper motions but large uncertainties, or magnitudes G>19. The red lines are PARSEC isochrones. The dashed lines correspond to offsets of ±0.2 mag in distance modulus.

data with **line-of-sight** velocities obtained from high-resolution spectra analysed by **?**. Their mean **line-of-sight** velocities are 24.8 km s^{-1} for Berkeley 29 (from eight stars), and 98.0 km s^{-1} for Saurer 1 (from two stars). All the stars they used to compute those mean velocities are part of the sample of secure members we obtained in the present study. We estimated the uncertainty on the main orbital parameters by Monte-Carlo sampling of the uncertainties on the distance, **line-of-sight** velocity, and proper motion. We assume an uncertainty of 0.2 mag on the distance modulus, and 2 km s^{-1} on the **line-of-sight** velocities of both clusters. The precision on the mean cluster proper motion is limited by systematics, on the level of 11 μas yr^{-1} on each component of the mean cluster proper motion. All sampled orbits correspond to prograde, bound trajectories. The maximum altitude above the Galactic plane is z_{max}=1.80$^{+0.45}_{-0.09}$ for Berkeley 29, and z_{max}=1.59$^{+0.11}_{-0.09}$ for Saurer 1. They also exhibit small eccentricities e=0.03$^{+0.08}_{-0.01}$ and 0.05$^{+0.06}_{-0.05}$, respectively. Despite their large Galactocentric distance, the orbits of these clusters are typical of disc objects. We obtained very similar results with the model by **?**.

7. Discussion and conclusions

7.1. Summary of results

With the combination of photometric and astrometric data from *Gaia* EDR3, we have explored the dynamics of different elements of the MW in the Galactic anticentre. The main results of this study are:

1. There are prominent oscillations in the median rotation and vertical velocities of disc stars as a function of radius which depend on the evolutionary state of the stars (Sect. 4.1).
2. There are significant asymmetries in velocity when comparing stars above and below the standard Galactic plane for disc stars that can be as high as 5 km s^{-1} for the vertical velocities and 10 km s^{-1} for the rotation ones (Sect. 4.2).
3. At the outer disc, stars are predominantly following a bimodal distribution, with a group of stars mostly below the plane moving upwards with velocities of $\sim$ 10 km s^{-1} and rotating faster by about $\sim$ 30 km s^{-1} than another group of stars predominantly above the plane moving downwards by 2-5 km s^{-1} (Sect. 4.2).
4. The known R-V_ϕ ridges discovered with *Gaia* DR2, reach larger Galactocentric radius with EDR3 (up to 14 kpc) and there are also new ridges up to about 16-18 kpc, that is much beyond the limits reached in previous studies (Sect. 4.2).
5. Galactic rotation is detected as far as 18 kpc from the Galactic centre (although the exact distance depends on the possible biases in the estimated distances), being this a lower limit on the current thin disk size (Sects. 4.1 and 4.2).
6. The ancient disc that was heated after the merger with Gaia-Enceladus-Sausage **now** extends **out** to $\sim$ 14 kpc (Sect. 5.1).
7. The debris of the Gaia-Enceladus-Sausage is much more extended and can be detected at least beyond 17 kpc (Sect. 5.1).
8. The far anticentre shows a intricate superposition of structures in the proper motion and photometry diagrams including the leading (in the north) and trailing (in the south) Sagittarius stream, and known outer disc structures such of Monoceros and ACS in the north (Sect. 5.2).
9. There are two structures at latitudes of $-30 < b < -20$ deg approximately at 9 and 14 kpc from the Sun, tentatively related to the Monoceros in the south and an extension of TriAnd in the anticentre direction, respectively (Sect. 5.2).
10. The clusters Berkeley 29 and Saurer 1, which are among the oldest open clusters known, are found to be on disc-like orbits despite being located at around 20 kpc from the Galactic center (Sect. 6).

7.2. Discussion (I): MW disc dynamics

Possibly one of the most relevant discoveries from *Gaia* DR2 was the multiple features seen in the phase space of the main baryonic component of the Galaxy: its disc. These features are manifestations of the complexity in the MW's dynamics and history that resulted in a particular outcome among the large variety of discs observed in the Universe.

Nearby, the rotation velocities are dominated by the ridges **in the** (R, V_ϕ^*) **plane**, which here, as a result of the larger extension of the Galaxy that we probe with *Gaia* EDR3 and the smaller kinematic uncertainties, are detected to larger distances (up to 14 kpc from the Galactic centre, that is 3 kpc farther than for DR2) while two additional ridges are discovered that reach 16-18 kpc from the Galactic centre. The overlap of distinct ridges in R seems to be the cause of some oscillation seen in the rotation curve, as already suggested by **??**, although alternative explanations could be that they related to the location of the spiral arms (**??**) or that of the corotation resonance **?**.

The most prominent nearby ridge is Sirius, followed by the hat, L18, Hyades and Hercules. If indeed the Hercules, Sirius and hat ridges are signatures of the corotation, 4:1, and 2:1 Outer Lindblad Resonance of the bar (**??**), respectively, with the latter being the outermost resonance that can exist, the new ridges beyond 12 kpc discovered here require a different explanation. While another non-axisymmetry (but unknown so far) with a lower pattern speed could explain them, it seems more likely that they are associated to another type of perturbation and/or a phase mixing event, either caused by spiral structure or by a perturbation from Sagittarius (or the two at the same time since perturba-

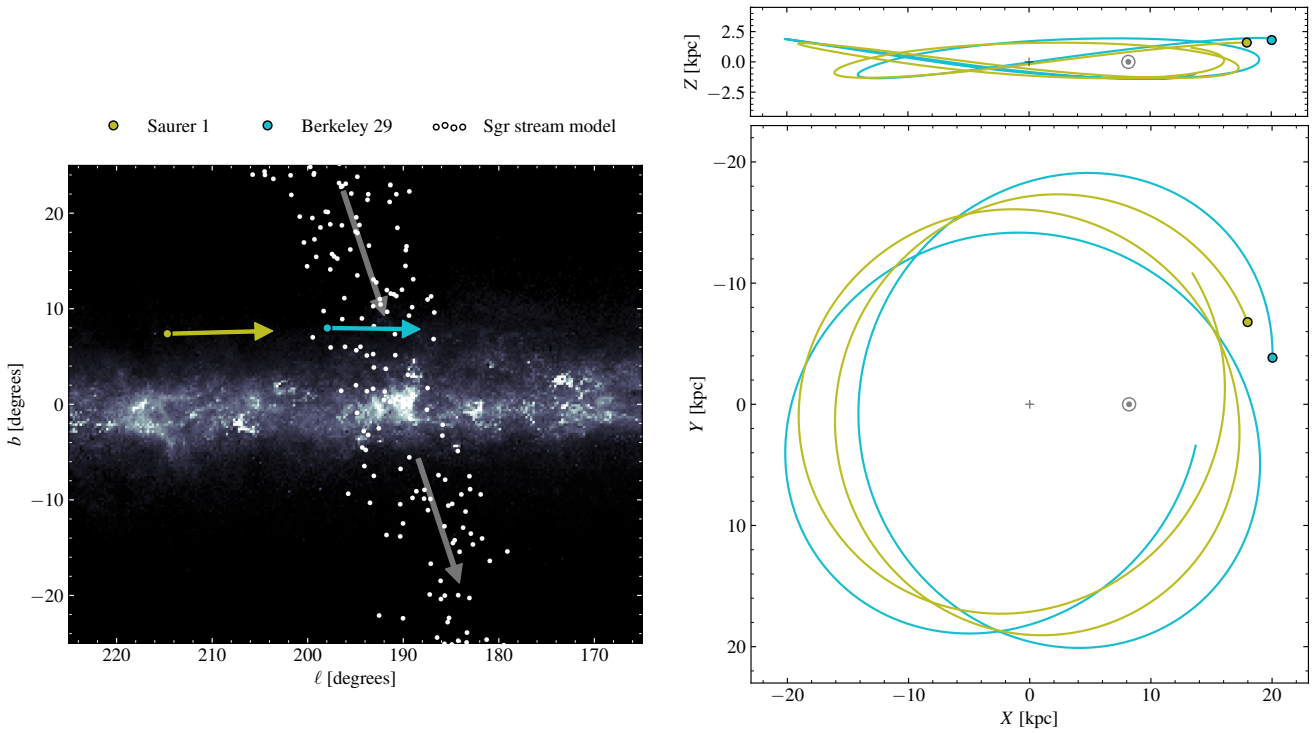

Fig. 23. Orbits if the Berkeley 29 and Saurer 1 clusters from EDR3 data. Left: location of Saurer 1 and Berkeley 29 in Galactic coordinates. The white symbols are the Sagittarius stream particles modelled by **?**. The arrows indicate mean proper motions corrected for the solar motion. The background is the integrated extinction model of **?**, beyond 2 kpc. Right: integrated orbits of Saurer 1 and Berkeley 29. The Sun's position and Galactic centre are indicated as the usual Sun's symbol and cross, respectively. We find that the orbits of these clusters are very similar and typical of the disc.

tions from satellites inevitably induce density spirals and rings, **?**).

We see clear oscillations in V_Z^* with radius of an amplitude of 1-2 km s^{-1} but increasing for younger stars. As already noticed before (e.g. **?; ?**; **?**; **?**) but now seen at a higher precision with *Gaia* EDR3, these oscillations could indicate a vertical wave propagating radially and are possibly associated to oscillations in the local mid-plane itself.

In the outer disc ($R > 12$ kpc), the velocity field is dominated by an upwards motion of about 5 km s^{-1}. This pattern was already observed but only in its part closer to the Sun for instance in **?** and **?**. Also, **?**, **? and ?** associated it to the warp that in the anticentre happens to be near the line-of nodes, **?** described it in terms of a strong bending wave possibly linked to the effects of Sagittarius, and **?** related it also to an external perturbation or to a disc that never achieved an equilibrium state.

Here, however, we go one step beyond and find, coexisting in R, two stellar groups (bimodality) moving vertically in opposite directions, predominantly located below (for the stars moving upwards) and above (downwards) of the plane, and correlating with the degree of rotation of the stars (the former group rotating faster). The feature can be observed also as a vertical velocity oscillation in angular momentum space, which can thus have different phases coexisting at the same R. This bimodality shows similar phase space correlations **to those of** the phase spiral (**?**), which might well indicate that **these phenomena** are related. Each group could have a distinct origin or, alternatively, the bimodality could be interpreted as different wraps of a phase-mixing feature or a combination of bending waves.

While the interpretation appears complex, even the understanding of the feature itself is a challenge at this point, perhaps limited by our simple analysis tools that combine at most 3 coordinates of the phase space while this bimodality involves at least 4 of them (Z-V_Z^*-R-V_ϕ^*), with the additional obstacle of a complex selection function at these distant regions. Our exploration reveals that simple 2d projections of phase space often do not capture the full complexity of the disc dynamics: when the vertical velocities are explored alone as a function of radius, only the upward motion (as in previous studies) is seen and adding more coordinates is necessary to observe this bimodality. Missing data in this study such as **line-of-sight** velocities and chemistry will help in the understanding of this feature. The WEAVE Galactic Archaeology survey (**??**) has a dedicated science case in the region of the anticentre to obtain **line-of-sight** velocities in complement to *Gaia*, which will be crucial in this and many other aspects explored in this study.

We also analysed the velocity dispersions and we see that the current *Gaia* EDR3 now allows for a full characterisation of the velocity ellipsoid and the asymmetric drift as a function of age and radius. In particular, the vertical velocity dispersions do not show the expected decreasing behaviour with radius but seem to increase and present very prominent oscillations that appear connected to the oscillations in the median velocities. Their relation with the mentioned bimodality and the role of the spiral arms and the flare needs to be examined.

All the complex patterns of movement discovered here need a deeper analysis and a detailed comparison with simulations. A dynamical framework is required that no longer assumes decoupling between the vertical and horizontal movements (**?**) and is capable of linking the small scale features such as the ridges, the global streaming motions, the phase spiral and perhaps structures such as the warp and the spiral arms. In any case, **we probably**

live in a Galaxy with a highly perturbed outer disc as seen in simulations of MW-like galaxies perturbed by a Sagittarius-like galaxy (**????**) dominated by rings with high vertical velocities, qualitatively comparable to what we find here. Our results also pose the question of where the mid plane of the Galaxy is in its outskirts, if we can actually define such a concept **(see ?)** and, as already questioned before (e.g. **???**) of how regular the Millky Way disc is.

7.3. Discussion (II): MW constituents

The past and recent history of the Milly Way has resulted in distinct Galaxy constituents from the smallest (clusters, thin streams, outer disc structures) to the largest scales (disc, halo). This distinction into components, which might be an oversimplification that we, historically, insist on doing, help us at least to approach phenomena of different spatial and temporal scales (e.g. star formation processes, orbital resonances) as well as particular moments in the history of the Galaxy (a major accretion event, the interaction with a satellite). These constituents should, however, serve us to understand the global structure and evolution of our Galaxy.

After *Gaia* DR2, our understanding of what we used to call Galactic components has changed, in particular recognising that most of the (local) halo is made of debris from a single accretion event and that we here find to be extended beyond the local neighbourhood at least up to distances of 17 kpc from the Sun, towards the outskirts of the disc. This is consistent with expectations from e.g. the orbit integrations of **?**, but also emphasises the global importance of the debris and confirms its retrograde nature. On the other hand, the heated thick disc left after the merger does not extend this far, having very few stars already around 14 kpc. This ancient disc was therefore smaller and more compact than even the canonical thick disc, which can be detected up to this radius. It will be interesting to try to constrain its initial properties, particularly through comparison to simulations of mergers and subsequent disc growth.

The current thin disc has a larger size and we observe stars **on circular orbits** as far as 18 kpc from the Galactic centre, and even farther as judged from the distances to RC sources. Such an important measurement needs some more detailed analysis in the context of the adopted zero parallax point and on the biases on the distances estimates, which we have shown here can not be neglected for any distance estimation that we have tested (including Bayesian distances and the simple inversion of the parallaxes). Further discussions on the extent of the disc and the need to include other aspects such as the flare when trying to measure it can be found for example in **?**. In general, other studies (e.g. **??**) already advocate for a disc that is larger than the previously thought 12-14 kpc-sized disc (**?**, and references therein).

We note that the precise values of positions and velocities reported here might be subject to small biases due to the adopted parallax zero point, the global effect of which is a compression of the distance scale, which at the same time propagates linearly to the velocities (decreasing its absolute value). We have compared the effects of a constant parallax offset of 19 μas (the average offset of the quasars) with that of **?** - a more sophisticated prescription as a function of magnitude, colour and ecliptic latitude. We find that the latter gives a more compressed distance scale but at this point it is not straightforward to claim that one prescription could better than the other (**?**). In any case, the features observed remain qualitatively the same regardless of the zero point.

Gaia has also provided us with a window into the structures that dwell at the edge of the disc. We detect the Monoceros and the ACS above the disc plane and other structures in the south. Our southern detections are possibly related to the Monoceros south or south middle structure (e.g. **??**) and TriAnd (**?**), which have not been probed in detail at $\ell \sim 180$ deg so far due to the high extinction (e.g. **??**). If confirmed, this would be the first TriAnd detection with *Gaia* data and the first time it is observed beyond its previously known longitude limit of $\ell \sim 160$ deg. Curiously, the disc bimodality that we find here and discus above, which starts at 12 kpc and has a prominent group of stars below the plane moving upwards, coincides approximately in distance with the nearby southern outer disc density structure, though the latter is at a lower latitude. The connection between these features certainly needs some attention.

All these density structures could be the corresponding northern and southern counterparts of the vertically oscillating disc (bending wave) expected in the scenario proposed by **?** and **?**, or they could be individual rings/feather structures in the outermost parts of the disc as suggested in **?**, **?**, **?**, **?** and **?**. To conclude, we find that the *Gaia* astrometric data enable the kinematic selection of members of these features, providing a uniform sample that comprises all the stellar types, and the determination of the proper motion, therefore stimulating the studies that try to explain their formation. We note that if indeed all these structures are composed of MW stars, then their kinematics and abundances contain valuable information about the chemo-dynamical evolution of the MW disc.

Moving to even smaller constituents, the open clusters are excellent elements to trace the global structure and evolution of the disc. A real revolution of open clusters discoveries already took place using *Gaia* DR2 (e.g. **??**). Here we have looked at two particular clusters, Berkeley 29 and Saurer 1, that due to their great distances from the Galaxy centre (around 20 kpc, derived photometrically and thus not affected by the parallax offset) and their old age (3-4 Gyr) probe extreme conditions in the Galaxy. Indeed, based on data from the Second US Naval Observatory CCD Astrograph Catalog (UCAC2, **?**), **?** and **?** suggested that the orbit of Berkeley 29 reaches altitudes of 20 to 30 kpc above the Galactic plane. **?** reported that Berkeley 29 rotates significantly faster than expected from the rotation curve of the MW, whereas **?** found that the cluster is likely counter-rotating, which would indicate an extragalactic origin. On the basis of their location and **line-of-sight** velocities, **?** proposed that both Berkeley 29 and Saurer 1 were deposited onto the disc by the disruption of Sagittarius. After all this uncertainty, thanks to the better membership and astrometry of *Gaia* EDR3, we finally ascertain here that the two clusters are on disc orbits.

Yet, their distant location makes us wonder whether the disc extends to such a distance or whether these clusters were brought there by other means. This requires some in-depth investigations in the context of the inside-out formation of our Galaxy, radial migration and/or the interaction with a satellite, similarly to the mechanism expelling material from the disc creating the outer disc structures. In particular Berkeley 29 has been already associated to Monoceros in **?** and in **?**, though in the latter case advocating for a stream origin of this structure. Our data indicates that the distances and proper motion of these clusters are compatible with the ones of Monoceros. Similarly, after examining the literature (**????**), we see that their chemistry and **line-of-sight** velocity are also broadly comparable. These clusters thus can be small but relevant pieces of information on the outer disc unknowns.

7.4. Conclusion

The quality of the EDR3 *Gaia* data together with the advantage of having astrometry and photometry from the same mission have allowed us to extend the horizon for exploration towards the very end of the disc, travel to the past to explore its ancient components and detect its small constituents and phase space features with better resolution. With a simple exploration of the *Gaia* data we find new complex patterns of movement in the outskirts of the Galactic disc, we estimate the extent of the ancient MW disc, show how the anticentre is a crossroad of structures likely both of internal and external origin, and uncover the nature of the orbits of two distant clusters. The anticentre is thus proven to be an excellent testbed region in the quest of deciphering the structure and history of our Galaxy that many astrophysicists are pursuing in the *Gaia* era.

Acknowledgements. This work has made use of data from the European Space Agency (ESA) mission *Gaia* (`https://www.cosmos.esa.int/gaia`), processed by the *Gaia* Data Processing and Analysis Consortium (DPAC, `https://www.cosmos.esa.int/web/gaia/dpac/consortium`). Funding for the DPAC has been provided by national institutions, in particular the institutions participating in the *Gaia* Multilateral Agreement. This work presents results from the European Space Agency (ESA) space mission *Gaia* . *Gaia* data are being processed by the *Gaia* Data Processing and Analysis Consortium (DPAC). Funding for the DPAC is provided by national institutions, in particular the institutions participating in the *Gaia* MultiLateral Agreement (MLA). The *Gaia* mission website is `https://www.cosmos.esa.int/gaia`. The *Gaia* archive website is `https://archives.esac.esa.int/gaia`. The *Gaia* mission and data processing have financially been supported by, in alphabetical order by country: the Algerian Centre de Recherche en Astronomie, Astrophysique et Géophysique of Bouzareah Observatory; the Austrian Fonds zur Förderung der wissenschaftlichen Forschung (FWF) Hertha Firnberg Programme through grants T359, P20046, and P23737; the BELgian federal Science Policy Office (BELSPO) through various PROgramme de Développement d'Expériences scientifiques (PRODEX) grants and the Polish Academy of Sciences - Fonds Wetenschappelijk Onderzoek through grant VS.091.16N, and the Fonds de la Recherche Scientifique (FNRS); the Brazil-France exchange programmes Fundação de Amparo à Pesquisa do Estado de São Paulo (FAPESP) and Coordenação de Aperfeicoamento de Pessoal de Nível Superior (CAPES) - Comité Français d'Evaluation de la Coopération Universitaire et Scientifique avec le Brésil (COFECUB); the National Science Foundation of China (NSFC) through grants 11573054 and 11703065 and the China Scholarship Council through grant 201806040200; the Tenure Track Pilot Programme of the Croatian Science Foundation and the École Polytechnique Fédérale de Lausanne and the project TTP-2018-07-1171 'Mining the Variable Sky', with the funds of the Croatian-Swiss Research Programme; the Czech-Republic Ministry of Education, Youth, and Sports through grant LG 15010 and INTER-EXCELLENCE grant LTAUSA18093, and the Czech Space Office through ESA PECS contract 98058; the Danish Ministry of Science; the Estonian Ministry of Education and Research through grant IUT40-1; the European Commission's Sixth Framework Programme through the European Leadership in Space Astrometry (ELSA) Marie Curie Research Training Network (MRTN-CT-2006-033481), through Marie Curie project PIOF-GA-2009-255267 (Space AsteroSeismology & RR Lyrae stars, SAS-RRL), and through a Marie Curie Transfer-of-Knowledge (ToK) fellowship (MTKD-CT-2004-014188); the European Commission's Seventh Framework Programme through grant FP7-606740 (FP7-SPACE-2013-1) for the *Gaia* European Network for Improved data User Services (GENIUS) and through grant 264895 for the *Gaia* Research for European Astronomy Training (GREAT-ITN) network; the European Research Council (ERC) through grants 320360 and 647208 and through the European Union's Horizon 2020 research and innovation and excellent science programmes through Marie Skłodowska-Curie grant 745617 as well as grants 670519 (Mixing and Angular Momentum tranSport of massIvE stars – MAMSIE), 687378 (Small Bodies: Near and Far), 682115 (Using the Magellanic Clouds to Understand the Interaction of Galaxies), and 695099 (A sub-percent distance scale from binaries and Cepheids – CepBin); the European Science Foundation (ESF), in the framework of the *Gaia* Research for European Astronomy Training Research Network Programme (GREAT-ESF); the European Space Agency (ESA) in the framework of the *Gaia* project, through the Plan for European Cooperating States (PECS) programme through grants for Slovenia, through contracts C98090 and 4000106398/12/NL/KML for Hungary, and through contract 4000115263/15/NL/IB for Germany; the Academy of Finland and the Magnus Ehrnrooth Foundation; the French Centre National d'Etudes Spatiales (CNES), the Agence Nationale de la Recherche (ANR) through grant ANR-10-IDEX-0001-02 for the 'Investissements d'avenir' programme, through grant ANR-15-CE31-0007 for project 'Modelling the Milky Way in the Gaia era' (MOD4Gaia), through grant ANR-14-CE33-0014-01 for project 'The Milky Way disc formation in the Gaia era' (ARCHEOGAL), and through grant ANR-15-CE31-0012-01 for project 'Unlocking the potential of Cepheids as primary distance calibrators' (UnlockCepheids), the Centre National de la Recherche Scientifique (CNRS) and its SNO Gaia of the Institut des Sciences de l'Univers (INSU), the 'Action Fédératrice Gaia' of the Observatoire de Paris, the Région de Franche-Comté, and the Programme National de Gravitation, Références, Astronomie, et Métrologie (GRAM) of CNRS/INSU with the Institut National Polytechnique (INP) and the Institut National de Physique nucléaire et de Physique des Particules (IN2P3) co-funded by CNES; the German Aerospace Agency (Deutsches Zentrum für Luft- und Raumfahrt e.V., DLR) through grants 50QG0501, 50QG0601, 50QG0602, 50QG0701, 50QG0901, 50QG1001, 50QG1101, 50QG1401, 50QG1402, 50QG1403, 50QG1404, and 50QG1904 and the Centre for Information Services and High Performance Computing (ZIH) at the Technische Universität (TU) Dresden for generous allocations of computer time; the Hungarian Academy of Sciences through the Lendület Programme grants LP2014-17 and LP2018-7 and through the Premium Postdoctoral Research Programme (L. Molnár), and the Hungarian National Research, Development, and Innovation Office (NKFIH) through grant KH_18-130405; the Science Foundation Ireland (SFI) through a Royal Society - SFI University Research Fellowship (M. Fraser); the Israel Science Foundation (ISF) through grant 848/16; the Agenzia Spaziale Italiana (ASI) through contracts I/037/08/0, I/058/10/0, 2014-025-R.0, 2014-025-R.1.2015, and 2018-24-HH.0 to the Italian Istituto Nazionale di Astrofisica (INAF), contract 2014-049-R.0/1/2 to INAF for the Space Science Data Centre (SSDC, formerly known as the ASI Science Data Center, ASDC), contracts I/008/10/0, 2013/030/I.0, 2013-030-I.0.1-2015, and 2016-17-I.0 to the Aerospace Logistics Technology Engineering Company (ALTEC S.p.A.), INAF, and the Italian Ministry of Education, University, and Research (Ministero dell'Istruzione, dell'Università e della Ricerca) through the Premiale project 'MIning The Cosmos Big Data and Innovative Italian Technology for Frontier Astrophysics and Cosmology' (MITiC); the Netherlands Organisation for Scientific Research (NWO) through grant NWO-M-614.061.414, through a VICI grant (A. Helmi), and through a Spinoza prize (A. Helmi), and the Netherlands Research School for Astronomy (NOVA); the Polish National Science Centre through HARMONIA grant 2018/06/M/ST9/00311, DAINA grant 2017/27/L/ST9/03221, and PRELUDIUM grant 2017/25/N/ST9/01253, and the Ministry of Science and Higher Education (MNiSW) through grant DIR/WK/2018/12; the Portugese Fundação para a Ciência e a Tecnologia (FCT) through grants SFRH/BPD/74697/2010 and SFRH/BD/128840/2017 and the Strategic Programme UID/FIS/00099/2019 for CENTRA; the Slovenian Research Agency through grant P1-0188; the Spanish Ministry of Economy (MINECO/FEDER, UE) through grants ESP2016-80079-C2-1-R, ESP2016-80079-C2-2-R, RTI2018-095076-B-C21, RTI2018-095076-B-C22, BES-2016-078499, and BES-2017-083126 and the Juan de la Cierva formación 2015 grant FJCI-2015-2671, the Spanish Ministry of Education, Culture, and Sports through grant FPU16/03827, the Spanish Ministry of Science and Innovation (MICINN) through grant AYA2017-89841P for project 'Estudio de las propiedades de los fósiles estelares en el entorno del Grupo Local' and through grant TIN2015-65316-P for project 'Computación de Altas Prestaciones VII', the Severo Ochoa Centre of Excellence Programme of the Spanish Government through grant SEV2015-0493, the Institute of Cosmos Sciences University of Barcelona (ICCUB, Unidad de Excelencia 'María de Maeztu') through grants MDM-2014-0369 and CEX2019-000918-M, the University of Barcelona's official doctoral programme for the development of an R+D+i project through an Ajuts de Personal Investigador en Formació (APIF) grant, the Spanish Virtual Observatory through project AyA2017-84089, the Galician Regional Government, Xunta de Galicia, through grants ED431B-2018/42 and ED481A-2019/155, support received from the Centro de Investigación en Tecnologías de la Información y las Comunicaciones (CITIC) funded by the Xunta de Galicia, the Xunta de Galicia and the Centros Singulares de Investigación de Galicia for the period 2016-2019 through CITIC, the European Union through the European Regional Development Fund (ERDF) / Fondo Europeo de Desenvolvemento Rexional (FEDER) for the Galicia 2014-2020 Programme through grant ED431G-2019/01, the Red Española de Supercomputación (RES) computer resources at MareNostrum, the Barcelona Supercomputing Centre - Centro Nacional de Supercomputación (BSC-CNS) through activities AECT-2016-1-0006, AECT-2016-2-0013, AECT-2016-3-0011, and AECT-2017-1-0020, the Departament d'Innovació, Universitats i Empresa de la Generalitat de Catalunya through grant 2014-SGR-1051 for project 'Models de Programació i Entorns d'Execució Parallels' (MPEXPAR), and Ramon y Cajal Fellowship RYC2018-025968-I; the Swedish National Space Agency (SNSA/Rymdstyrelsen); the Swiss State Secretariat for Education, Research, and Innovation through the ESA PRODEX programme, the Mesures d'Accompagnement, the Swiss Activités Nationales Complémentaires, and the Swiss National Science Foundation; the United Kingdom Particle Physics and Astronomy Research Council (PPARC), the United Kingdom Science and Technology Facilities Council (STFC), and the United Kingdom Space Agency (UKSA) through the following grants to the University of Bristol, the University of Cambridge, the University of Edinburgh, the Uni-

versity of Leicester, the Mullard Space Sciences Laboratory of University College London, and the United Kingdom Rutherford Appleton Laboratory (RAL): PP/D006511/1, PP/D006546/1, PP/D006570/1, ST/I000852/1, ST/J005045/1, ST/K00056X/1, ST/K000209/1, ST/K000756/1, ST/L006561/1, ST/N000595/1, ST/N000641/1, ST/N000978/1, ST/N001117/1, ST/S000089/1, ST/S000976/1, ST/S001123/1, ST/S001948/1, ST/S002103/1, and ST/V000969/1.

Appendix A: Queries to the *Gaia* Archive

In this Appendix we show a few examples of queries to the *Gaia* Archive `https://gea.esac.esa.int/archive/` to retrieve the data:

Listing 1. An example of query to retrieve stars in the rectangular sky patch of the AC20 sample.

```
SELECT * from gaiaedr3.gaia_source WHERE l<190 and
    l>170 and b>-10 and b<10 }
```

Listing 2. An example of query to retrieve the number of stars and average quantities in all healpix of level 8 inside a rectangular patch in the sky.

```
SELECT sub.healpix_8,COUNT(*) as
    N,AVG(phot_g_mean_mag) as avg_g,
    AVG(visibility_periods_used) as avg_vp FROM
    (SELECT gaia_healpix_index(8, source_id) AS
    healpix_8,phot_g_mean_mag,visibility_periods_used
    FROM user_edr3int4.gaia_source WHERE l<240 AND
    l>120 AND b<60 and b>-60 AND ruwe < 1.4) AS sub
    GROUP BY sub.healpix_8
```

Appendix B: Selection of Red Clump stars

In this Appendix we describe the selection of the RC subsample.

First, in order to compute the absolute magnitude, we need good estimates of the extinction A_λ in band λ. For each star, one could in principle use the 2D (l, b) maps of reddening, $E(B-V)$, from **?** which estimates the extinction at infinity. However, these 2D extinction values will overestimate the reddening. Since, we have parallax information for our sample, we can use this as a prior for distance and estimate the 3D extinction. For this, we make use of the 3D dust-reddening maps from *Bayestar* (**?**). These are derived using a Bayesian scheme that combines *Gaia* parallaxes with photometry from the *2MASS* and *Pan-STARRS* surveys, and covers the sky North of declination of $-30°$. Only 3 stars in our AC20 sample are missing from *Bayestar*. The multiplicative factor (f_λ) between reddening and extinction that we use is listed in Table B.1 for various bands.

For the RC selection, we first apply the following photometric cuts:

$$BP - G > 0.6, BP - RP_0 > 0.91. \tag{B.1}$$

Then, for each star, we compute the absolute magnitude (M_λ) in each of the *2MASS* bands, and in Gaia G:

$$M_\lambda = m_\lambda - A_\lambda - \mathrm{dmod}, \tag{B.2}$$

using $\mathrm{dmod} = 5\ log_{10}(100/\varpi'[\mathrm{mas}])$. Here, ϖ' is the parallax corrected for the offset of 17 μas. In Table B.1 we list the literature absolute magnitude $(\bar{M}_\lambda)$ and dispersion in various photometric bands for the RC population. Using this, for each star we can write down a likelihood function per bandpass i, and take their product

$$P_{RC}(m_\lambda, A_\lambda, \varpi) = \prod_i \sqrt{2\pi}\sigma_{\bar{M}_\lambda} \mathcal{N}(M_\lambda || \bar{M}_\lambda, \sigma^*_{M_\lambda}), \tag{B.3}$$

where $\sigma^*_{M_\lambda} = \sqrt{\sigma^2_{er,M_\lambda} + \sigma^2_{\bar{M}_\lambda}}$ combines the propagated error in the absolute magnitude from Equation B.2, σ_{er,M_λ}, and the dispersion in the true absolute magnitude, $\sigma_{\bar{M}_\lambda}$.

Table B.1. Median absolute magnitude $\bar{M}_\lambda$, and dispersion in absolute magnitude $\sigma_{\bar{M}_\lambda}$ for RC stars selected from **?**. Also listed are the extinction factors (f_λ) for the four passbands used, with the *2MASS* values taken from **?** and *Gaia* from **?**.

Passband (λ)	$\bar{M}_\lambda$	$\sigma_{\bar{M}_\lambda}$	$f_\lambda = \frac{A_\lambda}{E(B-V)}$
J	-0.93 ± 0.01	0.20 ± 0.02	0.7927
H	-1.46 ± 0.01	0.17 ± 0.02	0.469
K	-1.61 ± 0.01	0.17 ± 0.02	0.3026
G	$+0.44 \pm 0.01$	0.20 ± 0.02	2.74
G_{BP}	-	-	3.374
G_{RP}	-	-	2.035

Table B.2. Parameters used for selecting the *RC* population. *ML* is essentially the confidence level used to set a minimum probability threshold (P_{RC} >). Finally, N_{RC} gives the resulting number of stars classed as RC that lie between $170° < l < 190°$ and $|b| < 10°$.

ML	N_{RC}	P_{RC} >	band(s)
3	**121857**	0.01	*2MASS J*, *Gaia G*

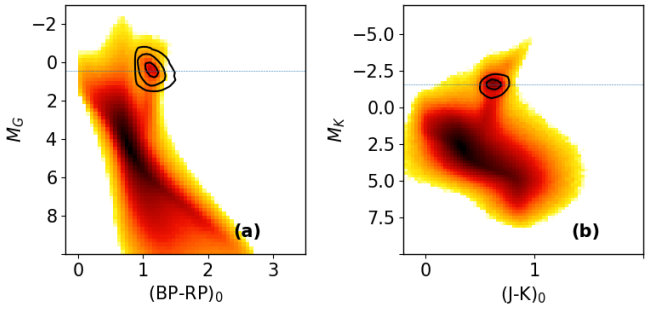

Fig. B.1. HR diagrams for the AC20 sample, with contours marking the RC selection.

For any distribution, the distance between the centroid (x_0) and a point of interest (x_1) can be given in terms of its Mahalanobis distance (ML)

$$ML^2 = (x_1 - x_0)^T \Sigma^{-1} (x_1 - x_0), \tag{B.4}$$

that respects the combined covariance of x_0 and x_1, which we have written as Σ. Essentially, ML is a measure of the distance from the centroid in units of the standard deviation. Then, we can define a p-value, i.e. the probability of finding a value of ML^2 or more extreme under the null-hypothesis of the star not being part of the RC, from a chi-square distribution, and select those stars for which

$$P_{RC} > 1 - P[\chi^2 \leq ML^2] \tag{B.5}$$

i.e., the probability (P_{RC}) is greater than the p-value. In this work we limit our analysis to a maximum of two bands, namely, *Gaia* G and *2MASS* K. So, we use a chi-square distribution with 2 degrees of freedom, and ML is essentially the confidence level used to set a minimum probability threshold. The tolerance parameters used in our selection is shown in Table B.2, and we obtain a high quality RC sample of N_{RC} =**121857**. The HR diagram with our RC selection is shown in Figure B.1. The parallax quality for the selection is shown in Figure B.2, with the tail of the distribution extending down to $\sigma_\varpi/\varpi \approx 0.8$.

In Figure C.5, we further inspect the RC selection. Panels(a-b) show the absolute magnitude distribution in G and K bands. We find that the median absolute magnitudes for our sample is

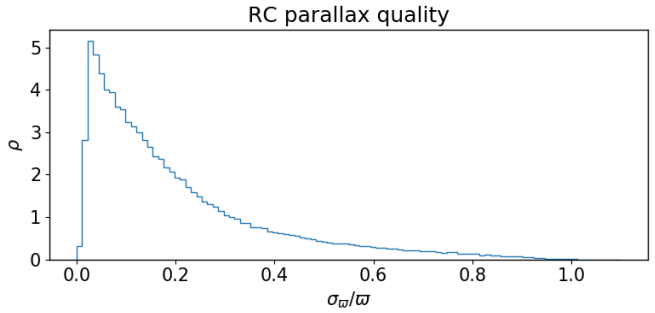

Fig. B.2. Parallax error quality of the RC sample. The tail of the distribution extends down to $\sigma_\varpi/\varpi \approx 0.8$.

offset from their literature values by -0.05 (G) and 0.05 (K) in the two bands. The yellow curves use the *Bayestar* reddening, but we also show the distribution for absolute magnitudes computed with $A_\lambda = 0$, just to illustrate that our extinction correction shifts the distribution in the correct direction. In Panels (c-d), we compare the distances computed as in **??**, against inverse parallax. It is encouraging to see that the running median for nearby stars lies on the 1:1 line. This is further shown in panels (e-f), where we look at the relative difference between the two distance estimates. Compared to inverse parallax method, our distances are slightly under (over) estimated in G (K) beyond 5 kpc from the Sun. This is likely due to the fact that distance modulus $\propto$ -M_λ. Since the literature absolute magnitudes are slightly offset, this would result in smaller distances, but the effect is minor given the small offset, especially in the K band. Finally, in panels (g-h), is shown the distance error as a function of distance. The errors in the inverse parallax distances are quadratic with d, while the trend is linear for the Red Clump distances. Beyond, $d > 5$ kpc, the errors in inverse parallax grow significantly, while for RC distances, the prediction is σ_d 1.5 kpc at 10 kpc. The distribution in heliocentric distance and Galactocentric cylindrical radius R is shown in Figure C.7. Our sample extends out to $R \sim$17 kpc, consisting of about 1000 stars at that distance.

? recently put out a catalogue of 2.6 million RC stars. Their method involves predicting asteroseismic parameters ($\Delta P, \Delta\nu$) and stellar parameters ($\log g$,$T_{\rm eff}$) from spectral energy distributions (SED). They combined photometry from *Pan-STARRS*, *WISE*, *2MASS* and *Gaia*. In their catalogue (hereafter L20) they classified RC stars with contamination rate of $\approx$ 33% as 'Tier II', and a superior subset with contamination rate of $\approx$ 20% as 'Tier I'. In Figure B.3 we show the distribution of our sample on a *Kiel* diagram by cross-matching with the L20 catalogue. We notice that their 'Tier I' sample does not have too many cooler stars. Conversely, their less stringent 'Tier II' sample, extends out to $\log g \approx$ 1.8, which is typically the lower limit of the RC range, and thus prone to contamination from regular giants.

Finally, we use *APOGEE*-DR16 (**?**), to construct the background *Kiel* diagram. This shows that our RC sample is largely concentrated around the horizontal branch (blue contour), thus missing several common stars with L20, but at the same time is likely a 'purer' sample for the purpose of distance estimation.

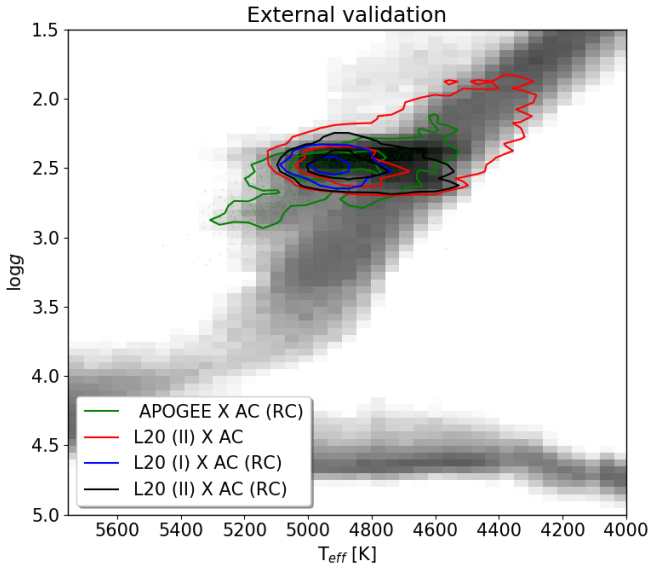

Fig. B.3. External validation comparing the distribution of the AC20 RC stars on a *Kiel* diagram. In grey is the full distribution from *APOGEE*-DR16, and the green contours show common stars between our RC sample and *APOGEE*-DR16. Red contours show common stars between L20 and the entire anticenter sample used here. The blue contours show common stars between L20-'Tier I' (i.e., 20% contamination) and our RC sample. The black contours show common stars between L20-'Tier II' (i.e., 33% contamination) and our RC sample.

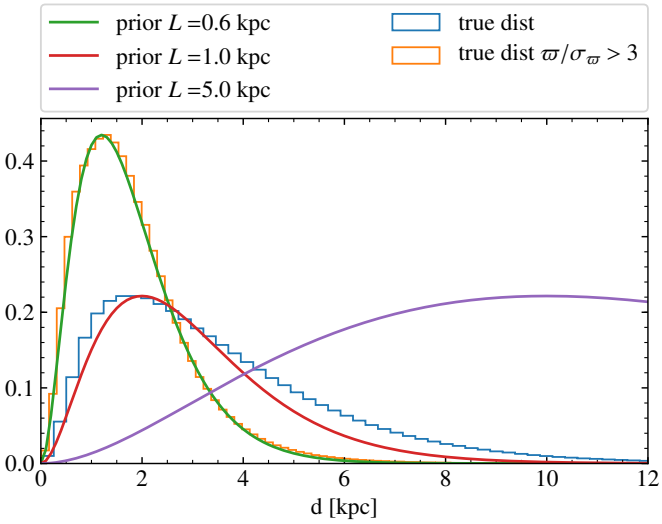

Fig. C.1. Distribution of true distances of GOG in the anticenter. We show all stars in GOG (blue histogram) and stars with $\varpi/\sigma_\varpi > 3$ (orange histogram). The different solid lines are the exponential decreasing prior (Eq. (C.1)) with scalelenght of 0.6, 1 and 5 kpc.

Appendix C: Distances to stars

Appendix C.1: Distance estimates

As discussed in Sect. 3.2 there is no existing perfect recipe for estimating distances from a measured parallax. In this work we approach this problem by testing how robust our conclusions are to the use of different distance estimators. We use three different methods, which we test with the mock *Gaia* data from GOG (described in Sect. 2.2):

1. d_ϖ: simple inversion of parallax $1/\varpi$

2. $d_{\rm PM}$: Bayesian distances with an iterative prior This approach is closely related to that used by **?**. In general, the

Bayesian approach relies on the statement that for an observed parallax, ϖ, and uncertainty, σ_ϖ, the probability of a given distance d is

$$P(d) \propto P(\varpi|d, \sigma_\varpi)\, P(d)$$

where $P(d)$ is the prior on distance. This prior takes three factors into account:

- The volume at distances between d and $d + \delta d$ increases like d^2.
- The true spatial distribution of stars is not uniform.
- Selection effects: the probability of a star at distance d entering the catalogue varies with d because there is a magnitude limit to the survey (because e.g., intrinsically faint stars become too faint to enter the catalogue).

For the distances $d_{\rm PM}$, these considerations lead us to a prior $P(d) \propto d^2 P(\mathbf{r}(d))S(d)$, where $S(d)$ is the selection function, and $\mathbf{r}(d)$ is the position in a galaxy of an object at distance d along a given line-of-sight, so $P(\mathbf{r}(d))$ is proportional to the density of a model Galaxy. The distance estimate, $\tilde{d}$ and uncertainty σ_d is then found as the expectation value and standard deviation of d given this prior and the measured parallax (with uncertainty).

The model from which we take $P(\mathbf{r}(d))$ is taken from **?**, and has two exponential discs (thin and thick) and a power-law halo. It has no warp. We approximate the selection function as $S(d) \propto \exp(-d/L_s)$ where L_s is a value we determine. Experiments with GOG (see below) and investigation with the *Gaia* data both suggest that this is a reasonable approximation.

Following **?**, we derive the selection function from the data itself by recognising that $S(d) \propto N(d)/(d^2 \int \rho(d, l, b) \cos b \mathrm{d}l\, \mathrm{d}b)$ where $N(d)$ is the number of stars in the catalogue at a distance d and the integral over ℓ, b is taken over the field we consider. We don't know $N(d)$, but we can make the approximation that $N(d) \approx N(\tilde{d})$ for some range of distances and subset of the more accurate parallaxes. We use this to find the scale length L_s which enters into $S(d)$. We then iterate this process – using this estimate of the selection function to find new distance estimates, $\tilde{d}$, then using these to make a new estimate of $S(d)$. Experiments with GOG indicate that fitting $S(d)$ for distances $1 < d/\mathrm{kpc} < 3$ and for stars with $\varpi/\sigma_\varpi > 3$ give a reasonable approximation. The value of L_s we find converges after a few iterations and we find $L_s = 0.963$ for our sample and $L_s = 1.16$ for GOG.

3. d_L: Bayesian distances with exponentially decreasing prior with scale length of L following **?** These distances are computed following **?** with a simpler prior, in particular an exponentially decreasing prior with distance d:

$$P(d|L) = \begin{cases} \dfrac{1}{2L^3}\, d^2 e^{-d/L} & \text{if } d > 0 \\ 0 & \text{otherwise} \end{cases} \tag{C.1}$$

Figure C.1 shows the true distribution of distances of GOG (blue histogram) and the same for a selection of sources with $\varpi/\sigma_\varpi > 3$ (orange histogram). As explained in **?**, a good approximation for the maximum likelihood estimate for the scale-length L of the prior Eq. (C.1) of a given distance distribution is $MED(d)/3$, where $MED(d)$ is the median of the distribution. For GOG in the anticenter this turns out to be 0.977 kpc and 0.527 kpc for stars with $\varpi/\sigma_\varpi > 3$. The red and green solid lines show the shape of the prior with $L = 1$ kpc and $L = 0.6$ kpc, respectively, which fairly reproduce the true distribution of distances in each case. We also show the prior for $L = 5$ kpc. Hereafter, we choose two different scale-length L of 1 kpc (that we name d_{L_1}) and 5 kpc (d_{L_5}), motivated by the tests shown below. While **?** uses a scale-length that depends on the sky coordinates, here for simplicity we use a single value for the whole field of 20×20 deg.

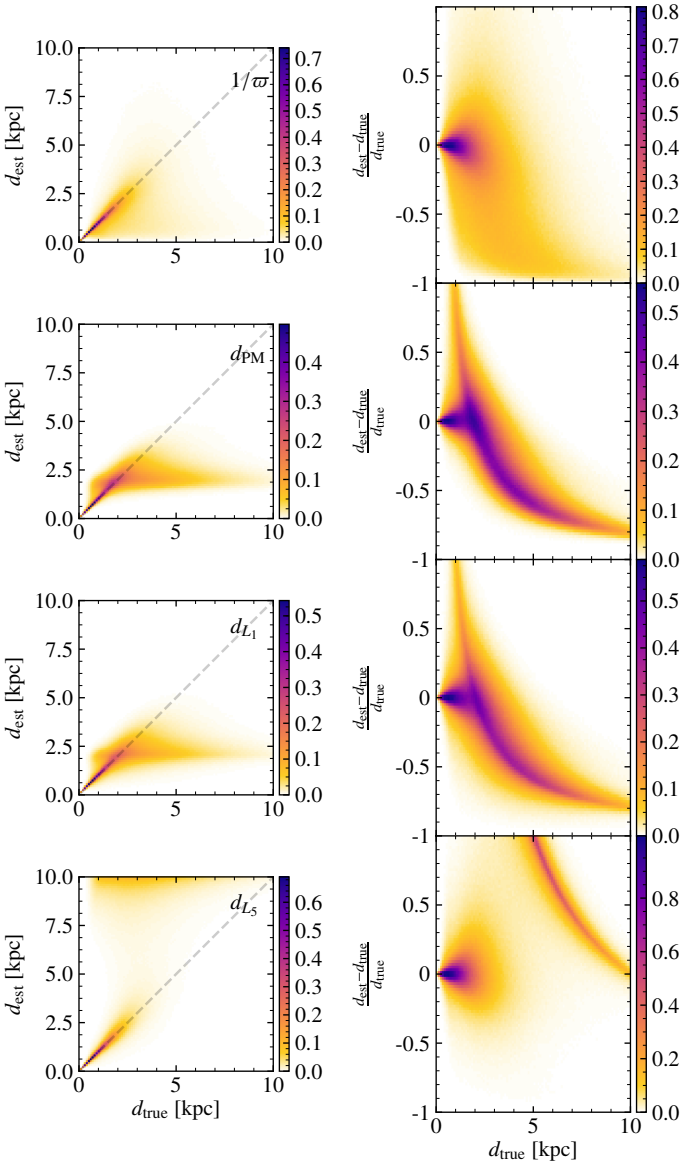

Fig. C.2. True versus estimated distances for different methods. *Left:* Direct comparison between true and estimated distances of GOG for the different distance estimations as indicated in the legends. *Right:* Fractional error in the estimated distance as a function of true distance for the same estimators.

Appendix C.2: Tests with GOG

Here we test the different distances estimations with GOG. First we note that due to deficiencies in the *Gaia* error model, the uncertainties in the astrometric values in GOG somewhat disagree with the values for EDR3. In particular we see an overestimation of the parallax errors as a function of magnitude G, actually more similar to the DR2 scenario than to EDR3 (Fig. E.1 top). The exercises presented here will thus show a worse case scenario.

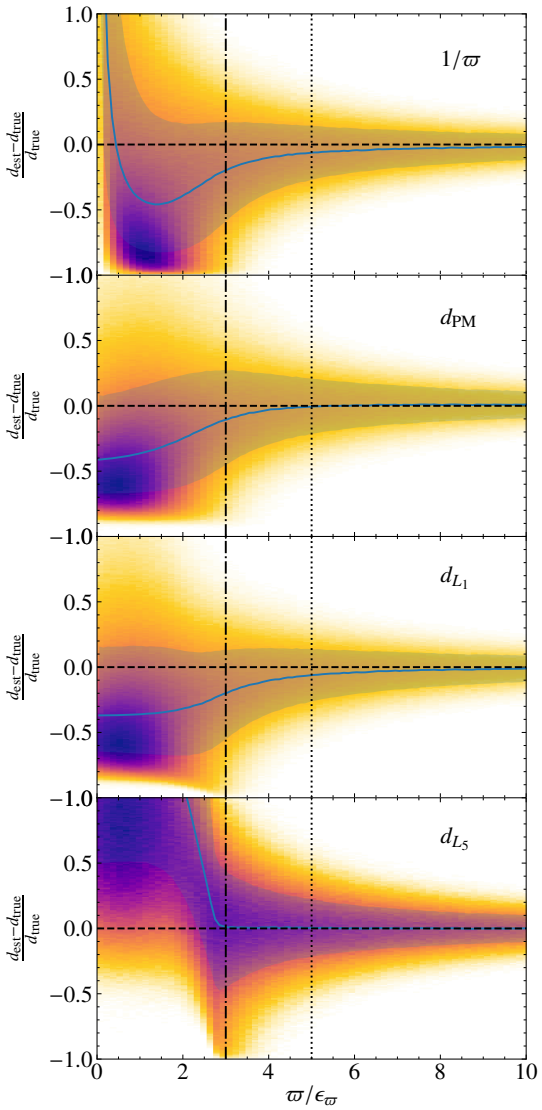

Fig. C.3. Fractional error in the estimated distance as a function of fractional error in parallax. We show the errors for the different distance estimations as indicated in the labels for the GOG sample. Solid lines indicate the median fractional error and shaded areas show the 25 and 75% quartiles.

Figure C.2 shows the comparison between true distance and estimated distance for the different methods presented above applied to the whole GOG sample, for which the true distances are known. We see in the left panels a good fraction of stars with properly determined distances falling on the 1:1 line (those with small parallax uncertainties). However, we also see large fraction of stars with badly estimated distances corresponding to parallaxes with large uncertainty (including negative parallaxes). For the d_ϖ case (top panels), most of these problematic cases appear scattered in the underestimated region. For Bayesian estimations d_{PM}, d_{L_1} and d_{L_5} (three bottom panels), they appear concentrated at the nearly horizontal line at $d_{\rm est} = 2L$ (coinciding with two times the mode of the prior, that is $\sim$ 2 kpc in the two middle rows, and 10 kpc for the bottom row), completely dominated by the choice of the prior as explained in **?**. These numerous uninformative parallaxes forces us to perform a cut in fractional parallax uncertainty, which, unfortunately, may introduce biases in our samples as discussed for instance in **?**.

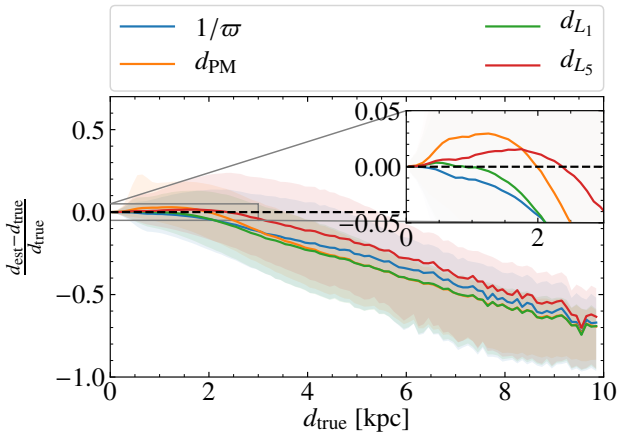

Fig. C.4. Median fractional error in the estimated distance for good quality parallaxes. We show the errors as a function of true distance for different distance estimations as indicated in the labels for stars with $\varpi/\sigma_\varpi > 3$ in the GOG sample. Solid lines indicate the median fractional error and shaded areas show the 25 and 75% quartiles.

Figure C.3 shows the fractional error in the estimated distance as a function of fractional error in parallax with different panels for different distance estimations. All panels show large errors for large parallax uncertainties (smaller ϖ/σ_ϖ) as expected and highlight the need to use a certain criteria to select good parallaxes while finding a proper balance with the final number of sources kept and trying not to bias the sample as a result of eliminating specific populations. Depending on the particular analysis, these considerations might lead to different choices. Here we choose to select sources with $\varpi/\sigma_\varpi > 3$ in the case of the AC20 sample (dash-dotted vertical line) while a more restrictive cut at $\varpi/\sigma_\varpi > 5$ is used for ACH (dotted line).

From Fig. C.3 we also note two important aspects. First, the performance of the 4 different methods is quite similar when one chooses cuts in ϖ/σ_ϖ as the ones mentioned above, with only a slight underestimation of the distances in the case of d_ϖ compared for instance to d_{PM}. Second, we also want to emphasise that, even if the median differences between estimated and true distances are small, at $\varpi/\sigma_\varpi > 5$ (dotted vertical line) 50% of the sources have errors in the derived distances $\gtrsim$ 20% (sources outside the shaded areas which enclose the other 50%) independently of the method used.

Now focusing on the selection of sources with $\varpi/\sigma_\varpi > 3$, the distance error of these different estimators as a function of true distances is shown in Fig. C.4. We see a slightly better performance of the d_{L_5} at larger distances but a better one for d_{L_1} at nearby distances. The d_ϖ is underestimated in median for all distances while d_{PM} shows overestimated distances at nearby distances, but the contrary beyond 2 kpc. Apart from these little differences, we note that non of the estimators is completely free of bias even with the selection of $\varpi/\sigma_\varpi > 3$, as already mentioned above. We see underestimations of the distance that start to be important (20%) at around 4 kpc and biases larger than ~40% for 25% of the sources at this same distance. Again we emphasise that the parallax errors in GOG are overestimated with respect to *Gaia* EDR3, and therefore the expected biases as a function of distance in EDR3 are possibly smaller than shown here.

All these tests show that different priors might work better in different regimes and that there can be multiple criteria to choose which method provides a better estimate (e.g. minimis-

ing the median distance error at small versus large distances). We also need to keep in mind that these conclusions are somewhat model dependent, influenced by the particular Milky Way density model and selection function imposed in GOG. Our approach of exploring varied distances estimations wants to mitigate this model-dependency and the appropriateness of different methods and priors in different cases. We highlight that it is necessary to evaluate the impact of this biases and the effects of the parallax quality cut on the different analysis.

So far what we have shown regarded only the estimation of the distance. This estimation and a single value for its uncertainty is then used, together with the proper motions, to calculate velocities and their uncertainties. However, we know this is not strictly correct. On one hand, because the proper motion errors are correlated with the parallax errors and, on the other, because the distribution of uncertainties in the estimated distance in general is not Gaussian and asymmetric. Ideally, then, one would use a method to estimate simultaneously the distance and the tangential velocity of each star. The *Gaia* technical note GAIA-C8-TN-MPIA-CBJ-081 described a way to infer velocities and distances at the same time, from the proper motions and parallax, using a MCMC method. This approach is mathematically more accurate and allows us to deal properly with the correlations between velocities and distances. We have tested it with a random subset of the GOG sample and conclude that: i) the resulting velocities are similar to the ones obtained with the usual and simpler approach, ii) the correlation between velocities and distances is dominated by the transformation rather than by the correlation in the uncertainties, iii) a cut in parallax quality is still necessary and iv) the high computation cost renders it unfeasible to use for even modest-sized samples. For all these reasons, we do not use it here.

Appendix C.2.1: Red Clump distances

For each star classified as RC, we can invert Equation B.2 to calculate the distance modulus. For this we use the literature absolute magnitudes in each band pass, $\bar{M}_\lambda$. The errors in the computed distances using the RC and parallax only is given by,

$$\sigma_{d_{RC,\lambda}} = 0.2ln(10)\sigma_{M_\lambda} d \quad (C.2)$$

$$\sigma_{d_\varpi} = \sigma_\varpi d^2, \quad (C.3)$$

where σ_{M_λ} is the dispersion in the computed absolute magnitudes of the RC selection, and σ_ϖ is the parallax error. The parameters in Table B.2 are fine tuned in order to maximise the number of RC stars and minimise the dispersion and thus the errors in distances.

As mentioned earlier, we do not apply the 'qfl' quality flag on *2MASS* photometry, but instead use the photometric errors to decide if the distances will be estimated using the K band or G band. In general, the K band suffers from lower extinction than the broader G band, so we prefer to use distances estimated using K. However, if for a given star the photometric errors, (e_jmag| e_kmag) > 0.025, the typical value above which photometry in *2MASS* becomes unreliable, then we estimate distances for these using the G band. This is illustrated in Figure C.6, where we compare our distance estimates to the external catalogue of L20. Essentially, for stars with poor *2MASS* photometry we overestimate the distances if the k band is used. Replacing these with G band estimates results in a much better agreement with the external catalogue.

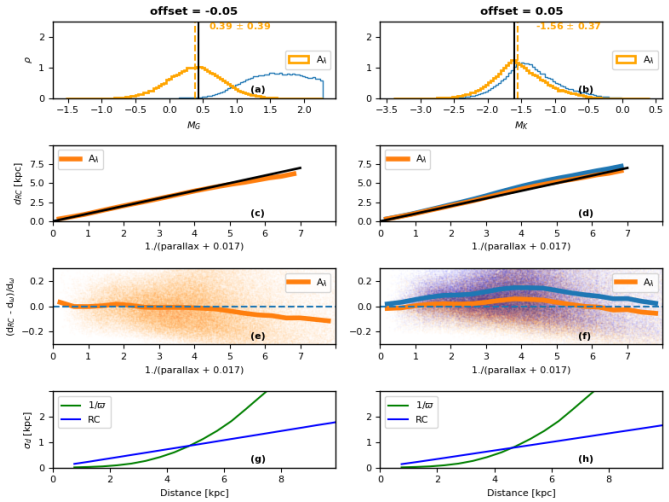

Fig. C.5. Red clump sample inspection. (a-b) Absolute magnitudes in G and K for the selected sample. The yellow curves use the 3D extinctions from *Bayestar*, while the blue curves are for zero extinction shown just for illustration of shift towards the correct literature value upon reddening correction. (c-f) compare the RC distances to inverse parallax, while panels (g-h) show the error in distances as a function of d for the two methods. Beyond 5 kpc, RC distances become more reliable than inverse parallax.

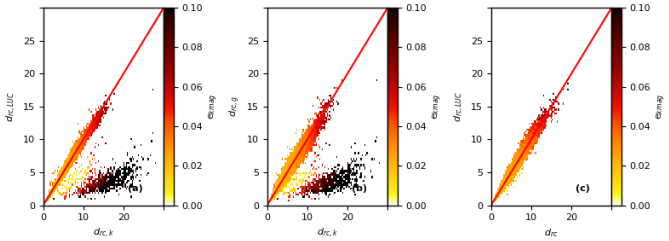

Fig. C.6. Red Clump distance validation with the external catalogue L20. To enhance the illustration we use a larger RC sample here (147° < l < 219° and $|b|$ < 30°). Panel a) Comparison to L20 shows the presence of a population for which distances are overestimated using the K band. This is due to very high photometric errors i.e., (e_jmag| e_kmag) > 0.025. b) Comparison between G and K band derived distances also highlights the same trend, i.e., K band distances are overestimated for poor photometry stars. c) Replacing K band estimates with G where (e_jmag| e_kmag) > 0.025 improves agreement with L20.

Appendix C.2.2: Comparison of the different distances for EDR3

Finally, Fig. C.8 compares all sets of distances derived in this work using the d_{PM} case as a baseline (see caption for more details).

Appendix D: Parallax zero point

In this Appendix we illustrate the differences in distance and velocities when different parallax zero points are used (Fig. D.1), and we reproduce several figures of the main part done with and without different parallax zero points (Figs. D.2 and Fig. D.3).

Appendix E: Additional material

In this Appendix we present a miscellanies set of plots that serve as supporting material to the rest of the sections. A describing text can be found in each of the figures.

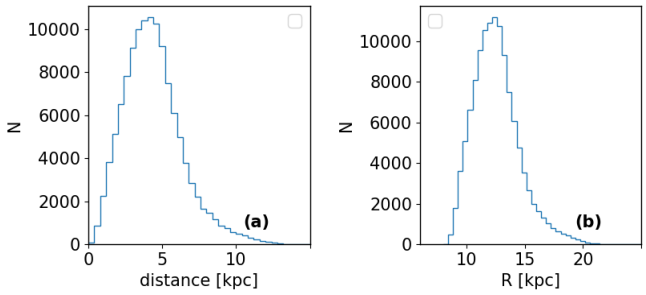

Fig. C.7. Number of RC stars as a function of a) heliocentric distance, and b) Galactocentric distance (R).

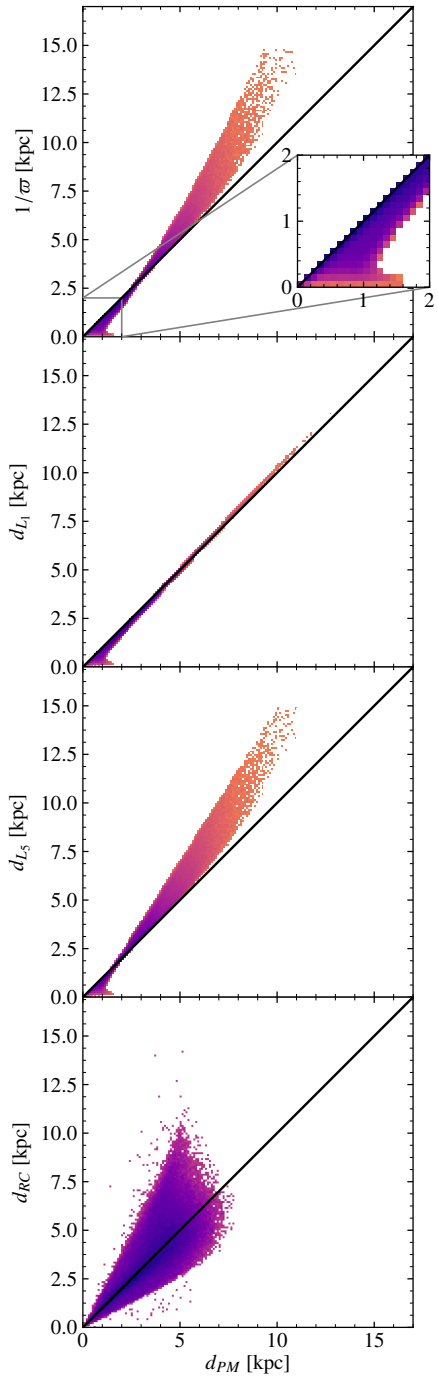

Fig. C.8. Comparison of the different distances used in this study. The comparison is done with respect to the d_{PM} distances. The discrepancies are small for small distances. For the case of the RC, we only compare stars with $\varpi/\sigma_\varpi > 3$, since the rest of RC sources are not included in our set of d_{PM}. This is then misleading since for these stars the parallax retrieves better distances, but the real gain for the RC occurs exactly for the stars missing in this panel, in the regime where the photometric distances might be better than the ones from parallax alone. The peculiar shape shown in the inset of the top panel and present in the three top panels is composed of stars with large parallax error, for which the expectation values used in the d_{PM} estimation are larger than for instance the medians used in d_L.

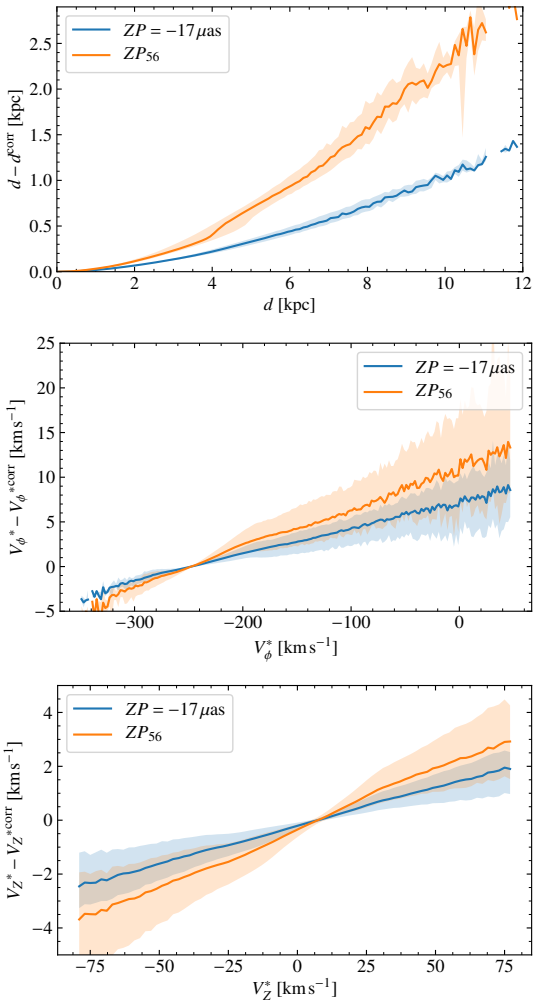

Fig. D.1. Effects of the zero point in parallax on distances and velocities. The comparison is done with respect to the case where the zero point is not considered (x axis) and the shaded areas show the percentiles 10 and 90 (i.e. they enclose 80% of stars). In the top panel, we see how not correcting for the zero point produces overestimated distances. The zero point prescription ZP_{56} reduces even more the distances compared to the case of a fixed zero point $ZP = 19\,\mu$as. The velocities (middle and bottom) scale linearly with the distance and thus we see the absolute magnitude of the velocities being larger when the zero point is not considered. We see null differences in the case of null proper motion, that is when the velocities equal that of the Local Standard of Rest.

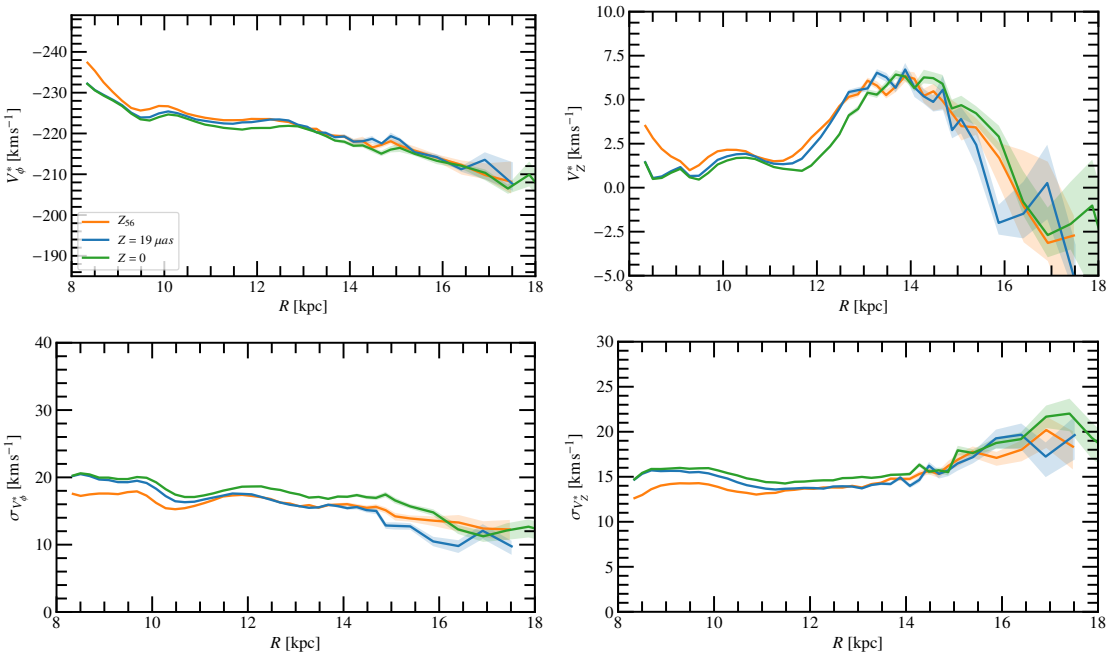

Fig. D.2. Velocity profiles for different parallax zero points. In the rotation curve (top left), as expected, the rotation curve computed using ZP_{56} (orange curve) is slightly shifted to the left (R decreases by about 0.5 kpc at $R = 14$ kpc) and V^*_ϕ also decreases, but always in amounts smaller than $\sim 2\,\mathrm{km\,s^{-1}}$. In the vertical velocity plot (top right), we observe similar effects, though a notable effect is seen in the first kpc. The velocity dispersions (bottom) appear also lightly different, with ZP_{56} yielding smaller dispersions but without changing the overall shape.

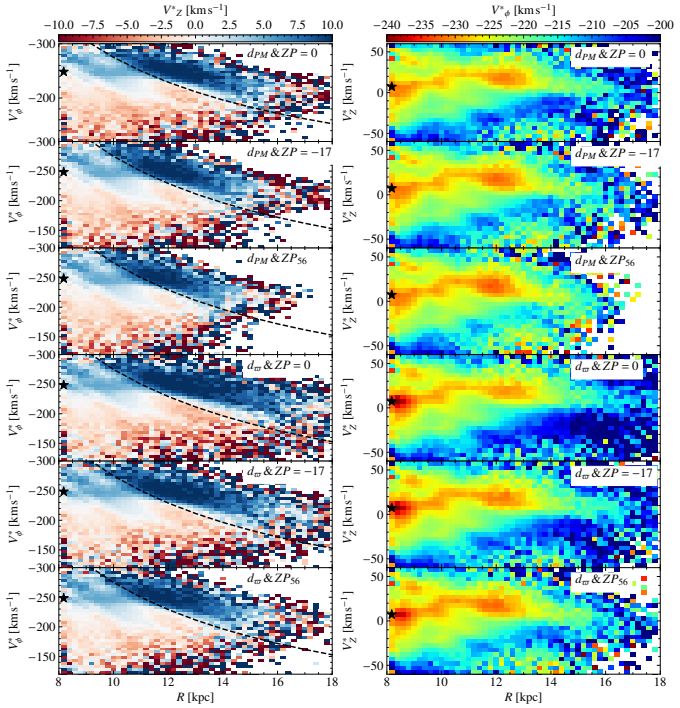

Fig. D.3. Phase space projections for different parallax zero point. The plot reproduces panels b and e of Fig. 13 using different distance estimations and parallax zero point as indicated in the legends. As explained in other parts of the article, the correction of the zero point combined with the different distance estimators used produce a change in the distance scale but in any case induces or removes the phase space substructure such as the one observed in this panels. The smallest distances are found when the Bayesian distances d_{PM} and the zero point ZP_{56} are used.

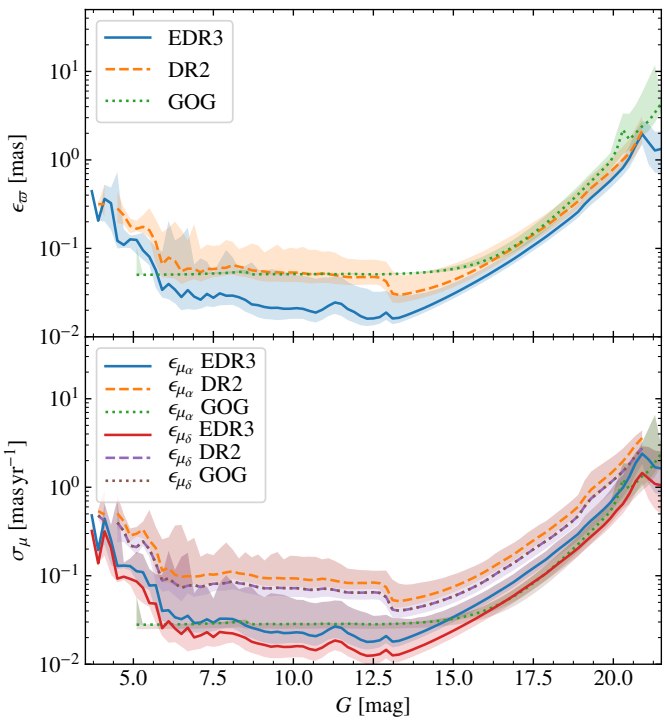

Fig. E.1. Comparison of the astrometric uncertainties for DR2, EDR3 and GOG. Due to deficiencies in the GOG *Gaia* error model, the astrometric uncertainties in GOG do not match perfectly those for EDR3. The error model retrieves unique values of the formal uncertainties as a function of G, while a large range is obtained for the data (shaded areas showing the 10% and 90% percentiles). We also see an overestimation of the parallax errors (top), which actually look more similar to the DR2 scenario than to EDR3. The errors of the proper motions are closer to the true uncertainties although no distinction between the different components is made for this mock data.

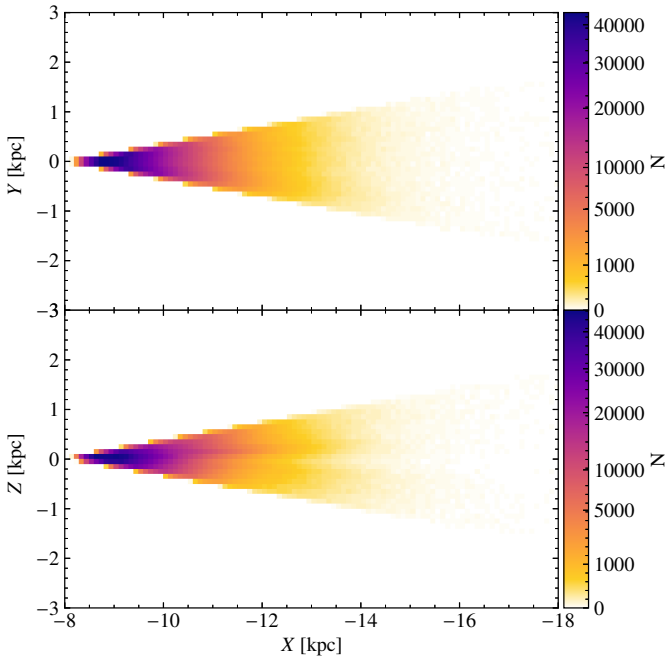

Fig. E.2. Spatial distribution of the AC20-$\varpi/\sigma_\varpi > 3$. a) Counts in bins of 0.1 kpc in the X-Y projection. b) Same but for the X-Z projection.

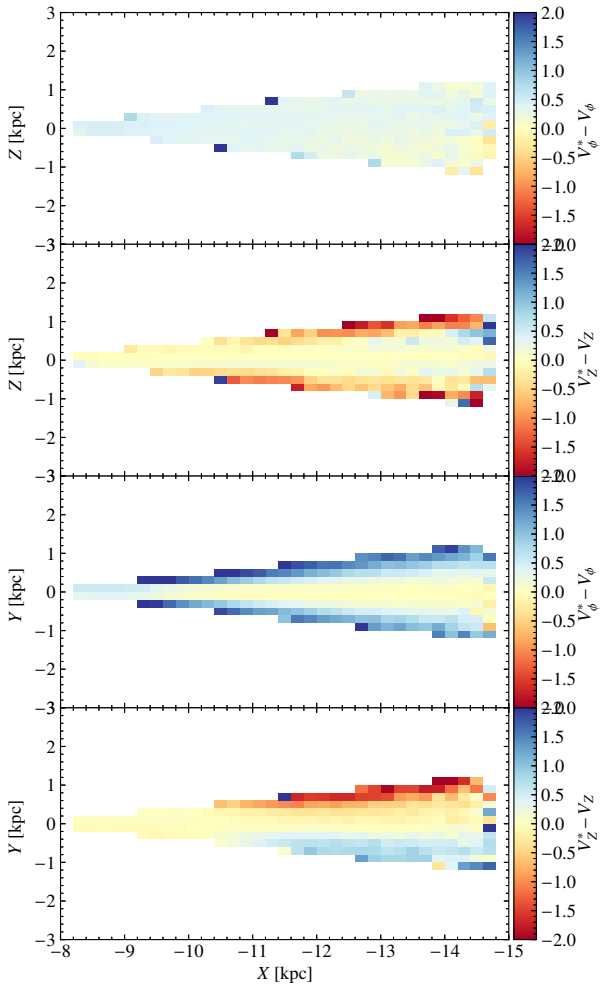

Fig. E.3. Error in the velocities for GOG when using our approximations. Median differences between V_ϕ^* and V_ϕ, and between V_Z^* and V_Z (Eq. 4 and 5) in bins in the X-Y and X-Z projections.

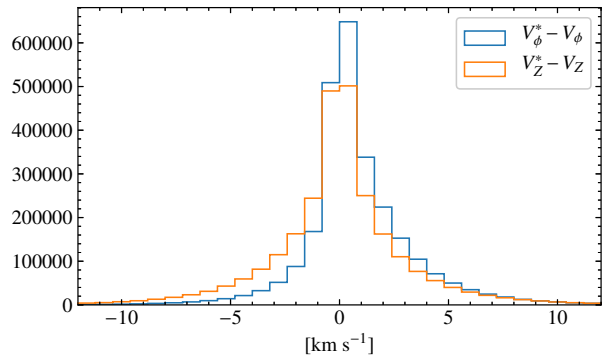

Fig. E.4. Error in the velocities for GOG when using our approximations (part 2). The histogram of the differences between V_ϕ^* and V_ϕ, and between V_Z^* and V_Z is shown. The 10% and 90% percentiles of the differences are -1.5 and 3.9 km s^{-1} and -3.6 and 3.4 for $V_\phi*$ and for V_Z*, respectively.

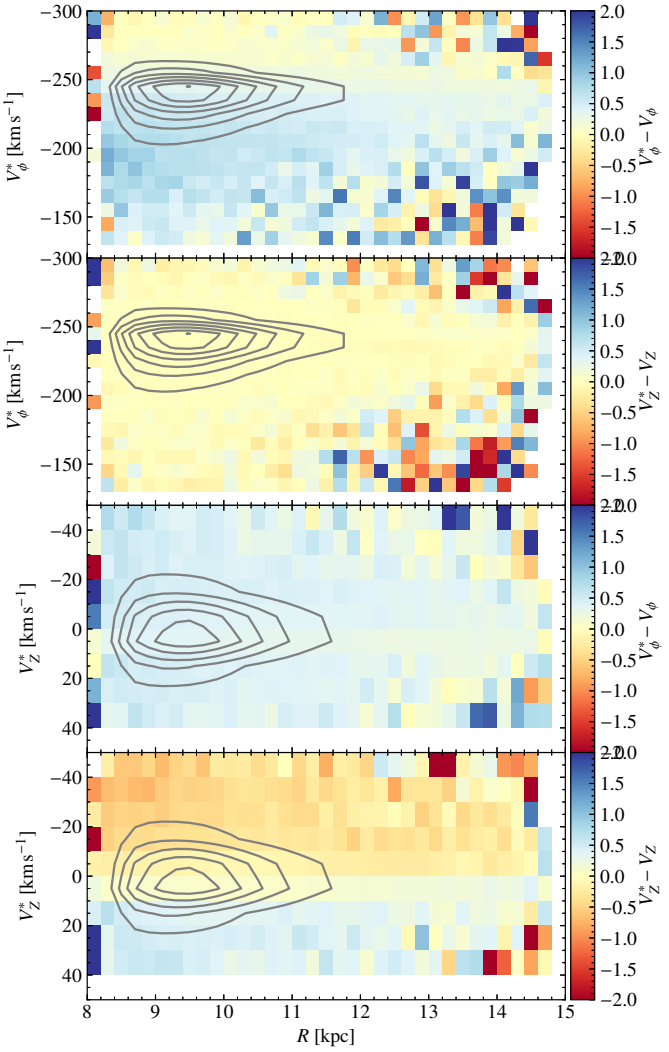

Fig. E.5. Error in the velocities for GOG when using our approximations (part 3). Median differences between V_ϕ^* and V_ϕ, and between V_Z^* and V_Z in bins in the R-V_ϕ^* and R-V_Z^* projections.

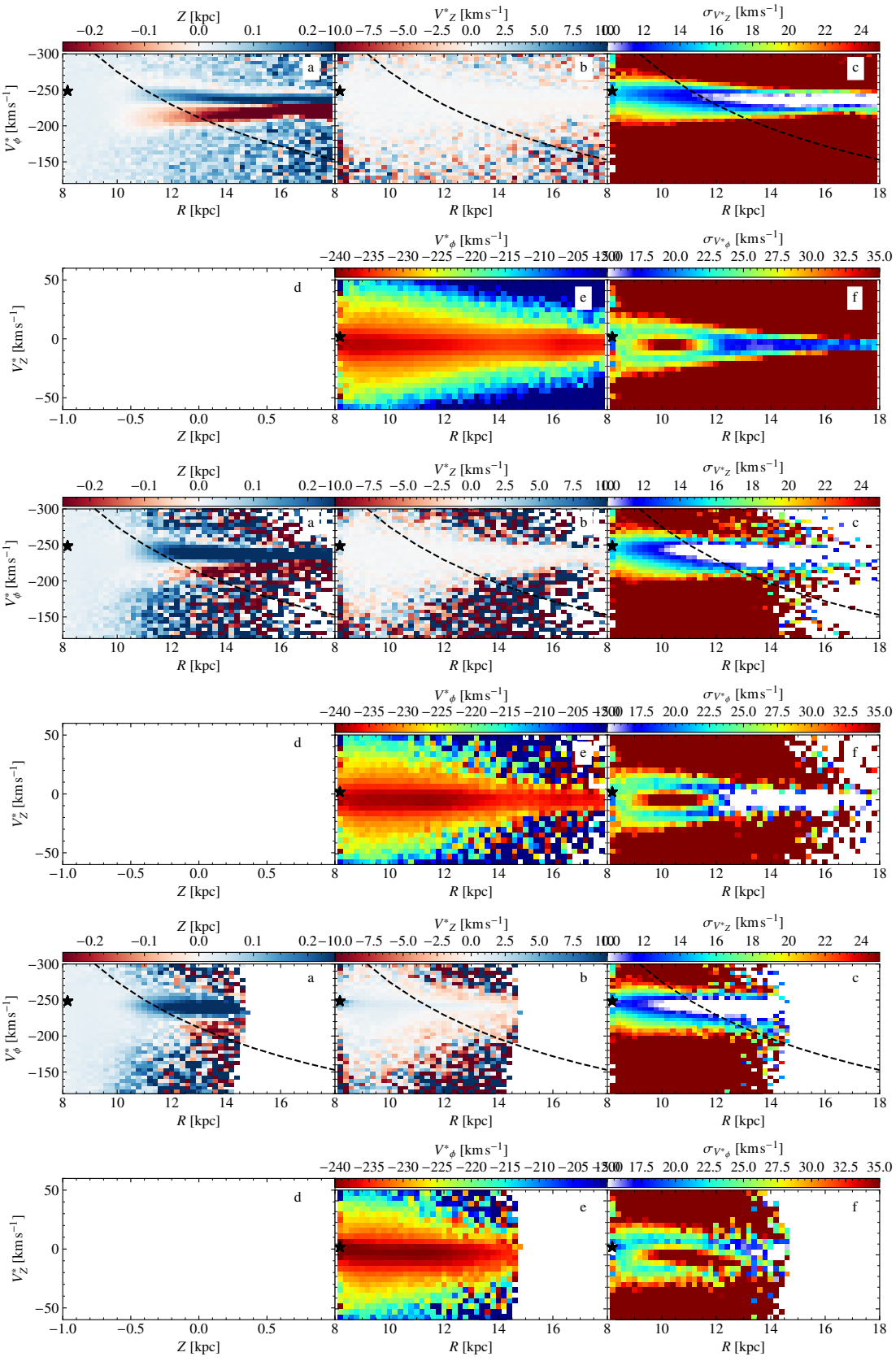

Fig. E.6. Phase space projections for model and mock data. Same as Fig. 13 but for the UM (top), the UM with the sources that in GOG have $\varpi/\sigma_\varpi > 3$ (middle), and for GOG with the selection $\varpi/\sigma_\varpi > 3$ (bottom). The phase space spiral does not exist in GOG and is not shown in panels d.

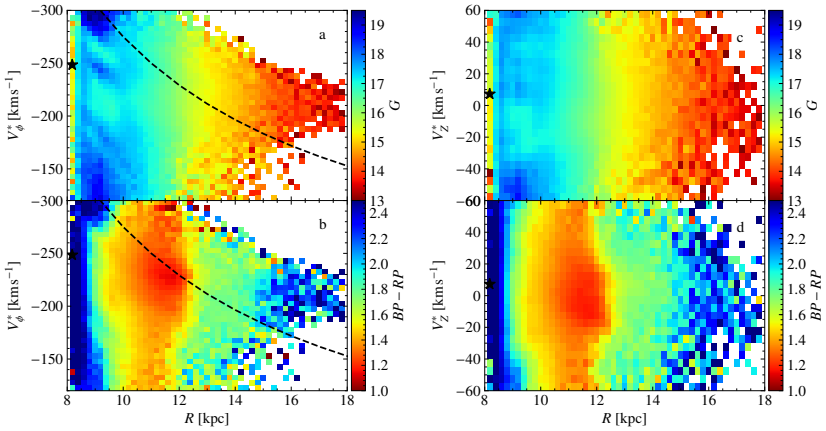

Fig. E.7. Photometry in different phase space projections. Median magnitudes G (top) and colour $BP - RP$ (bottom) in the R-V_ϕ^* plane (left) and R-V_Z^* plane (right) for the AC20-$\varpi/\sigma_\varpi > 3$ sample.

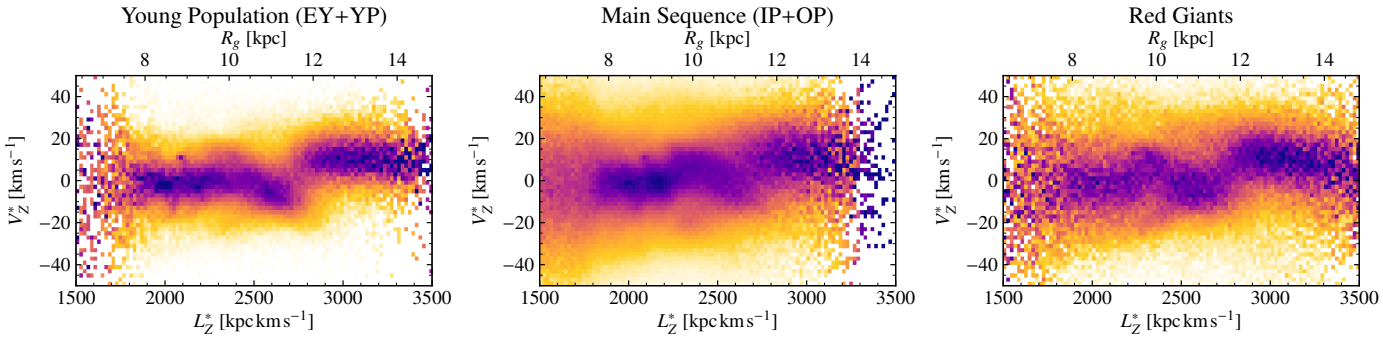

Fig. E.8. Structures in the vertical velocity and angular momentum space for different populations. As in the top panel of Fig. 14, these show a column normalised histogram of star numbers in the L_z, V_Z^* plane but for a given population (as in Sect. 2.2). In all cases the feature at $\sim$ 2750 km s^{-1} kpc is clearly visible. The young population has the lowest velocity dispersion, and therefore shows the feature most cleanly.